University of Alberta

REAL-TIME DIGITAL SIMULATION AND CONTROL OF GRID-CONNECTED WIND ENERGY SYSTEMS

by

Lok Fu Pak

A thesis submitted to the Faculty of Graduate Studies and Research in partial fulfillment of the requirements for the degree of **Master of Science**

Department of Electrical and Computer Engineering

Edmonton, Alberta
Spring 2006

Library and Archives Canada

Published Heritage Branch

395 Wellington Street
Ottawa ON K1A 0N4
Canada

Bibliothèque et Archives Canada

Direction du Patrimoine de l'édition

395, rue Wellington
Ottawa ON K1A 0N4
Canada

Your file Votre référence
ISBN: 0-494-13869-6
Our file Notre référence
ISBN: 0-494-13869-6

NOTICE:
The author has granted a non-exclusive license allowing Library and Archives Canada to reproduce, publish, archive, preserve, conserve, communicate to the public by telecommunication or on the Internet, loan, distribute and sell theses worldwide, for commercial or non-commercial purposes, in microform, paper, electronic and/or any other formats.

The author retains copyright ownership and moral rights in this thesis. Neither the thesis nor substantial extracts from it may be printed or otherwise reproduced without the author's permission.

AVIS:
L'auteur a accordé une licence non exclusive permettant à la Bibliothèque et Archives Canada de reproduire, publier, archiver, sauvegarder, conserver, transmettre au public par télécommunication ou par l'Internet, prêter, distribuer et vendre des thèses partout dans le monde, à des fins commerciales ou autres, sur support microforme, papier, électronique et/ou autres formats.

L'auteur conserve la propriété du droit d'auteur et des droits moraux qui protège cette thèse. Ni la thèse ni des extraits substantiels de celle-ci ne doivent être imprimés ou autrement reproduits sans son autorisation.

In compliance with the Canadian Privacy Act some supporting forms may have been removed from this thesis.

While these forms may be included in the document page count, their removal does not represent any loss of content from the thesis.

Conformément à la loi canadienne sur la protection de la vie privée, quelques formulaires secondaires ont été enlevés de cette thèse.

Bien que ces formulaires aient inclus dans la pagination, il n'y aura aucun contenu manquant.

Canada

Abstract

As more wind energy is integrated to the power network, it becomes critical to study the influence of wind generation on existing power system. Real-time simulation and control of a grid-connected wind farm was investigated using a combination of off-line software and real-time hardware simulators. A reference doubly-fed induction generator (DFIG) based wind turbine generator system (WTGS) was model and validated using several off-line simulation tools. Then, the reference model was utilized for constructing the detailed wind energy systems. By performing various interaction studies using these systems, a set of benchmark results were obtained for the validation of the aggregated models. Finally, three models with different levels of aggregation were developed to improve the efficiency of the real-time electromagnetic transient study of the wind farm, and all of these models were implemented on the Real-Time eXperimental LABoratory (RTX-LAB) digital simulator.

Acknowledgements

First of all, I would like to divulge my gratefulness to Dr. Venkata Dinavahi. You were the one who introduced me to real-time simulation, and gave me the opportunity to put theories into practice. Under your supervision, I learned how to explore knowledge and where to seek answers. Your passion and enthusiasm for your work has motivated me throughout my study. Without your insightful guidance, I might not be able to complete this thesis.

I would also like to praise my colleagues in the Power Lab for their helpful advices and selfless assistances. Special thanks to Omar Faruque, who has always been patient and willing in providing me with the best explanations for many theories, and Xin Nie, who helped me solving many challenging software and technical problems. Your companionship has made the long hours of research study joyful.

Finally, I wish to extend all my gratitude toward my parents for their love, caring, understanding, and inspiration. You have given me everything you had, and asked for nothing in return. The hope and support you gave me through my life made me who I am. I wish that you will smile proudly whenever you are thinking about me.

Contents

1 Introduction 1

1.1 Motivation . . . 1

1.2 Fixed Speed and Variable Speed WTGS . . . 3

1.3 Stand Alone Wind Generator and Wind Farm . . . 5

1.4 Off-Line and Real-Time Digital Simulation . . . 6

1.5 Objectives of Thesis . . . 7

1.6 Scope and Outlines of Thesis . . . 8

2 Modeling of DFIG-based WTGS 10

2.1 Introduction . . . 10

2.2 Background . . . 10

2.3 Aerodynamic Model . . . 11

2.4 Mechanical Model . . . 13

2.5 Electrical Model . . . 17

2.5.1 Wound-Rotor Induction Machine Model . . . 18

2.5.2 Back-to-Back Converter Model . . . 21

2.6 Summary . . . 23

3 DFIG-based WTGS Controller Design 24

3.1 Introduction . . . 24

3.2 Background . . . 25

3.3 Mechanical Control . . . 27

3.4 Electrical Control and Design . . . 28

3.4.1 The WRIM Control Fundamentals 28
3.4.2 Control and Operation of the Back-to-back PWM Converter . 30
3.4.2.1 Vector Control Theory 31
3.4.2.2 PI Controller 33
3.4.2.3 PWM Gating Pulse Generation 34
3.4.3 Electrical Controller Design 35
3.4.3.1 Rotor-Side Converter Control 35
3.4.3.2 Rotor-Side Inverter PI Controller Design 38
3.4.3.3 Grid-Side Converter Control 41
3.4.3.4 Grid-Side Converter PI Controller Design 43
3.5 Summary 46

4 Off-Line and Real-Time DFIG Model Simulation, Comparison, and Validation 47

4.1 Introduction 47
4.2 Background 48
4.2.1 Hardware 49
4.2.2 Software Packages 50
4.3 Off-line DFIG Simulation Result Comparison and Model Validation . 52
4.3.1 Induction Machine Modeling 52
4.3.2 Multi-Mass Model 58
4.3.3 Power Electronics Modeling 59
4.3.4 Complete DFIG Configuration 62
4.4 Real-Time DFIG Model Preparation and Model Validation 66
4.4.1 Off-Line DFIG Model Complexity 67
4.4.2 BBC Optimization 68
4.4.3 WRIM Model Reduction 72
4.4.4 Implementation of the Lumped-Mass Mechanical Model . . . 76
4.4.5 Real-Time Simulation Model Validation 77
4.5 Summary 84

5 Wind Farm Dynamics and Aggregation **85**

5.1 Introduction 85

5.2 Background 86

5.3 Single WTGS Dynamics 86

5.3.1 Interaction of the Stand-Alone WTGS with Variable Wind Speed 87

5.3.2 Interaction of the Stand-Alone WTGS with Grid faults 90

5.3.2.1 Case 1: Single-line-to-ground fault 90

5.3.2.2 Case 2: Three-phase-to-ground fault 94

5.3.2.3 Case 3: Two-phase-to-ground fault 98

5.3.2.4 Summary of Case Studies 102

5.3.3 Real-Time Simulation of the Complete DFIG-based WTGS . . 104

5.4 Wind Farm Structure and Dynamics 110

5.4.1 Structure of the Wind Farm 110

5.4.2 Dynamics of the Wind Farm 112

5.4.3 Real-Time Simulation of the Wind Farm 115

5.5 Wind Farm Aggregation 120

5.5.1 Level One Aggregation 121

5.5.2 Level Two Aggregation 124

5.5.3 Level Three Aggregation 128

5.5.4 Aggregation Summary 130

5.5.5 Real-Time Performance of the Aggregated Models 132

5.6 Summary 135

6 Conclusions and Future Work **136**

6.1 Contributions 136

6.2 Suggestions for Future Research 139

Bibliography **141**

Appendix A Coefficients for $C_p(\theta, \lambda)$ Curve Fitting **151**

Appendix B MATLAB-code for $C_p(\theta, \lambda)$ Curve Fitting 153

B.1 `Cp.m` 154

Appendix C Variables for Mechanical Control 155

Appendix D MATLAB-code for Rotor-side Converter Controller Design 156

D.1 `PI_inner_con1.m` 157

D.2 `PI_outter_con1.m` 157

Appendix E MATLAB-code for Grid-side Converter Controller Design 158

E.1 `PI_inner_con2.m` 159

E.2 `PI_outter_con2.m` 159

Appendix F Induction Machine Starting Schematics 160

Appendix G DC Capacitor Charging Schematics Implementations 162

Appendix H Complete DFIG Implementation 167

Appendix I DFIG Implemented with RT-LAB Modules 174

Appendix J Loop-free Trapezoidal Implementation 176

Appendix K 3rd Order WRIM Implementation 178

List of Tables

2.1 Coefficients for Mechanical Power Computation 12
2.2 Parameters for the GE $1.5MW$ two-masses-spring and lumped-mass model . . . 15
2.3 Hypothetical Nameplate Values and Final WRIM Parameters 20

4.1 Off-line DFIG Model SS Matrix Dimensions 67
4.2 SS Matrix Dimensions of the Optimized DFIG Configuration 70
4.3 Conclusive Overview of the RT and Off-line Simulation Results with Various Optimization Options (FE: Forward Euler; Tra.: Trapezoidal; CTra.: Compensated Trapezoidal) 78
4.4 Execution times for individual tasks within one time-step for various setups 81

5.1 Performance log for the RT virtual HIL simulation 110
5.2 Performance log for the RT simulation of the detail wind farm model 120
5.3 Off-line execution times and errors associated with different levels of aggregation 134
5.4 RT execution times for individual tasks within one time-step 135

A.1 Coefficients for $C_p(\theta, \lambda)$ Curve Fitting 152

C.1 Wind Power Coefficients 155

List of Figures

1.1 Various WTGS configurations: (a) doubly-fed induction generator based variable speed WTGS; (b) direct drive synchronous generator based variable speed WTGS; (c) asynchronous induction generator based fixed speed WTGS 4

2.1 Single WTGS model 11

2.2 $C_p(\lambda, \theta_{pitch})$ curves: (a) specific curves of the GE $1.5MW$ WTGS; (b) reproduction of the GE $1.5MW$ WTGS $C_p(\lambda, \theta_{pitch})$ relation using curve fitting equation (2.3) . . 13

2.3 Complete mechanical model for the DFIG drive-train 14

2.4 Mass spring models for the mechanical drive-train: (a) three-masses-two-spring model; (b) two-masses-spring model; (c) lumped mass model 14

2.5 Two-masses-spring model implementation 16

2.6 Lumped-mass model implementation 17

2.7 Doubly-fed induction generator connected to the grid 17

2.8 Reference frame for WRIM modeling 18

2.9 Induction machine model represented in the qd axis 19

2.10 Switch model: (a) IGBT with anti-parallel diode; (b) custom switch model with ideal switch, diode, and resistors; (c) custom switch model with ideal switch, capacitor, and resistor 21

3.1 Controller model for single WTGS 24

3.2 Power vs. generator rotor rotational speed control curve for GE1.5 26

3.3 Synthesis of the power vs. rotor generator rotational speed control curve for GE1.5 26

3.4 Mechanical control 27
3.5 Induction machine power vs. generator rotor speed characteristic 29
3.6 Effects of the injected voltages: v_{r1}=positve, v_{r2}=zero, and v_{r3}=negative . . 29
3.7 Per-phase v_r injection schematic in steady-state 30
3.8 Electrical signals within the WTGS 30
3.9 Reference frames for vector control: (a) Relationships among different frames; (b) stationary abc frame; (c) stationary $\alpha\beta$ frame; (d) rotating dq frame 31
3.10 PI controller schematics 33
3.11 PWM signal generation: (a) comparison of the carrier and the discretized reference signal; (b) switching pulse stream for individual IGBT switches . 34
3.12 Relationships among the rotor-side converter control frames 36
3.13 Rotor-side converter controller schematic 37
3.14 Block diagrams for PI controller design: (a) inner rotor current current control loop; (b) outer stator active and reactive power control loop 38
3.15 Root-locus for the inner rotor current control loop in z-domain 39
3.16 Designed step responses for the rotor-side converter: (a) inner-loop current response; (b) outer-loop active and reactive power response 40
3.17 Root-locus for the outer active and reactive power control loop in z-domain 40
3.18 Relationships between the grid-side converter control frames 41
3.19 Grid-side converter controller schematic 42
3.20 Block diagrams for PI controller design: (a) inner grid-side current control loop; (b) outer dc voltage control loop 43
3.21 Root-locus for the inner grid-side current control loop in z-domain 44
3.22 Designed step responses for the grid-side converter: (a) inner-loop current response; (b) outer-loop dc voltage response 45
3.23 Root-locus for the outer DC voltage control loop in s-domain 45

4.1 RTX-LAB real-time simulator hardware configuration 49
4.2 Un-controlled WRIM starting with shorted rotor terminals 52

4.3 Simulation results for WRIM modeled in stationary reference frame: (a) stator-side active power; (b) stator-side reactive power 53
4.4 Simulation results for WRIM modeled in rotor reference frame: (a) stator-side active power; (b) stator-side reactive power 54
4.5 Simulation results for WRIM modeled in synchronous reference frame: (a) stator-side active power; (b) stator-side reactive power 54
4.6 Linear electrical system model with nonlinear machine modeled as current feedback 55
4.7 Elementary integration methods: (a) Forward Euler; (b) Trapezoidal 56
4.8 Observations of quadrature rotor flux integration using forward euler method: (a) in stationary reference frame; (b) in rotor reference frame; (c) in synchronous reference frame, where the black and grey lines indicate the results obtained with $5\mu s$ and $50\mu s$, respectively 57
4.9 Electrical torque and rotor speed of the multi-mass system simulated in: (a) MATLAB®/SIMULINK®; (b) PSCAD™/EMTDC™; (c) EMTP-RV . . 59
4.10 Control of grid-side converter voltage and current simulated in: (a) PSCAD™/EMTDC™; (b) MATLAB®/SIMULINK®; (c) EMTP-RV 61
4.11 DFIG stator-side active and reactive power, and DC-link voltage simulated in: (a) MATLAB®/SIMULINK®; (b) PSCAD™/EMTDC™; (c) EMTP-RV . 63
4.12 Control of grid-side converter voltage and current simulated using; (a) the ideal switch, diode and resistor model; (b) the ideal switch, capacitor and resistor model 65
4.13 Switching function based converter model 70
4.14 Stator-side active and reactive power, and DC-link voltage simulated with: (a) the validated detailed off-line DFIG model in SIMULINK®; (b) the DFIG model implemented with 5^{th} order IM model integrated with Trapezoidal method and TSB model 71
4.15 Interactions of the DFIG electrical model in SIMULINK® 72

4.16 Stator-side active and reactive power, and DC-link voltage simulated with: (a) the validated detailed off-line DFIG model in SIMULINK®; (b) the DFIG model implemented with 5^{th} order IM model integrated with loop-free Trapezoidal method and TSB model 74
4.17 Stator-side active and reactive power, and DC-link voltage simulated with: (a) the validated detailed off-line DFIG model in SIMULINK®; (b) 3^{rd} order IM model integrated with loop-free Trapezoidal method and TSB . . 75
4.18 : Comparing the difference between two-masses-spring and lump-mass model with the simulation results of: (a) stator-side active power in SIMULINK®; (b) stator-side reactive power; (c) rotor speed 76
4.19 : Including the OpComm block to activate the XHP mode for real-time simulation 77
4.20 : Real-time and off-line simulation results for Setup 21: (a) stator-side active power; (b) stator-side reactive power; (c) DC-line voltage 82
4.21 : Real-time and off-line simulation results for Setup 22: (a) stator-side active power; (b) stator-side reactive power; (c) DC-line voltage 83

5.1 Single grid-connected DFIG-based WTGS 87
5.2 Synthesis of the variable wind speed 88
5.3 Response of the single DFIG-based WTGS to variable wind speed: (a) variable wind signal; (b) turbine rotational speed; (c) generated active power; (d) generated reactive power; (e) turbine blade pitch angle 89
5.4 Three-phase voltage and current waveforms at bus B2 and B3 during the single-phase-to-ground fault 91
5.5 Impacts of the single-line-to-ground fault on the WTGS internal parameters: (a) magnitude of the supporting voltage; (b) turbine rotational speed; (c) generated active power; (d) generated reactive power; (e) DC-link voltage 92
5.6 Zoom-in view of Fig. 5.5: (a) magnitude of the supporting voltage; (b) generated active power; (c) generated reactive power; (d) DC-link voltage . 93

5.7 Three-phase voltage and current waveforms at bus B2 and B3 during the three-phase-to-ground fault 95
5.8 Impacts of the three-phase-to-ground fault on the WTGS internal parameters: (a) magnitude of the supporting voltage; (b) turbine rotational speed; (c) generated active power; (d) generated reactive power; (e) DC-link voltage 96
5.9 Zoom-in view of Fig. 5.8: (a) magnitude of the supporting voltage; (b) generated active power; (c) generated reactive power; (d) DC-link voltage . 97
5.10 Three-phase voltage and current waveforms at bus B2 and B3 during the two-phase-to-ground fault 99
5.11 Impacts of the two-phase-to-ground fault on the WTGS internal parameters: (a) magnitude of the supporting voltage; (b) turbine rotational speed; (c) generated active power; (d) generated reactive power; (e) DC-link voltage 100
5.12 Zoom-in view of Fig. 5.11: (a) magnitude of the supporting voltage; (b) generated active power; (c) generated reactive power; (d) DC-link voltage . 101
5.13 Overviews of the impacts from the various line faults 103
5.14 Voltage and current waveforms at bus B2 and B3 : (a) at the beginning; and (b) at the end of the supply voltage sag 105
5.15 Comparisons of the oscilloscope traced RT simulation results (left) with the corresponding off-line results generated using SIMULINK® (right): (a) turbine rotational speed; (b) generated active power; (c) generated reactive power 107
5.16 Comparisons of the oscilloscope traced RT simulation results (left) with the corresponding off-line results generated using SIMULINK® (right): phase-*a* voltage at bus B3 during (a) single-phase-to-ground fault; (b) three-phase-to-ground fault; (c) two-phase-to-ground fault 108

5.17 Comparisons of the oscilloscope traced RT simulation results (left) with the corresponding off-line results generated using SIMULINK® (right): phase-*a* current at bus B3 during (a) single-phase-to-ground fault; (b) three-phase-to-ground fault; (c) two-phase-to-ground fault 109
5.18 Wind farm schematic 111
5.19 Physical attributes of the wind farm and the hypothetical wind direction . . 112
5.20 Synthesis of the variable wind speed signals for (a) WTGSs 1, 2, and 3; (b) WTGSs 4 and 5; (c) WTGSs 6, 7, and 8; (d) WTGSs 9 and 10 113
5.21 Wind farm response to variable wind speed measured at the collector bus: (a) generated active power; and (b) generated reactive power from the wind farm 114
5.22 Wind farm responses to various grid faults measured at the collector bus: (a) single-line-to-ground fault; (b) three-phase-to-ground fault; (c) two-phase-to-ground fault 115
5.23 Division of the detailed wind farm model for RT simulation 116
5.24 Distribution of the subsystems across the *target cluster* 117
5.25 Comparisons of the oscilloscope traced RT simulation results (left) with the corresponding off-line results generated using SIMULINK® (right): phase-*a* voltage at the collector bus during (a) single-phase-to-ground fault; (b)three-phase-to-ground fault; (c) two-phase-to-ground fault 118
5.26 Comparisons of the oscilloscope traced RT simulation results (left) with the corresponding off-line results generated using SIMULINK® (right): phase-*a* current at the collector bus during (a) single-phase-to-ground fault; (b)three-phase-to-ground fault; (c) two-phase-to-ground fault 119
5.27 Division of the wind farm for Level One aggregation 121
5.28 Comparisons of the variable wind speed responses generated by the detailed and Level One Aggregation model: (a) generated active power measured at collector bus; (b) generated reactive power measured at collector bus 122

5.29 Comparisons of the fault responses generated by the detailed and Level One Aggregation model: (a) response to single-line-to-ground fault; (b) response to three-phase fault; (c) response to two-line-to-ground fault . . . 124
5.30 Comparisons of the collector bus: phase-*a* (a) voltage; and (b) current, during single-line-to-ground fault generated by the detailed and Level One Aggregation model . . . 125
5.31 Comparisons of the collector bus: phase-*a* (a) voltage; and (b) current, during three-phase fault generated by the detailed and Level One Aggregation model . . . 125
5.32 Comparisons of the collector bus: (a) phase-*a* voltage; and (b) current, during two-line-to-ground fault generated by the detailed and Level One Aggregation model . . . 126
5.33 Variable wind speed signals for the Level Two aggregation model . . . 126
5.34 Comparisons of the variable wind speed responses generated by the detailed and Level Two Aggregation model: (a) generated active power measured at collector bus; (b) generated reactive power measured at collector bus . . . 127
5.35 Comparisons of the fault responses generated by the detailed and Level Two Aggregation model: (a) response to single-line-to-ground fault; (b) response to three-phase fault; (c) response to two-line-to-ground fault . . . 128
5.36 Comparisons of the collector bus: phase-*a* (a) voltage; and (b) current, during single-line-to-ground fault generated by the detailed and Level Two Aggregation model . . . 129
5.37 Comparisons of the collector bus: phase-*a* (a) voltage; and (b) current, during three-phase fault generated by the detailed and Level Two Aggregation model . . . 129
5.38 Comparisons of the collector bus: phase-*a* (a) voltage; and (b) current, during two-line-to-ground fault generated by the detailed and Level Two Aggregation model . . . 130
5.39 Variable wind speed signal for the Level Three aggregation model . . . 130

5.40 Comparisons of the variable wind speed responses generated by the detailed and Level Three Aggregation model: (a) generated active power measured at collector bus; (b) generated reactive power measured at collector bus 131
5.41 Comparisons of the fault responses generated by the detailed and Level Three Aggregation model: (a) response to single-line-to-ground fault; (b) response to three-phase fault; (c) response to two-line-to-ground fault . . . 132
5.42 Comparisons of the collector bus: phase-*a* (a) voltage; and (b) current, during single-line-to-ground fault generated by the detailed and Level Three Aggregation model 133
5.43 Comparisons of the collector bus: phase-*a* (a) voltage; and (b) current, during three-phase fault generated by the detailed and Level Three Aggregation model 133
5.44 Comparisons of the collector bus: phase-*a* (a) voltage; and (b) current, during two-line-to-ground fault generated by the detailed and Level Three Aggregation model 134

F.1 Induction Machine Starting Schematics Implemented in: (a) PSCAD/EMTDC V.4.0; (b) MATLAB/SIMULINK V.7.0.1; (c) EMTP-RV V1.1 161

G.1 DC Capacitor Charging Electrical Schematics Implemented in PSCAD/EMTDC V.4.0 162
G.2 DC Capacitor Charging Electrical Schematics Implemented in MATLAB/SIMULINK V.7.0.1 163
G.3 DC Capacitor Charging Electrical Schematics Implemented in EMTP-RV V1.1 . . 163
G.4 DC Capacitor Charging Control Schematics Implemented in PSCAD/EMTDC V.4.0 164
G.5 DC Capacitor Charging Control Schematics Implemented in MATLAB/SIMULINK V.7.0.1 165
G.6 DC Capacitor Charging Control Schematics Implemented in EMTP-RV V1.1 . . . 166

H.1 DFIG Schematics Implemented in PSCAD/EMTDC V.4.0 168
H.2 Rotor-side Converter Controller Schematics Implemented in PSCAD/EMTDC V.4.0 169
H.3 DFIG Schematics Implemented in MATLAB/SIMULINK V.7.0.1 170
H.4 Rotor-side Converter Controller Schematics Implemented in MATLAB/SIMULINK V.7.0.1 171
H.5 DFIG Schematics Implemented in EMTP-RV V1.1 172
H.6 Rotor-side Converter Controller Schematics Implemented in EMTP-RV V1.1 . . . 173

I.1 PWM Pulse Generation with RT-EVENTS V.2.4 Comparison Block 174
I.2 DFIG Schematics Implemented with RT-EVENTS V.2.4 Time-Stamped Bridge . . 175

J.1 Loop-free Trapezoidal Implementation for WRIM in MATLAB/SIMULINK V.7.0.1: (a) stator-side algebraic-loop compensated with memory buffer and prediction mechanism; (b) original stator winding model 177

K.1 3^{rd} Order WRIM Implementation in MATLAB/SIMULINK V.7.0.1: (a) modified stator winding model; (b) original stator winding model 178

List of Acronyms

A/D	Analog-to-Digital
AWEA	American Wind Energy Association
BBC	Back-to-Back Converter
COTS	Commercial-Off-The-Shelf
CPU	Central Processing Unit
CTra.	Compensated Trapezoidal integration method
D/A	Digital-to-Analog
DFIG	Doubly-Fed Induction Generator
EMTP	Electro-Magnetic Transient Program
FE	Forward Euler integration method
FPGA	Field Programmable Gate Array
GUI	Graphical User Interface
HIL	Hardware-In-the-Loop
HT	Hyper-Threading
IGBT	Insulated Gate Bipolar Transistor
IM	Induction Machine
LVRT	Low Voltage Ride-Through

MMs	Multi-mass
OS	Operating System
PC	Personal Computer
PCC	Point of Common Coupling
PWM	Pulse Width Modulation
RT	Real-Time
RTX-LAB	Real-Time eXperimental LABoratory
Tra.	Trapezoidal integration method
TS	Time-Stamped
TSB	Time-Stamped Bridge
SS	State-Space
SPS	SimPowerSystem
WECC	Western Electricity Coordinating Council
WRIM	Wound Rotor Induction Machine
WTGS	Wind Turbine Generation System
XHP	eXtremely High Performance

List of Symbols

$'$	rotor-side parameter referenced to the stator-side
dr	Rotor-side parameter referred to the direct axes
ds	Stator-side parameter referred to the direct axes
qr	Rotor-side parameter referred to the quadrature axes
qs	Stator-side parameter referred to the quadrature axes
$l-l$	Line-to-line
r	WRIM rotor-side parameter
s	WRIM stator-side parameter
$\alpha_{i,j}$	Coefficient for characterizing $C_p(\lambda, \vartheta_{pitch})$
$\alpha\beta$	Stationary orthogonal reference frame with α laying at 0° and β leading by 90°
abc	Stationary three-phase reference frame
A, B, C, D	SIMULINK® state-space matrices
C_p	Power coefficient indicating percentage of wind power extracted from the wind
dq	Rotating orthogonal reference frame with d as the reference and q leading by 90°
D	Damping ratio

D_{bg}	Damping ratio of the high-speed generator shaft
D_{tb}	Damping ratio of the low-speed turbine shaft
D_{tg}	Damping ratio of the combinational shaft between the turbine and generator rotor
ϵ_P	Maximum error between the collector bus active power generated by the detailed wind farm and aggregation models
ϵ_Q	Maximum error between the collector bus reactive power generated by the detailed wind farm and aggregation models
E	Machine internal voltage
f	Gearbox ratio
f_e	Electrical frequency
f_s	Grid electrical frequency
H	Turbine inertia at the low-speed side
H_g	Generator rotor inertia
H_T	Turbine inertia at the high speed side
H_{lump}	Lumped-mass inertia
i	Phase current / current referred to a specific axes
I_{ms}	Stator-flux current
I_{coll}	Collector bus current
$\lvert\overrightarrow{I_{ms}}\rvert$	Magnitude stator-flux current
K	Spring constant
K_{bg}	Spring constant of the high-speed generator shaft
K_i	Integral gain
K_{ic}	Pitch compensating PI controller integral gain

K_{ip}	Pitch controlling PI controller integral gain
K_{itrq}	Torque controlling PI controller integral gain
K_p	Proportional gain
K_{pc}	Pitch compensating PI controller proportional gain
K_{pp}	Pitch controlling PI controller proportional gain
K_{ptrq}	Torque controlling PI controller proportional gain
K_{tb}	Spring constant of the low-speed turbine shaft
K_{tg}	Spring constant of the combinational shaft between the turbine and generator rotor
λ	Tip-speed ratio
L_{fg}	BBC grid-side filter inductance
L_{fr}	BBC rotor-side filter inductance
L_m	Magnetizing inductance
L_{lr}	Rotor leakage inductance
L_{ls}	Stator leakage inductance
L_r	Rotor inductance
L_s	Stator inductance
ρ	Air density
rms	Root mean square
R_{fg}	BBC grid-side filter resistance
R_r	Rotor winding resistance
R_s	Stator winding resistance

ψ_{dr}	Rotor magnetic flux on the direct axes
ψ_{ds}	Stator magnetic flux on the direct axes
ψ_{qr}	Rotor magnetic flux on the quadrature axes
ψ_{qs}	Stator magnetic flux on the quadrature axes
p	Number of pole pairs
P_{elec}	Total generated active electrical power
P_{max}	Maximum active power generation
P_{min}	Minimum active power generation
P_{mech}	Mechanical power captured by the wind turbine
P_{ord}	Active power generation command
P_r	Rotor-side active power
P_s	Stator-side active power
P_{coll}	Collector bus active power
qd	Rotating orthogonal reference frame with q as the reference and d lagging by 90°
Q_{elec}	Total generated reactive electrical power
Q_r	Rotor-side reactive power
Q_s	Stator-side reactive power
Q_{coll}	Collector bus reactive power
R_{off}	IGBT switch-off resistance
R_{on}	IGBT switch-on resistance
R_T	Turbine radius
S_C	High frequency triangular carrier signal

Sig_{PWM}	Electrical control signal
Sig_{trip}	Electrical protection signal
θ	Angular position of an arbitrary qd frame
θ_{min}	Maximum pitch angle
θ_{max}	Minimum pitch angle
θ_{pitch}	Pitch angle of turbine blades
θ_r	Angular position of the WRIM rotor
t	time
t_F	IGBT switch off extinction time
T_{avg}	Average off-line simulation time
T_{elec}	Electrical torque
T_{mech}	Mechanical torque
T_{pc}	Time delay for active power command execution
T_P	Time delay for pitch angle command execution
T_{rs}	Generator shaft torque
T_{RT}	Maximum real-time execution time
T_S	Simulation Step-size
ν_w	Wind speed
uv	Rotating orthogonal rotor reference frame
v	Phase voltage / voltage referred to a specific axes
v_r	Injected rotor voltage

V_{dc}	DC-link voltage
V_{on}	IGBT switch-on forward voltage
V_s	Stator terminal voltage
$\lvert\vec{V_s}\rvert$	Magnitude of stator terminal voltage
V_S	Transmission line voltage / Supply voltage
V_r	WRIM rotor terminal voltage
I_{coll}	Collector bus voltage
ω	Rotational speed of an arbitrary qd frame
ω_b	Base rotational speed
ω_e	Electrical speed
ω_{err}	Speed error
ω_{ms}	Rotational speed of the stator-flux frame
ω_r	Generator rotor speed
ω_{ref}	Reference speed
ω_T	Turbine rotating speed
ω_{sync}	Synchronous speed
xy	Rotating orthogonal stator-flux reference frame

1 Introduction

1.1 Motivation

Research and development of renewable energy has gained tremendous momentum in the past decade as the cost of conventional electrical power generation continuously escalate due to the limited fuel resources, and the general public becomes increasingly concerned of the environmental impacts caused by the thermal and nuclear generation. Among many technologies promising green power, the utilization of wind energy via wind turbine generation system (WTGS) is one of the most mature and well developed. Across the world, the total capacity of wind generation has already exceeded giga-watt (GW) rating and larger wind farms are constantly being planned and commissioned [1–6].

Referring to the report in [4], potentially available wind power is being under utilized. Common explanations for the conservative exploration is associated with the intermittent nature of the wind. Because of the stochastic behavior, bringing wind energy to the market becomes a difficult task. To justify the investment in wind generation, the captured energy need to be effectively distributed under the current market structure involving day-ahead forecasting, day-ahead market,

unit commitment, real-time operation, and market settlement [4]. There are research studies [1, 7] targeting the development of correlation model that will allow estimating the wind power of an area from the measurements taken from a distant site. Once the model is completed, wind farm operator may be able to more accurately predict the available wind power and its pattern ahead of time. However, to understand the impact of captured wind energy on the network and be able to make spontaneous decisions an authentic wind facility model is needed.

To deliver the wind power safely is another challenge faced by the facility owner and operator alike. Since many of the best wind resources are remotely located from the main grid, the reliability issues associated with the relatively weak transmission system often have a negative effect on the wind energy integration. In order to sustain system stability and power quality, sophisticated controller and protective devices must be installed to direct the wind facilities through the hazardous fault conditions. For the development and testing of these high-speed equipment, modern simulation technology provides an accurate, timely, and cost efficient platform [1,2].

As wind generation achieves commercial viability in North America, many organizations, such as American Wind Energy Association (AWEA) and Western Electricity Coordinating Council (WECC), are pushing for codifying requirements and performance standards for large wind generation facilities. Although the technical details of the wind facility operation recommendations are yet to be finalized, the major areas of concern, such as low voltage ride-through (LVRT) and reactive power capability, are generally accepted. Formal development, update, and improvement of the engineering models and turbine specifications used for studying the wind plant interconnections are also listed in the advisory requirements.

Fully digital electromagnetic transients program (EMTP) has greatly simplified the study of power system and its interactions with various equipments. Using modern graphical interfacing EMTP-type software simulators, such as PSCAD™/EMTDC™, SPS/SIMULINK®, and EMTP-RV, the wind facility and

the power system it is connected to can be efficiently represented with the built-in mathematical models. Accuracy of the models are ensured by following the standard EMTP modeling practice that has been refined and confirmed by previous researchers with many years of experience in experimental comparison studies.

Aided by the advancements in computing technology and the development of EMTP-type software packages, researchers can now conduct massive power system study and equipment testings on the powerful real-time simulators. These simulators geared with latest innovations can handle the computation of complex mathematical models with microsecond resolution, and allow high frequency interaction with real equipments. These features not only open up a whole new gateway for research study, but also tie the research results closer to real-world demand.

1.2 Fixed Speed and Variable Speed WTGS

In general, there are two types of WTGSs: fixed-speed and variable-speed. With relatively simple design, Fig. 1.1 (c), the fixed-speed WTGS provided a cost efficient opportunity for entrepreneurs to explore the viability of pollution-free generation in the early days. However, the poor mechanical isolation and narrow operating speed range inherited from the direct connection of a turbine driven squirrel-cage induction machine has limited the generation yield [8–10]. Another problem impairing the fixed-speed WTGS was the frequent shut-off caused by high wind speed, disturbance in the grid, or excess reactive power consumption [3]. Although many remedies, such as stall/pitch control and supporting capacitor bank, were proposed, the fixed-speed design is being phased out of the market particularly in the area requiring high capacity WTGSs [3].

Introduction of the variable-speed WTGS has bred new life into the wind generation sector. Addition of the power electronic driven variable-speed drive have drastically improved the performance of a WTGS in virtually every aspect [3, 11–14]. Between the two major variants, Fig. 1.1 (a) and (b), the doubly-

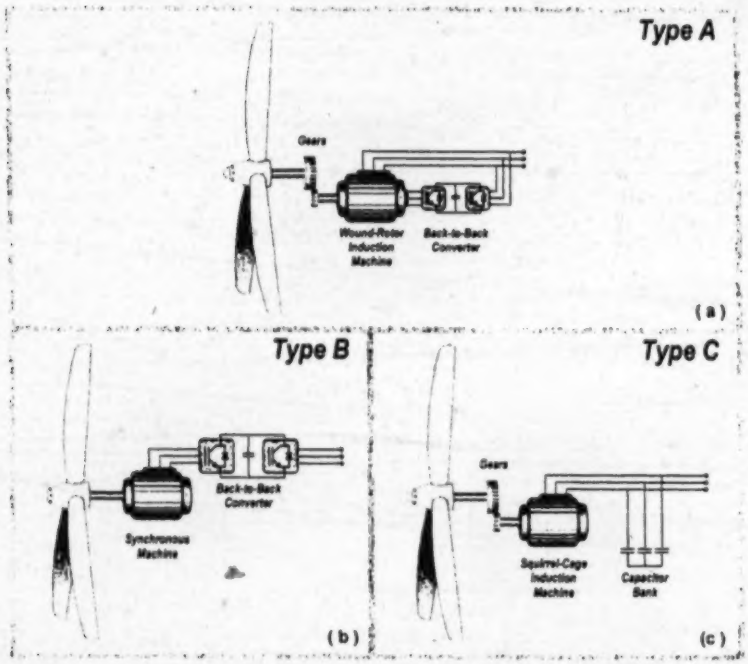

Figure 1.1: Various WTGS configurations: (a) doubly-fed induction generator based variable speed WTGS; (b) direct drive synchronous generator based variable speed WTGS; (c) asynchronous induction generator based fixed speed WTGS

fed configuration (Type A) has gained the most popularity owing mainly to its economical design. Instead of having high-cost full scale converter at the mains, the power electronic drive connected between the stator and rotor of the wound rotor induction machine (WRIM) is required to handle only fraction of the total generation capacity. In spite of the more expensive WRIM, savings from the lower rating power electronics has placed the doubly-fed induction generator (DFIG) based WTGS in a very competitive position [15]. In the current market, generation capacity of the Type A WTGSs has already reached MW range.

When the capacity and number of the DFIG-based WTGS continuously increase in the network, it is no longer appropriate to model them as simple negative loads [6]. To help reflect their actual impact on the existing system under various operating conditions, the WTGSs need to be modeled with sufficient details.

1.3 Stand Alone Wind Generator and Wind Farm

Researchers have been focusing their studies on the stand alone WTGS. Few WTGSs were erected in an autonomous grid for 'fuel displacement' purposes as well as for earning some 'capacity credit' [16]. Since the WTGSs were usually coupled with a diesel generator or other means of backup systems [10, 16], the control system was designed to mainly allow maximum extraction of wind energy. When irregularities were encountered, the controller would simply trip the WTGS from the line.

In contrast, modern WTGSs with much higher generation capacity are collectively connected to the power network in the form of wind farms. As wind is moving into the main steam of generation sources, a deeper understanding of its potential impacts on the interactions with the bulk electric power system is needed, and this need has shaped the trend of modeling and simulation of grid-connected wind farms [2, 17–25].

A large wind farm under contain tens or even hundreds of WTGSs. Since the aggregated performance is more important [1, 26], modeling each WTGS in detail will not only form a huge computational burden for simulation studies, but also create redundant information hampering the overall productivity of the research study. In order to produce an aggregated wind farm model, a general two-step approach has been proposed [24, 26, 27]. First, the model representing each WTGSs shall be simplified to retain only the characterizing details. Then based on the response to the wind speed and interaction to the grid, a group of WTGSs can be collectively represented with a model having equivalent capacity. However, substantial amount of study is required to realize these generalized guidelines. Developing a wind farm consisted of detailed WTGSs is the preliminary requirement. When it comes to determining the coherence among the individual WTGSs, the stochastic behavior of the wind source, geographical properties, and electrical connections shall be carefully accounted for.

1.4 Off-Line and Real-Time Digital Simulation

Most digital simulations running on personal computers (PCs) are off-line in nature. Using the latest simulation software packages, these simulations are easy to setup. Because there are no specific requirements on the amount of time used to perform the off-line arithmetic computations, efficiency of the software model and hardware components are usually not strictly optimized during the research study. Nevertheless, to keep up with the pace of current technology developments related to wind energy, conducting only off-line simulation studies becomes insufficient.

To overcome the limitations in off-line simulation studies, adoption of real-time simulation is a necessity. There are many commercially available real-time simulators basing on various technologies: HYPERSIM from Hydro-Québec, Real-Time Digital Simulator (RTDS™) from Manitoba Hydro, RT-Lab™ from Opal-RT, etc. Besides simulating a complex model at blazing speed, these simulators are capable of instantaneous communication with external hardware through their high resolution analog-to-digital (A/D) and digital-to-analog (D/A) interfacing devices. This is one of the most important features accrediting the real-time simulators for developing, prototyping, testing and troubleshooting the ever speedier digitized controllers and power electronics.

For time critical studies, such as generation forecasting, real-time simulation is indispensable. When the window for decision making is limited to less than a day, no time can be wasted in waiting for the simulation results. As the forecasted wind pattern is continuously feeding in, an off-line simulation study might not be able to keep up with the computation demand and result in the waste of valuable data leading to misjudgement.

Real-time electromagnetic simulation of a wind farm is important for the design and coordination of the protection system within as well as outside the wind farm. Through the high resolution I/O ports, relay, circuit breakers, and their controllers can be connected to a real-time simulator for hardware-in-the-loop (HIL) testings. Executing in the simulator, the detailed wind facility and transmission system

model would interact with the externally connected protective devices in real-time. Developer can impose any kind of fault conditions onto the real-time model for equipment performance evaluations. This HIL configuration not only provide enough resolution to satisfy the electromagnetic studies, but also avoid the hazardous field testing and time consuming site trial data recording [28].

Many operators are not familiar with the procedures when it comes to managing a wind farm. Thus, realistic training is required for building up the expertise. By interfacing the real-time simulator with the control panel and monitoring devices, a virtual control room can be setup. With the computation capacity of the modern processors, the real-time simulator can simultaneously handle the user responses and simulation of the wind facility under various operating conditions.

Many researchers have even developed their own hybrid simulator [29–32] or emulator [33] specifically for real-time wind energy research. However, most of these studies were performed using either non-scalable components requiring constant maintenance [32] or based on customized platform. Verification of the reported simulation results can be difficult and costly. Although the hybrid configuration can provide accurate results for the analysis of a single WTGS, the detailed modeling and real-time simulation of a wind farm can only be conducted through the fully digital setup. For the given reasons, this research is dedicated for developing an aggregated wind farm model suitable for real-time study under a widely utilized platform and affordable commercial hardware components.

1.5 Objectives of Thesis

The main focus of this research study is to develop and verify the aggregation techniques that are suitable for real-time wind farm electromagnetic simulation studies. By following the step-by-step approach, a detailed single DFIG-based WTGS model will first be created using EMTP-type software. Once the detailed model is verified through comparison studies, it will undergo a series of optimizations, and the end result should be a simple yet representative model suitable for real-time electromagnetic transient studies.

With the stand-alone WTGS model as the fundamental building block, focus will be extended to the modeling and simulation of a wind farm. Then the systematic aggregation techniques will be applied and accredited through in-depth analysis. To enable result reproduction and further research studies on the related subject, detailed recording of the development theories, problems encountered and their solutions, and verification procedures will be clearly presented.

1.6 Scope and Outlines of Thesis

The presentation of analysis and results obtained for this research study is divided into four chapters. In Chapter 2, detailed mechanical and electrical model were developed for the DFIG-based WTGS. The development of these models are in large guided by the specifications for GE $1.5MW$ WTGS, which is the most popular design in North America [2, 15]. When modeling details are missing from the manufacture's document [34], widely accepted conventional practices are applied in order to complete the model.

Modeling and design of the WTGS mechanical and electrical controller are given in Chapter 3. To clarify the complex control concept, pitch control, variable speed control fundamental, PI controller application, and pulse-width-modulation (PWM) principles are discussed along with the root-locus design procedure.

Chapter 4 concentrates on the validation and real-time simulation of the DFIG configuration. Since this configuration comprised of the most complicated electrical components and control logics, it was validated by comparing the off-line simulation results from PSCAD™/EMTDC™, MATLAB®/SIMULINK®, and EMTP-RV. This validated model was then simplified and optimized for real-time simulations using the Real-Time eXperimental LABoratory (RTX-LAB) simulator.

In Chapter 5, the dynamics of the complete WTGS were examined. From studying the interactions of a single WTGS with variable wind speed and grid faults, insights for the dynamic wind farm responses were provided. Then, a detailed wind farm model was constructed for real-time simulation and aggregation technique developments.

A summary of the contributions of this research study is given in Chapter 6. Lastly, recommendations and future perspectives in the field of wind energy are given.

2

Modeling of DFIG-based WTGS

2.1 Introduction

A detailed DFIG-based WTGS is developed for the forthcoming studies of model simplification and wind farm aggregation. The amount of detail contained in this model will be sufficient for characterizing the critical dynamics of a WTGS. In order to obtain the most feasible detailed model, many publications [12, 13, 16, 32, 35–47] were consulted along with the manufacturer's documentation [34]. By following common practice and the collected data, the detailed model based on the popular GE $1.5MW$ WTGS was chosen as the basis for present studies and it was divided into three sub-models: Aerodynamic, Mechanical, and Electrical. Even with a specific manufacturing system as its underlining design, the developed WTGS model does not lose its generality. It can be employed for modeling the DFIG-based WTGSs from other manufacturers as well.

2.2 Background

The WTGS model is a collective representation of the sub-models. Various electrical (i.e. currents and voltages) and mechanical (i.e. torque and speed) signals

are processed and exchanged among the aerodynamic, mechanical, and electrical models, shown in Fig. 2.1.

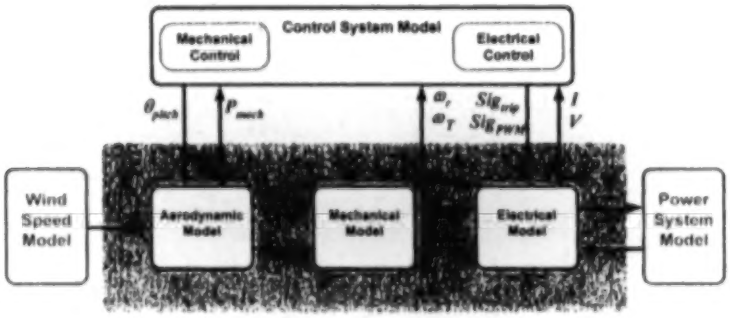

Figure 2.1: Single WTGS model

The aerodynamic model estimates the mechanical torque (T_{mech}) from the wind speed signal (ν_w), the turbine blade pitch angel (θ_{pitch}) and the generator rotor speed (ω_r) produced by the wind speed, the mechanical controller, and the mechanical model, respectively. With the present states of T_{mech} and T_{elec} (electrical torque), the mechanical model renews ω_r and ω_T along with the generator shaft torque (T_{rs}). In the electrical model, the updated T_{rs}, ω_r, Sig_{PWM} (electrical control signals), Sig_{trip} (electrical protection signal), and V_S (transmission line voltage) are used for determining the electrical operating conditions. These conditions include the various current and voltage values required by the electrical controller, and the generated active (P_{elec}) and reactive power (Q_{elec}) feeding to the external power system model. The following sections describe the three sub-models of the WTGS in more detail.

2.3 Aerodynamic Model

Under the given wind speed and turbine operating conditions, the aerodynamic model calculates the amount of kinetic energy that has been captured by the turbine. This calculation can get very involved via elemental analysis on the surface of each turbine blade [13]. In order to avoid the cumbersome elemental

analysis, the relatively simple (2.1) has been generally accepted for estimating the captured kinetic energy in the form of mechanical power (P_{mech}) [12, 13, 16, 32, 34–47].

$$P_{mech} = C_p(\lambda, \theta_{pitch})\frac{\rho}{2}R_T^2\pi\nu_w^3 \tag{2.1}$$

$$\lambda = R_T\left(\frac{\omega_T}{\nu_w}\right) \tag{2.2}$$

Table 2.1: Coefficients for Mechanical Power Computation

$\frac{\rho}{2}R_T^2\pi$	0.00159
R_T	56.6

The computation of P_{mech} depends on the power coefficient (C_p), air-density (ρ), turbine radius (R_T), and wind velocity (ν_w). C_p is a function of the turbine blade tip-speed ratio (λ) and the blade pitch angle (θ_{pitch}). This function describes the percentage of power extracted from the wind crossing the turbine blades, and it is unique for each turbine [13]. λ is calculated with (2.2), which requires the instantaneous ω_T and ν_w. θ_{pitch} is given from the mechanical controller depending on the electrical power generation.

The function $C_p(\lambda, \theta_{pitch})$ is usually expressed with a set of parabolic curves. The characterizing $C_p(\lambda, \theta_{pitch})$ curves of the GE $1.5MW$ WTGS, Fig. 2.2 (a), can be extrapolated using the curve-fitting formula (2.3) with the given $\alpha_{i,j}$ (Appendix A, Table A.1). Other fixed coefficients could be collected from Table 2.1.

$$C_p(\lambda, \theta_{pitch}) = \sum_{i=0}^{4}\sum_{j=0}^{4}\alpha_{i,j}\theta^i\lambda^j \tag{2.3}$$

To visualize the validity of (2.3), the $C_p(\lambda, \theta_{pitch})$ curves were reproduced using the MATLAB® programming language, Appendix B. As shown in Fig. 2.2 (b), the curve-fitting approximation has provided good estimates in the range of $2 < \lambda < 13$. Value of λ beyond the lower and higher boundaries represented very high and

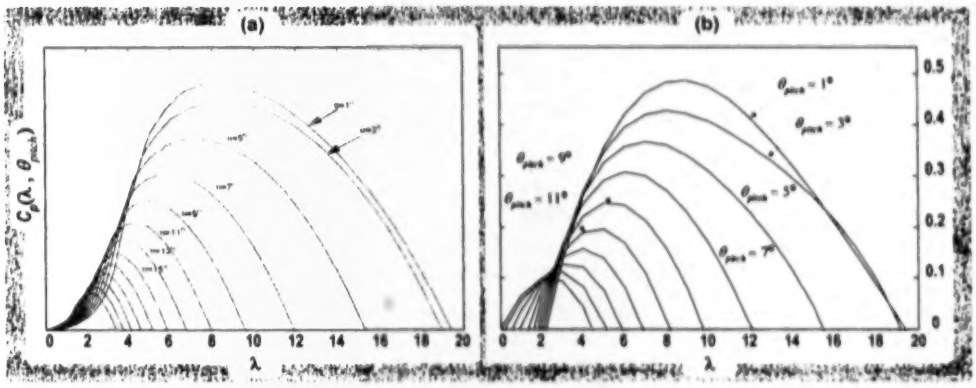

Figure 2.2: $C_p(\lambda, \theta_{pitch})$ curves: (a) specific curves of the GE $1.5MW$ WTGS; (b) reproduction of the GE $1.5MW$ WTGS $C_p(\lambda, \theta_{pitch})$ relation using curve fitting equation (2.3)

low wind speeds, respectively, that were outside the continuous operating region of the WTGS [34].

2.4 Mechanical Model

The mechanical model replicates the storage and transfer of mechanical energy within the WTGS. As seen from the complete mechanical drive-train model, Fig. 2.3, the mechanical energy stored in the rotating turbine is transmitted to the generator rotor through two shafts and a gearbox [12, 25, 34, 36, 40–42, 46, 47].

To reduce mechanical stress and wear, the turbine with the much larger inertia (H) must be operated at a lower speed. However, the generator cannot produce electrical power if the rotor is rotating at the same speed as the turbine. Therefore, a gearbox must be incorporated to transmit the mechanical power from the low-speed-high-torque end to the high-speed-low-torque end. With gear ratio f, the rotational speed of the rotor with the inertia H_g is proportionally increased to $\omega_r = \omega_T f$. Nevertheless, the shafts connecting between the masses and the gearbox have finite stiffness, and the conventional spring and damper model is employed to recreate the losses. The damping ratios and the spring constants are generally symbolized with D and K, respectively.

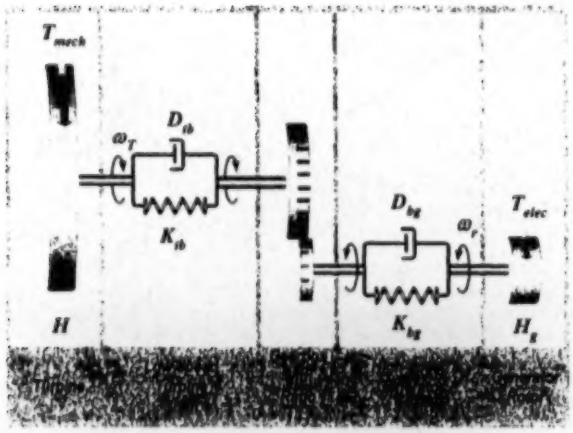

Figure 2.3: Complete mechanical model for the DFIG drive-train

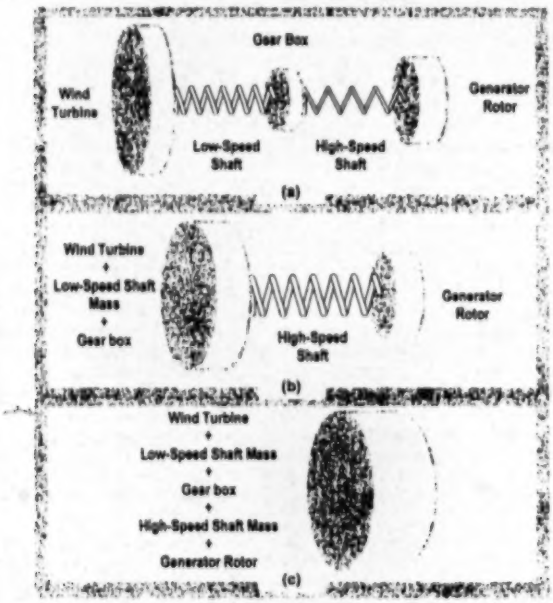

Figure 2.4: Mass spring models for the mechanical drive-train: (a) three-masses-two-spring model; (b) two-masses-spring model; (c) lumped mass model

The detail mechanical model can be readily represented by the three-masses-two-springs model, Fig. 2.4 (a). Consequently, the direct representation will create excessive demand on computational resources during the simulation of WTGS. In

the effort of balancing between simulation accuracy and speed, many researchers [10, 24, 25, 33] have adopted the two-masses-spring model, Fig. 2.4 (b). The three-masses model can be simplified to the two-masses model by converting the inertia of the turbine, the spring constant, and the damping ratio of the low-speed shaft to the high-speed side using (2.4)-(2.6) [25].

$$H_{high-speed} = \frac{H_{low-speed}}{f^2} \tag{2.4}$$

$$K_{high-speed} = \frac{K_{low-speed}}{f^2} \tag{2.5}$$

$$D_{high-speed} = \frac{D_{low-speed}}{f^2} \tag{2.6}$$

Nevertheless, it was claimed in [26] that the mechanical and electrical isolation established by the DFIG configuration would promise further reduction of the mechanical representation to a single lumped-mass model, Fig. 2.4 (c). The reason was that the fluctuations related to the shaft stiffness could be buffered by the operations of the electrical components when observing from the grid. Because the three-masses-two-springs model parameters for the GE $1.5MW$ WTGS were not publicly available, only the two-masses-spring and the lumped-mass mechanical model were implemented using the parameters given in Table. 2.2.

Table 2.2: Parameters for the GE $1.5MW$ two-masses-spring and lumped-mass model

H_T	4.32
H_g	0.62
K_{tg}	80.27 pu
D_{tg}	1.5 pu
ω_{base}	1.745 $\frac{rad}{s}$
H_{lump}	4.64

The two-mass model can be solved by:

$$\begin{aligned} -T_{elec} &= 2H_g \frac{d\omega_r}{dt} + T_{rs} \\ T_{mech} &= 2H_T \frac{d\omega_T}{dt} - T_{rs} \\ T_{rs} &= (\theta_r - \theta_T)K_{tg} + (\omega_r - \omega_T)D_{tg} \end{aligned} \tag{2.7}$$

where θ_T and θ_r were the angular position of the turbine and the generator found from the integration of ω_T and ω_r, respectively. H_T, K_{tg}, and D_{tg} denoted the combined inertia, spring constant, and damping ratio, respectively; and T_{rs} represent the torque exserted on the combined shaft. Graphical illustration of the actual implementation was shown in Fig. 2.5.

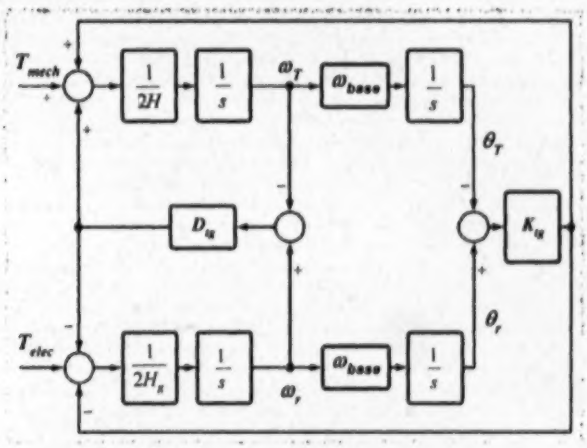

Figure 2.5: Two-masses-spring model implementation

The lumped-mass model could be solved using (2.8):

$$T_{elec} - T_{mech} = 2H_{lump} \frac{d\omega_{lump}}{dt} \tag{2.8}$$

However, the lumped inertia (H_{lump}) was found smaller than the direct sum of H_T and H_g given in Table 2.2. Possible explanation could be that the specification of H_{lump} has already taken the damping losses into account. The model implementation presented in Fig. 2.6 was much simpler, and no feed-back signal was involved.

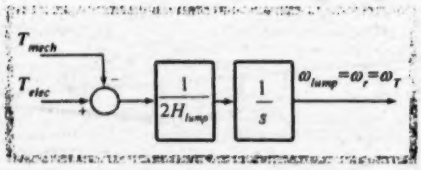

Figure 2.6: Lumped-mass model implementation

2.5 Electrical Model

The electrical model containing wide range of electrical components has received the most attention from researchers in the renewable energy field. This model could be generalized into two main parts: the wound rotor induction machine (WRIM) and the back-to-back converters (BBC), Fig. 2.7.

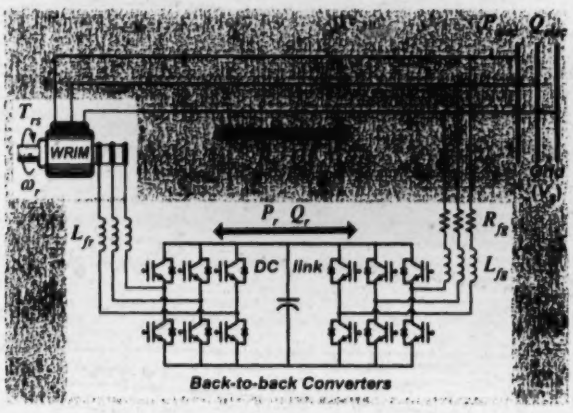

Figure 2.7: Doubly-fed induction generator connected to the grid

After receiving T_{rs} and ω_r from the mechanical model, the WRIM model determines its generated active (P_s) and reactive (Q_s) power at the stator terminal depending on the fixed grid voltage (V_s) and the controlled rotor terminal voltage (V_r). Through the secondary winding, the flow and magnitude of the WRIM rotor-side active (P_r) and reactive (Q_r) power are determined by controlling the BBC. The sum of the stator and rotor powers at the point of common coupling (PCC) yields the total electrical active (P_{elec}) and reactive (Q_{elec}) power transmitting to the external power system.

2.5.1 Wound-Rotor Induction Machine Model

The three-phase $1.67MVA\ 575V_{l-lrms}$ WRIM model shown in Fig. 2.7 was assumed to be symmetrical. By convention, the machine was modeled in the arbitrary qd frame [35, 44, 48]. Fig. 2.8 can be consulted for the relationship between the stationary three-phase stator axis abc_s, the rotating three-phase rotor axis abc_r, and the arbitrary axis qd. Since the three sets of axes are spanning the same two-dimensional space, the reversible transformation matrix (2.9) can be applied to project the parameters given in one axis system to another.

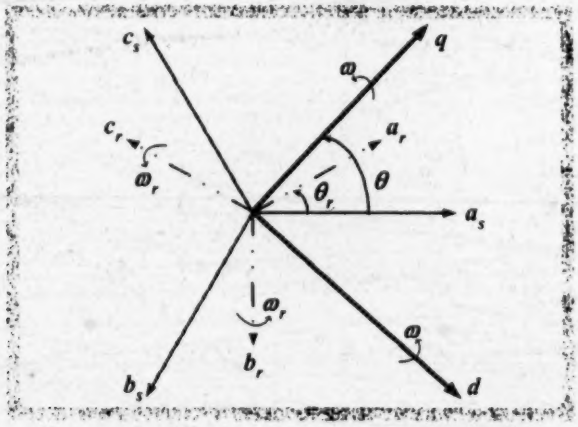

Figure 2.8: Reference frame for WRIM modeling

$$\begin{bmatrix} q \\ d \\ 0 \end{bmatrix} = \frac{2}{3} \begin{bmatrix} \cos\theta & \cos(\theta - \frac{2\pi}{3}) & \cos(\theta + \frac{2\pi}{3}) \\ \sin\theta & \sin(\theta - \frac{2\pi}{3}) & \sin(\theta + \frac{2\pi}{3}) \\ \frac{1}{2} & \frac{1}{2} & \frac{1}{2} \end{bmatrix} \begin{bmatrix} a_s \\ b_s \\ c_s \end{bmatrix} \tag{2.9}$$

When the qd frame rotates at ω, its angular position (θ) defined from the stationary a_s axis to the q axis is tracked by:

$$\theta = \int_0^t \omega + \theta_{(t=0)} \tag{2.10}$$

Because the abc_r axis is rotating at the same speed with the rotor, all the rotor-side parameters are expressed using this axis system. In order to transform the

rotor-side electrical properties to the qd frame, the transformation matrix would have to be modified to (2.12) to take into account of the relative angular position $(\theta - \theta_r)$ between the abc_r and the qd axis, where θ_r is defined by:

$$\theta_r = \int_0^t \omega_r + \theta_{r(t=0)} \tag{2.11}$$

$$\begin{bmatrix} q \\ d \\ 0 \end{bmatrix} = \frac{2}{3} \begin{bmatrix} \cos(\theta - \theta_r) & \cos(\theta - \theta_r - \frac{2\pi}{3}) & \cos(\theta - \theta_r + \frac{2\pi}{3}) \\ \sin(\theta - \theta_r) & \sin(\theta - \theta_r - \frac{2\pi}{3}) & \sin(\theta - \theta_r + \frac{2\pi}{3}) \\ \frac{1}{2} & \frac{1}{2} & \frac{1}{2} \end{bmatrix} \begin{bmatrix} a_r \\ b_r \\ c_r \end{bmatrix} \tag{2.12}$$

Following the transformation procedures in [48, 49], the equivalent circuit representation of a WRIM in the qd frame would be identical to the one presented in Fig. 2.9; the stator and rotor voltage equations would be similar to that given in (2.13).

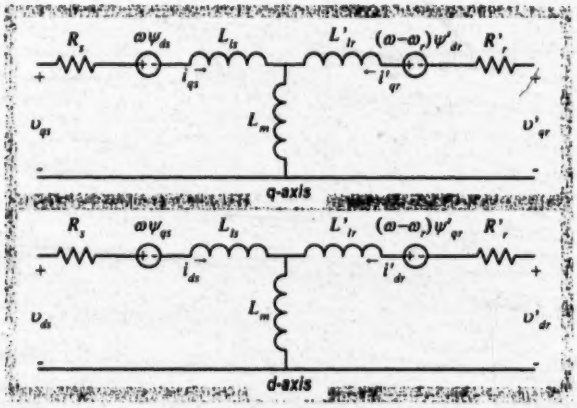

Figure 2.9: Induction machine model represented in the qd axis

$$\begin{aligned} \upsilon_{sq} &= R_s i_{sq} + \frac{d}{dt}\psi_{sq} + \omega\psi_{sd} \\ \upsilon_{sd} &= R_s i_{sd} + \frac{d}{dt}\psi_{sd} - \omega\psi_{sq} \\ \upsilon'_{rq} &= R'_r i'_{rq} + \frac{d}{dt}\psi'_{rq} + (\omega - \omega_r)\psi'_{rd} \\ \upsilon'_{rd} &= R'_r i'_{rd} + \frac{d}{dt}\psi'_{rd} - (\omega - \omega_r)\psi'_{rq} \end{aligned} \tag{2.13}$$

with

$$\begin{aligned}
\psi_{sq} &= L_s i_{sq} + L_m i'_{rq} \\
\psi_{sd} &= L_s i_{sd} + L_m i'_{rd} \\
\psi'_{rq} &= L'_r i'_{rq} + L_m i_{sq} \\
\psi'_{rd} &= L'_r i'_{rd} + L_m i_{sd} \\
L_s &= L_{ls} + L_m \\
L'_r &= L'_{lr} + L_m
\end{aligned}$$

The primed parameters symbolized the rotor electrical properties referred to the stator side. R_s and R_r represent the stator and rotor winding resistances, respectively. The leakage inductance of the stator and rotor are expressed by L_{ls} and L_{lr}, respectively. L_m is the magnetizing inductance bonding the stator and rotor winding. Magnetic flux in the different windings and axes are indicated with the corresponding ψ terms. Finally, the four derivative terms in (2.13) are included to estimate the transient properties.

Specific resistance and inductance values were not available in the manufacturer's document. Therefore, the hypothetical nameplate values given in Table. 2.3 were used to derive the necessary parameters for the WRIM [50].

Table 2.3: Hypothetical Nameplate Values and Final WRIM Parameters

Hypothetical Nameplate Values	**(per-unit)**
Full Load Efficency	0.95
Full Load Powerfactor	0.9
Full Load Slip	1.0
Starting Current	5
Final WRIM Parameters	**(per-unit)**
R_s	0.0256294
R'_r	0.0100649
L_{ls}	0.0998644
L'_{lr}	0.0998644
L_m	3.4785700

Since θ and ω are arbitrarily defined, the qd frame could be affixed to any references. Conventionally, there are three most convenient reference frames: stator, rotor and synchronous. When the qd axis is fixed to the stationary stator frame, ω becomes zero, and the terms $\omega\psi_{sd}$ and $\omega\psi_{sq}$ are eliminated from the stator-

side voltage equations in (2.13). If the q axis coincides with the a_r axis, ω equals ω_r, and the terms $(\omega - \omega_r)\psi'_{rd}$ and $(\omega - \omega_r)\psi'_{rq}$ are trimmed off the rotor-side voltage equations in (2.13). For power system studies, the analysis of the WRIM operation in steady-state can be conveniently conducted in the synchronous reference frame rotating at electrical speed $\omega_e = 2\pi 60(rad/s)$ [48].

2.5.2 Back-to-Back Converter Model

The electrical control exerted upon the WRIM is realized by the BBC. This device is constructed from two conventional six-pulse converters, which are connected back-to-back at their dc terminals with the shared buffering capacitor, Fig. 2.7. Switchings of the twelve insulated gate bipolar transistors (IGBTs) with their anti-parallel diodes on the six independent legs determine the functionalities of the BBC. All the switches and diodes are having the same on- and off-state resistance, $R_{on} = 0.001\Omega$ and $R_{off} = 1e6\Omega$, respectively. Since the study was focused on switching pattern, the switch-on forward voltage (V_{on}) and the switch-off extinction time (t_F) were set to zero to simplify the individual switch model.

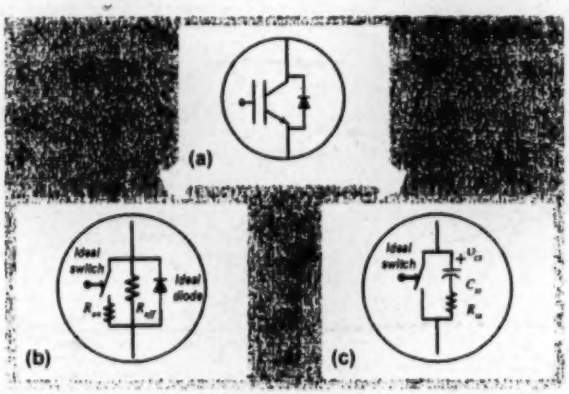

Figure 2.10: Switch model: (a) IGBT with anti-parallel diode; (b) custom switch model with ideal switch, diode, and resistors; (c) custom switch model with ideal switch, capacitor, and resistor

Usually, the IGBT and diode model are built-in to the modern EMTP software packages, i.e. PSCAD™/EMTDC™ and MATLAB®/SIMULINK®. In the case when the switch model is not already given, the two custom designed alternatives

shown in Fig. 2.10 can be considered. The first alternative, Fig. 2.10 (b), incorporates an ideal switch, a diode, and two resistors. When the ideal switch is *on*, the tiny R_{on} is in parallel with the huge R_{off}, and the effective resistance R_{eff} appears across the ideal diode is given by (2.14). As soon as the ideal switch is turned *off*, the resistance across the diode becomes R_{off}.

$$R_{eff} = \frac{1}{\frac{1}{R_{on}} + \frac{1}{R_{off}}} \approx R_{on} \tag{2.14}$$

In the second alternative, Fig. 2.10 (c), the switch is modeled with an ideal switch anti-paralleled with a RC branch. The polarized capacitor reproduce the effect of a diode by only allowing current flow into the positive terminal. When the ideal switch is closed, the downward current must flow against the capacitor voltage (v_{cs}), Fig. 2.10 (b). This resistive effect (R_{on-eff}) can be defined by (2.15). Re-opening the switch, the capacitor would be charged with the time constant of $\frac{1}{R_{ss}C_{ss}}$. For the specific switch model use in the research, the value of R_{ss} and C_{ss} are determined to be 5Ω and $3\mu F$ through trial and error. Verifications of the two models were given in Chapter 4.

$$R_{on-eff} = \frac{v_{cs}}{i_{switch-on}} \tag{2.15}$$

For the purpose of representing the collective behavior of a six-pulse converter, a switching function model can be utilized [51–57]. For this kind of behavior model, individual switches are not modeled. Instead, the model imitates the converter's interactions at AC and DC terminals using the controlled voltage and current sources, respectively. Detailed discussion and demonstration of the switching function model will be given in Chapter 4.

Since the BBC operation involves discrete switchings of the power electronics, current shaping filters are connected at both terminals to limit current distortions. Simple inductor (L_{fr}) filter connected between the rotor and the BBC ac terminal has the inductance of $0.005H$. The RL filter compensating the current flowing from the BBC to grid was consisted of the series connecting $0.01m\Omega$ R_{fg} and $0.001H$ L_{fg}.

2.6 Summary

By following the convention and the information collected for the popular GE $1.5MW$ WTGS, the model for a DFIG-based WTGS was divided into three sub-models: Aerodynamic, Mechanical, and Electrical. First, the interchanging signals among the individual sub-models were clearly defined. Then, the underlying mathematical formulations of each model and the simplification practice associated with these formulations were discussed. All the necessary parameters and the acquisition methods were provided along with the discussions.

3

DFIG-based WTGS Controller Design

3.1 Introduction

Control system determines the response of a WTGS under different operating conditions. A properly designed controller should force the WTGS to yield maximum power while ensuring the safety of the mechanical and electrical components involved. Therefore, the WTGS controller is sub-divided into mechanical and electrical controls, Fig. 3.1, to properly distribute the workload.

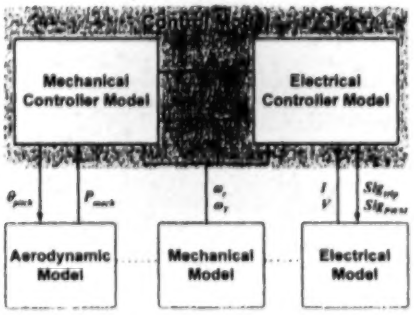

Figure 3.1: Controller model for single WTGS

According to the generator rotor speed (ω_r) and mechanical power (P_{mech}), the mechanical controller adjusts the turbine blade pitch angle (θ_{pitch}) to achieve optimal energy capture. The active electrical power (P_{elec}) estimation received from the electrical controller is used to define new speed reference for the turbine, and the speed is adjusted either by tuning θ_{pitch} or resetting the active power generation command P_{ord}. When measurements indicate hazardous operations, the Sig_{trip} is sent out to detach the WTGS from the grid sequentially.

The electrical controller is responsible for monitoring the current electrical power generation, and enacting the new power generation command. From the various current and voltage measurements, the active and reactive power power generated by the WRIM is continuously evaluated. These generation states are compared with the P_{ord} from the mechanical controller and the internal reference for the reactive power. Any difference found from the comparisons shall be mitigated by sending new command signals (Sig_{PWM}) to the electrical system. In the case of emergency or out of limit operation, the electrical system will be shut down by Sig_{trip}.

3.2 Background

For each manufacturing model of wind generator, there is a distinctive P_{mech} versus ω_r control curve, Fig. 3.2 [6, 12, 38–40, 42, 43, 47, 60, 61]. By referring to this curve, the controller commands the WRIM to produce maximum power at the appropriate ω_r. The cut-in and shut-down speed limits are mainly due to converter ratings [6,12,34,38], and this optimal speed range is defined to be $\pm 0.3pu$ of synchronous speed (ω_{sync}) for the GE $1.5MW$ WTGS. To overcome losses, the minimum power generation is set to $0.1pu$. For low-medium ν_w, the speed control will maintain the P_{elec} vs. ω_r relation on the curve between point **X** and **Y**. θ_{pitch} will be kept at zero for maximum power tracking. When ω_r reaches the optimal speed, the controllers enter speed-limiting mode until the generated power reaching the rated limit. Beyond point **Z**, blade pitch regulation dominates the control and limits the extracted P_{mech}. For very high ν_w, the pitch control will operate before

the turbine shut-down speed is surpassed.

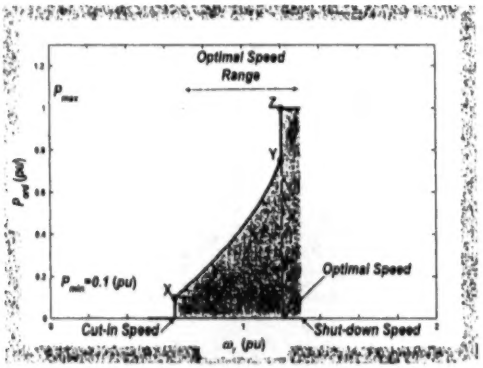

Figure 3.2: Power vs. generator rotor rotational speed control curve for GE1.5

The control curve (**X-Y**) is usually derived from the aerodynamics of the turbine. As discussed in the previous chapter, the available P_{mech} for energy conversion is calculated using (2.1), in which $C_p(\theta_{pitch}, \lambda)$ is a critical parameter. Provided that θ_{pitch} is held at zero before arriving point **Z**, the dependance of λ on the mechanical rotational speed allows the construction of a set of curves to describe the relationship between the speeds and the amount of mechanical energy available for conversion.

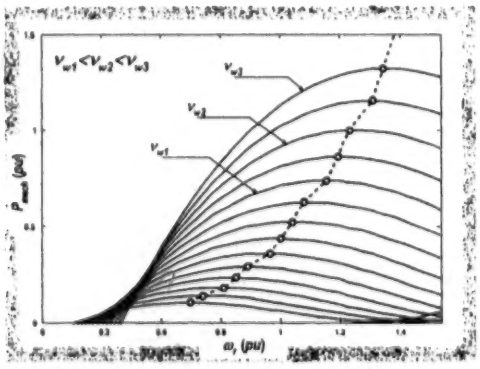

Figure 3.3: Synthesis of the power vs. rotor generator rotational speed control curve for GE1.5

As illustrated in Fig. 3.3, the available P_{mech} increases with the rising wind

speed. At different wind speed, there will always be a matching rotor speed allowing maximum power extraction. By connecting all the maximum point together, the optimal power versus rotor speed control curve is defined.

3.3 Mechanical Control

The representative mechanical control model was found from the documentation released by General Electric in 2003 [34]. All the control parameters presented in Fig. 3.4 were listed in Appendix C, Table C.1.

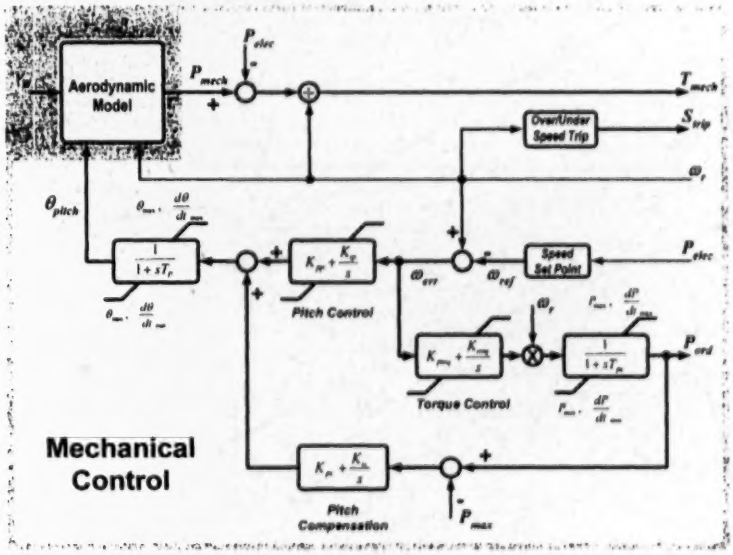

Figure 3.4: Mechanical control

The left hand side of Fig. 3.4 is the model of the turbine pitch control. The practical implication of this control is to regulate P_{mech} under the variable wind condition. When the available wind power is higher than the equipment rating, the turbine blades are pitched to reduce power extraction; as the wind power falls below the equipment's generation limit, the pitch angel will be kept at minimum to maximize power capturing. In either case, the controller senses the turbine speed and tries to return it to tracking the optimal generation curve in Fig. 3.2. The

dynamics of the pitch control are moderately fast, and can have significant impact on dynamic simulation results [25].

P_{ord} sent to the electrical control requests the converters to deliver certain amount of power to the grid. The electrical control may or may not be successful in implementing the power order. However, the electrical power actually delivered (P_{elec}) is returned to the mechanical control model for calculating the rotor speed setpoint. Because of the rapidly reacting power electronics, the dynamics of the electrical control is extremely fast.

Rotor speed is optimally controlled at $1.2pu$ but is reduced for power levels below 75% according to (3.1). When the system is not able to sustain the rotor speed within the optimal control range, the tripping signal (S_{trip}) is sent out to detach the generation unit from the grid.

$$w_{ref} = -0.67P^2 + 1.42P + 0.51 \tag{3.1}$$

3.4 Electrical Control and Design

The main function of electrical control is to manage the power generation from the WRIM. Because the WRIM allows access to the rotor winding through slip ring, controlled three-phase voltages can be injected into the rotor to fulfill various control schemes. Due to the flexibility and controllability of power electronics, the PWM controlled BBC was chosen to accomplish the voltage injector role.

3.4.1 The WRIM Control Fundamentals

A typical induction machine power-speed characteristic curve was shown in Fig. 3.5. The machine is generating when the rotor speed goes beyond its synchronous speed ω_{sync}. To accomplish linear response, the machine is operated along the shaded region [62].

The effect of the injected (v_r) could be better understood by referring to Fig. 3.6, in which the generation curves were flipped up-right [6, 13]. By referencing to the internal voltage E, Fig. 3.7, the injection of a positive voltage (v_{r1}) enables

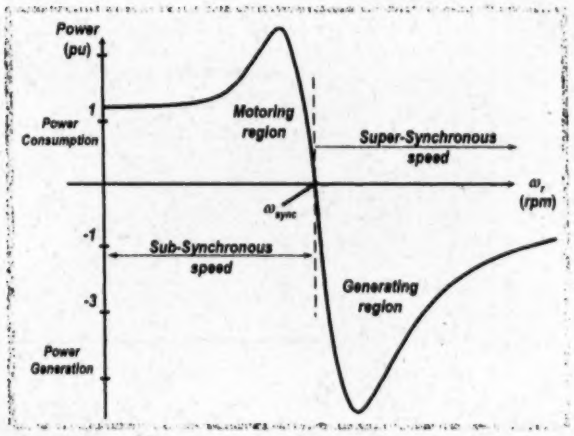

Figure 3.5: Induction machine power vs. generator rotor speed characteristic

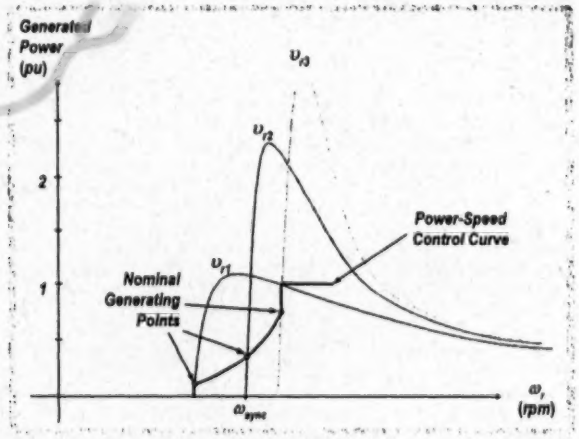

Figure 3.6: Effects of the injected voltages: v_{r1}=positve, v_{r2}=zero, and v_{r3}=negative

the WRIM to generate in the sub-synchronous speed region; as soon as the injected voltage turns negative (v_{r2}), the WRIM is producing power in the super-synchronous region. Therefore, the nominal generating points can be matched onto the power-speed control curve through properly tuning the rotor voltage.

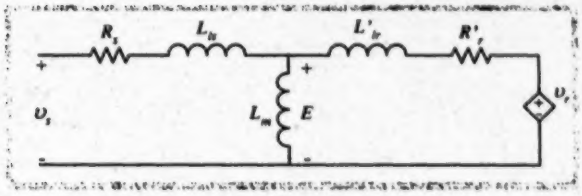

Figure 3.7: Per-phase v_r injection schematic in steady-state

3.4.2 Control and Operation of the Back-to-back PWM Converter

The BBC acts as the controlled voltage source injecting three-phase voltage (V_r) with variable frequency and amplitude to the rotor, Fig. 3.8. To interact with the three-phase electrical system on both sides, a total of twelve IGBT switches are required. Each leg, constructed from two inversely operating switches, is responsible of regulating the injected voltage to the phase that it is connected to.

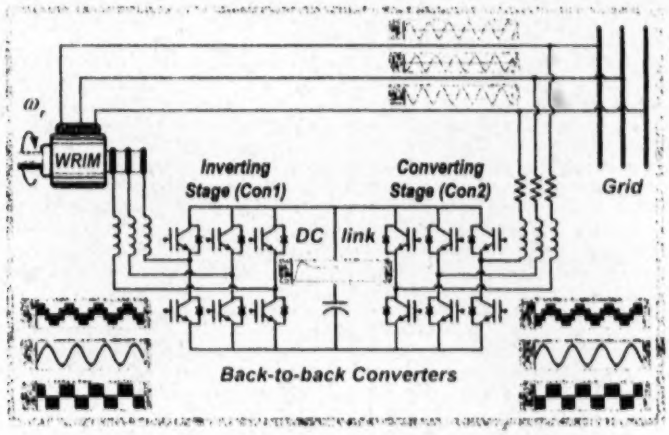

Figure 3.8: Electrical signals within the WTGS

Connected to the grid, the converting stage rectifies the sinusoidal three-phase V_S to the predefined dc voltage level across the $25000\mu F$ capacitor. The charged up capacitor will then act as the source for the inverting stage to produce the variable V_r. Control and operation of the two stages are considered highly independent.

Decoupled vector control is the underlying theory that brings the BBC into action. To apply the control theory, the measured three-phase abc current and

voltage values are transformed to a decoupled dq-axis system for the estimation of the parameters and the enaction of the control. The final control signals are transformed back to the abc form for the generation of individual switching signals for the twelve IGBT switches using the conventional PWM method.

3.4.2.1 Vector Control Theory

Vector control allows independent regulations on the system variables. Therefore, the control must be performed in the independent axis system. For the application of vector control theory, basic understanding in reference frame and frame transformation would be beneficial.

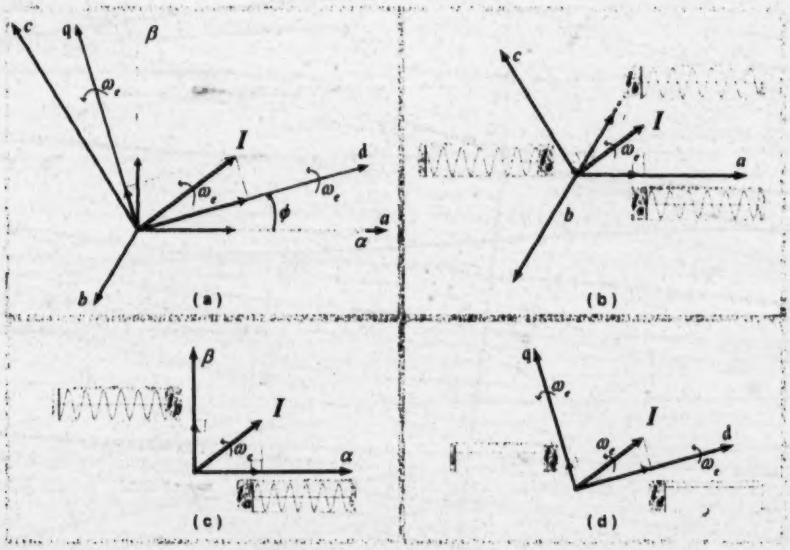

Figure 3.9: Reference frames for vector control: (a) Relationships among different frames; (b) stationary abc frame; (c) stationary $\alpha\beta$ frame; (d) rotating dq frame

For the three-phase electrical system, a set of instantaneous abc variables, either voltage or current, that sum to zero can be uniquely represented by a single point in a plane [63], Fig. 3.9 (b). By definition, the vector drawn from the origin to this point has a vertical projection onto each of the three symmetrically disposed phase axes, which corresponds to the instantaneous value of the associated phase variable. If the values of the phase variables change with frequency f_e, the

associated vector moves around the plane at the speed of $\omega_e = 2\pi f_e(rad/s)$. However, the heavy couplings between the phases of the abc coordinate system has created many obstacles for controller design. Fortunately, the fundamental theory of space vector has proven that a two-dimensional plane could be simply spanned by a set of orthogonal axes, such as $\alpha\beta$ and dq.

The $\alpha\beta$ ideology generally refers to the coordinate system that has one axis affixed to the stationary phase a of an electrical system, and the quadrature axis is leading by 90°, Fig. 3.9 (c). Projection of the abc variable is accomplished with the Park's transformation matrix (3.2). The '0' term was discarded since it would always be zero for the balanced system.

$$\begin{bmatrix} \alpha \\ \beta \\ 0 \end{bmatrix} = \begin{bmatrix} 1 & -\frac{1}{2} & -\frac{1}{2} \\ 0 & \frac{\sqrt{3}}{2} & -\frac{\sqrt{3}}{2} \\ \frac{1}{2} & \frac{1}{2} & \frac{1}{2} \end{bmatrix} \begin{bmatrix} a \\ b \\ c \end{bmatrix} \tag{3.2}$$

As illustrated in Fig. 3.9 (b) and (c), the vector components of I appeared as sinusoidal waveforms when observed from the stationary coordinates.

A dq axes rotating at ω_e is used to catch up with I, which is rotating at the same frequency. As illustrated by Fig. 3.9 (d), the zero relative speed between the current vector and the coordinate axes made the decoupled currents i_d and i_q appeared to be dc signals. By knowing the positional phase angle ϕ (3.3) shown in Fig. 3.9 (a), the dq frame current values were calculated using the Clark's transformation matrix (3.4).

$$\frac{d\phi}{dt} = \omega_e \tag{3.3}$$

$$\begin{bmatrix} d \\ q \end{bmatrix} = \begin{bmatrix} \cos(\phi) & \sin(\phi) \\ -\sin(\phi) & \cos(\phi) \end{bmatrix} \begin{bmatrix} \alpha \\ \beta \end{bmatrix} \tag{3.4}$$

By changing the coordinate system, controller design is tremendously simplified. It is more intuitive to control the dc signals in the dq frame, and simple gain controllers can be used to realize the commands on the decoupled signals.

3.4.2.2 PI Controller

Popularity of the PI controllers are characterized by their robustness and user-friendliness [64]. Equation (3.5) illustrated the transfer function of this controller in the continuous time s-domain. The application of this controller required the specifications of the proportional (K_p) and the integral (K_i) gains. Error (ε) signal would be proportionally magnified by K_p and linearly increased by K_i, Fig. 3.10. The final control signal resulting from the sum of the two amplification branches would drive the system to the desired operating point and ε to zero. By incorperating the feedback tracking feature, PI controller is made suitable for closed-loop control applications.

$$G(s) = K_p + \frac{K_i}{s} \tag{3.5}$$

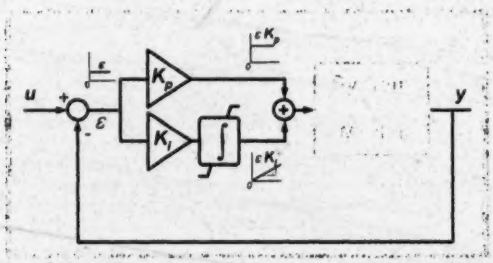

Figure 3.10: PI controller schematics

With bilinear transform (3.6), the discrete-time z-domain PI controller transfer function was found to be (3.7), where T was the sampling period.

$$s = \frac{2}{T}\frac{1 - z^{-1}}{1 + z^{-1}} \tag{3.6}$$

$$G(s) = K_p + \frac{K_i}{s} \implies G(z) = K_x\frac{z - a_x}{z - 1} \tag{3.7}$$

with

$$K_x = K_p + K_i\frac{T}{2} \;\; ; \;\; a_x = \frac{K_p - K_i\frac{T}{2}}{K_p + K_i\frac{T}{2}}$$

3.4.2.3 PWM Gating Pulse Generation

For the conventional way of generating PWM pulses [65, 66], a train of high frequency triangular carrier signal (S_C) and the sinusoidally varying control reference signal are required, Fig. 3.11 (a). S_C is usually formed in a high resolution function generator with the frequency fixed in kHz range and the amplitude limited between ± 1.

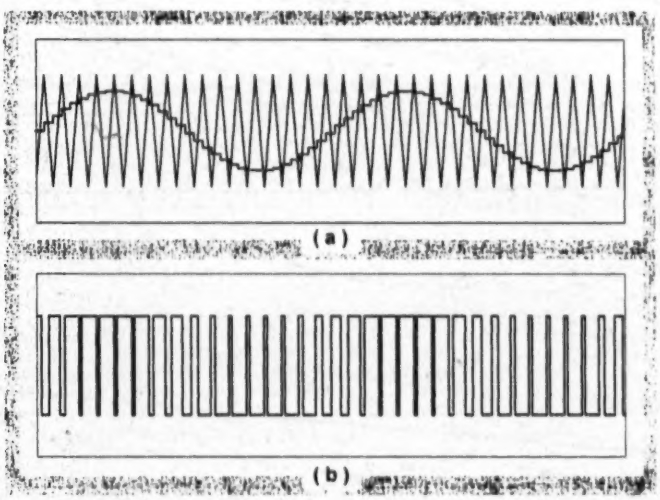

Figure 3.11: PWM signal generation: (a) comparison of the carrier and the discretized reference signal; (b) switching pulse stream for individual IGBT switches

After the PI controllers, the controlled dq-axis signals would be transformed back to the abc form using the inverse of (3.4) and (3.2) sequentially. By proportionally reducing the magnitude of the three-phase signals, they become the references that designate the *on*/*off* of the IGBT switches. When the reference signal is larger or equal to S_C, the upper switch of the corresponding leg, Fig. 3.8, would be turned *on* with the level high, Fig. 3.11 (b). Because of the inverse operation, the bottom switch on the same leg would be held *off* until the next comparison point.

In order to lighten the computational burden, the digital electrical controller is operated at a lower rate. As a result, the reference signal would have a lower

resolution, Fig. 3.10 (a). However, the carrier signal should retain its high resolution triangular shape to preserve operational accuracy. The multi-resolution requirement can be resolved using the "Sampling Technique" approach presented in [65,67].

3.4.3 Electrical Controller Design

Detailed electrical control schematics were not found from [34], and the given controller can only be used for a drastically simplified electrical system model. Therefore, a popular vector-control based controller design [35,38,39,44,63,68] was exploited for the study. For fine-tuning the controller parameters, conventional discrete-time root-locus method was applied.

3.4.3.1 Rotor-Side Converter Control

The stator-flux oriented indirect voltage control method has been adopted for maneuvering the rotor-side converter. In the synchronously rotating stator-flux (xy) frame, the stator side active (P_s) and reactive (Q_s) power could be analytically expressed in terms of the orthogonal rotor-side currents i_{ry} and i_{rx}, respectively [35,44]:

$$P_s = \frac{3}{2}|\vec{V}_s|i_{sy} = -\frac{3}{2}|\vec{V}_s|\frac{L_m}{L_s}i_{ry} \tag{3.8}$$

$$Q_s = \frac{3}{2}|\vec{V}_s|i_{sx} = \frac{3}{2}|\vec{V}_s|\frac{L_m}{L_s}(|\overrightarrow{I_{ms}}| - i_{rx}) \approx \frac{3}{2}|\vec{V}_s|\frac{L_m}{L_s}\left(\frac{|\vec{V}_s|}{2\pi f_s L_m} - i_{rx}\right) \tag{3.9}$$

The orientations of the control frames were illustrated in Fig. 3.12. Having the stationary $\alpha\beta$ frame as reference, the rotating rotor and stator-flux frames could be located by finding θ_r and ρ_s, respectively; θ_r was obtained from the decoder attached to the rotor shaft, and ρ_s were defined using (3.10)-(3.12):

$$i_{ms\alpha} = i_{r\alpha} + \frac{L_s}{L_m}i_{s\alpha} \tag{3.10}$$

$$i_{ms\beta} = i_{r\beta} + \frac{L_s}{L_m}i_{s\beta} \tag{3.11}$$

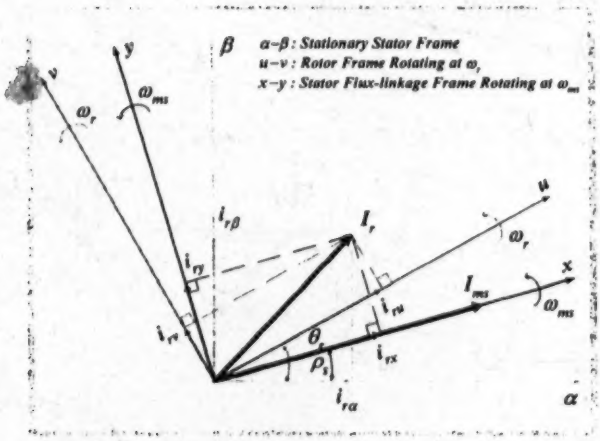

Figure 3.12: Relationships among the rotor-side converter control frames

$$\rho_s = \arctan \frac{i_{ms\beta}}{i_{ms\alpha}} \tag{3.12}$$

Since the range of arctan was limited between $(-\frac{\pi}{2}, \frac{\pi}{2})$, the actual implementation of (3.12) was modified as (3.13) to span the full 2π spectrum.

$$\rho_s = \arccos\left(\frac{i_{ms\alpha}}{|\overrightarrow{I_{ms}}|}\right) \times \frac{i_{ms\beta}}{|i_{ms\beta}|} \tag{3.13}$$

where

$$|\overrightarrow{I_{ms}}| = \sqrt{i_{ms\alpha}^2 + i_{ms\beta}^2} \tag{3.14}$$

Because the x-axis was overlapping with the apparently constant stator-flux current I_{ms}, (3.14), the rotor-side voltage relation in (2.13) were re-written as [35]:

$$\begin{aligned} v_{rx} &= R_r' i_{rx} + L^* \frac{d}{dt} i_{rx} - (\omega_{ms} - \omega_r) L_r^* i_{ry}' \\ v_{ry} &= R_r' i_{ry} + L^* \frac{d}{dt} i_{ry} + (\omega_{ms} - \omega_r)[(L_r' - L_r^*)|\overrightarrow{I_{ms}}| + L_r^* i_{rx}'] \end{aligned} \tag{3.15}$$

with

$$L_r^* = L_r' - \frac{L_m^2}{L_s}$$

where ω_r and ω_{ms} are calculated from the derivatives of θ_r and ρ_s, respectively.

Extracting the decoupling terms, the independent xy-axis control functions were ready for the controller parameter design:

$$\begin{aligned} \upsilon_{rx}^{*} &= R_r' i_{rx} + L^{*} \frac{d}{dt} i_{rx} \\ \upsilon_{ry}^{*} &= R_r' i_{ry} + L^{*} \frac{d}{dt} i_{ry} \end{aligned} \tag{3.16}$$

Eventually, the coupling terms, υ_{dx} and υ_{dy}, would be added correspondingly to improve the accuracy and independence of the control signals υ_{rx-ref} and υ_{ry-ref}:

$$\begin{aligned} \upsilon_{rx-ref} &= \upsilon_{rx}^{*} - (\omega_{ms} - \omega_r) L_r^{*} i_{ry}' &&= \upsilon_{rx}^{*} + \upsilon_{drx} \\ \upsilon_{ry-ref} &= \upsilon_{ry}^{*} + (\omega_{ms} - \omega_r)[(L_r' - L_r^{*})|\overrightarrow{I_{ms}}| + L_r^{*} i_{rx}'] &&= \upsilon_{ry}^{*} + \upsilon_{dry} \end{aligned} \tag{3.17}$$

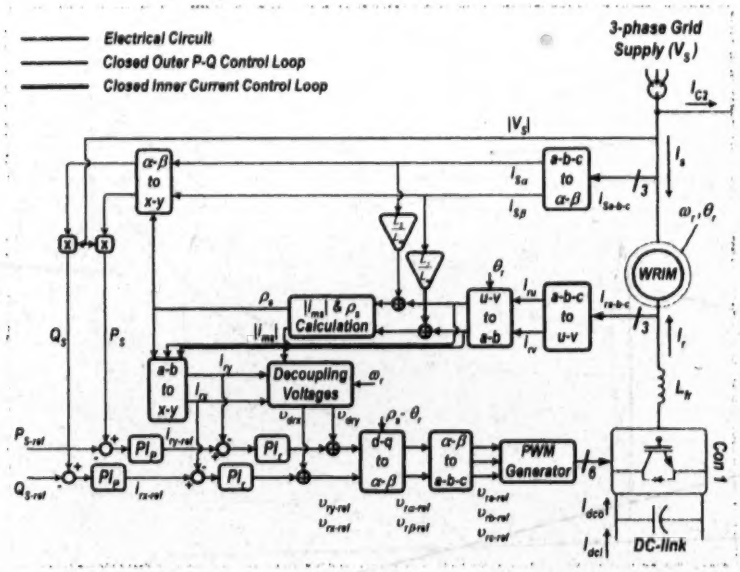

Figure 3.13: Rotor-side converter controller schematic

As shown in Fig. 3.13, after performing the reference frame transformation on the measured voltage (V_s) and currents (I_s and I_r), the instantaneous P_s and Q_s were calculated and compared with the references P_{s-ref} and Q_{s-ref}, respectively. The comparison errors would be fed into two independent PI controllers. Since the rotor current was indirectly regulated through the injection of controlled rotor

voltage, the current control values i_{ry-ref} and i_{rx-ref} were compared with the measured i_{ry} and i_{rx}, respectively; through the comparison, second set of error signals for voltage control were generated. After the last pair of PI controllers, v_{dry} and v_{drx} were added to the voltage control values to the improved independence between the x and y axis control values. Prior to the gating pulse generation, the sinusoidal reference signals v_{ra}, v_{rb}, and v_{rc} were obtained by backward transforming the xy control values into the abc_r frame.

3.4.3.2 Rotor-Side Inverter PI Controller Design

The behavior of the rotor-side converter (Con1) was characterized by the two sets of PI controllers. With the properly identified system transfer functions, the controller gains were specified using the conventional root-locus method under MATLAB®, Appendix D. Since there were two sets of PI controllers, two different system models were required.

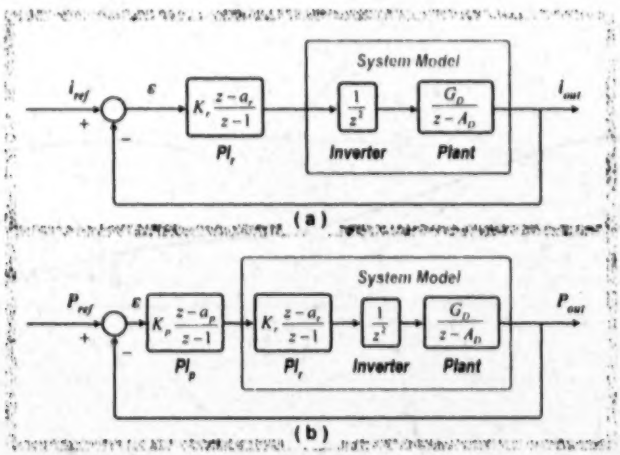

Figure 3.14: Block diagrams for PI controller design: (a) inner rotor current current control loop; (b) outer stator active and reactive power control loop

For the inner current control loop design, Fig. 3.13, the $25000\mu F$ DC-link capacitor was ignored since its time constant was much larger than the controller's $50\mu s$ sample-time (T_s). The fast switching converter was modeled by a delay of two sample periods [38, 39]. When looking into the rotor terminal of the WRIM, the s-

domain transfer function (3.18) was obtained by performing Laplace transform on (3.16):

$$F(s) = \frac{i_{rx}}{v^*_{rx}} = \frac{i_{ry}}{v^*_{ry}} = \frac{1}{sL^*_r + R'_r} \tag{3.18}$$

The z-domain equivalent (3.19) was derived using bilinear-transform. Because the system was assumed to be symmetrical, the transfer function were identical for both d and q axis, and the first set of PI controllers were assigned identical gain values.

$$F(z) = \frac{G_D}{(z - A_D)} \tag{3.19}$$

with

$$G_D = \frac{1 - A_D}{R'_r} \quad and \quad A_D = e^{-\frac{R'_r}{L^*_r} T_s}$$

With the simplified system models in place, the closed-loop model for inner current control, Fig. 3.14 (a), was then ready to undergo the root-locus design. By inspecting the transfer functions, total of four *poles* were found; a double-*pole* was created at zero, and the other two were scattered at 1 and A_D. However, there was only one *zero* created by a_r. After finding that A_D was also equal to 1, it was decided that the value of a_r must be very close to, but smaller than, 1 for the compensation of the double-*pole* located on the edge of the unit-circle in z-domain, Fig. 3.15. For the given reason, a_r was chosen to be 0.97.

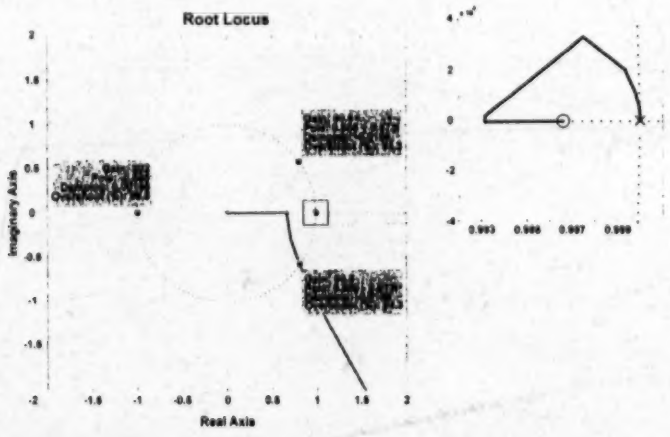

Figure 3.15: Root-locus for the inner rotor current control loop in z-domain

Once a_r was decided, the root-locus of the closed-loop model were plotted, Appendix D, in MATLAB®, Fig. 3.15. The boundary points indicated that K_r must be kept below 60.5 to retain the controller within the stable region. By selecting K_r equal to 2.02, the inner-loop system overshoot was suppressed to 0% with 100% damping. Combined with the $0.075s$ settling time, the system would response to the step changes in rotor current set-point smoothly, Fig. 3.16 (a).

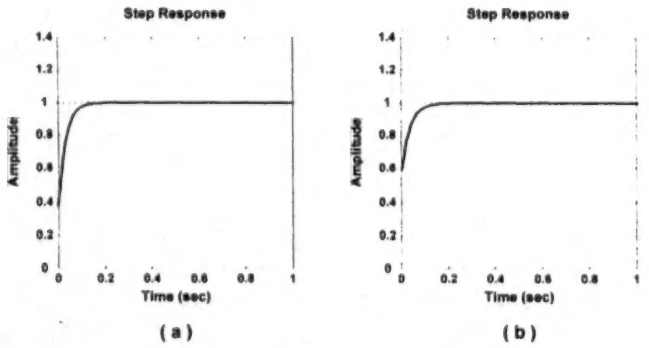

Figure 3.16: Designed step responses for the rotor-side converter: (a) inner-loop current response; (b) outer-loop active and reactive power response

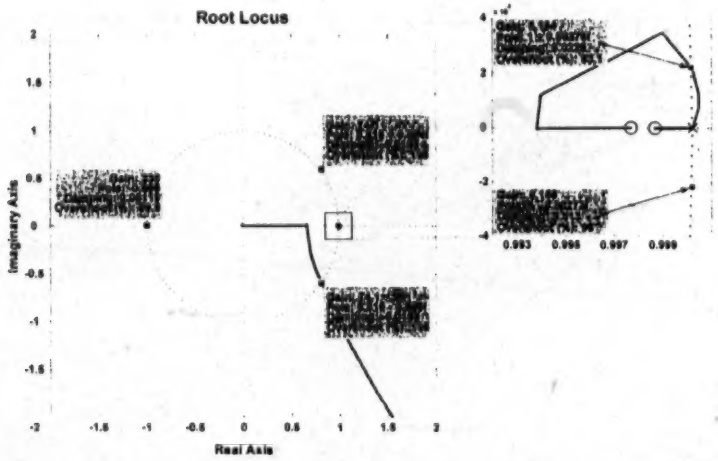

Figure 3.17: Root-locus for the outer active and reactive power control loop in z-domain

For the design of the second set of PI controllers, the system model need to be

modified to include the first set of PI controllers, Fig. 3.14(b). Since the additional PI controller introduced another *pole* at 1, a_p must be placed very close to a_r for the *zero-pole* compensation; 0.99 was chosen as a reasonable value. With the chosen a_p, root-locus was again applied for finding the proper K_p. The root paths in Fig. 3.17 showed that K_p must state above 0.164 to avoid stepping out of the unit-circle. Finally, K_p was assigned to be 0.88 to preserve the step response properties of the inner-loop system, Fig. 3.16 (b). This practice would prevent spiky power generation at the stator terminal.

3.4.3.3 Grid-Side Converter Control

The grid-side converter (Con2) vector control was very similar to that applied for Con1. However, the control objective was changed to regulating the DC-link voltage and the reactive power injected to the grid. The underlining control method was still the indirect voltage control, but the reference frame was changed to align with the grid-side voltage vector V_S, Fig. 3.18. To locate the rotating V_S, the stationary $v_{s\alpha}$ and $v_{s\beta}$ were needed for specifying the angular position θ_e, (3.20). The rotating dq frame would always be synchronized with the $60Hz$ V_S rotating at $\omega_e = 2\pi 60(rad/s)$.

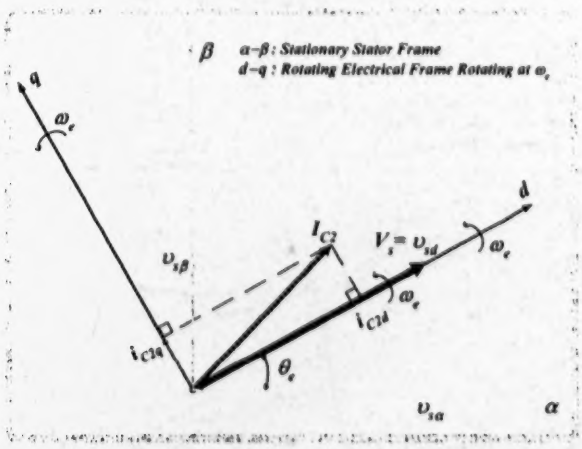

Figure 3.18: Relationships between the grid-side converter control frames

$$\theta_e = \arccos\left(\frac{\upsilon_{s\alpha}}{|V_s|}\right) \times \frac{\upsilon_{s\beta}}{|\upsilon_{s\beta}|} \tag{3.20}$$

As shown in Fig. 3.18, the d-axis was overlapped with V_S. This made the active (P_r) and reactive (Q_r) power through the converter directly proportional to the d and q component of the current I_{C2}, Fig. 3.19. When the losses caused by the filter and the converter switchings were ignored, the dc-side power can be related to the ac-side active power using (3.21) [38, 39, 44]. Here, it became obvious that the DC-link voltage can be proportionally controlled through i_{C2d}.

$$V_{dc} i_{dci} = 3\upsilon_{sd} i_{C2d} = 3|V_s| i_{c2d} \tag{3.21}$$

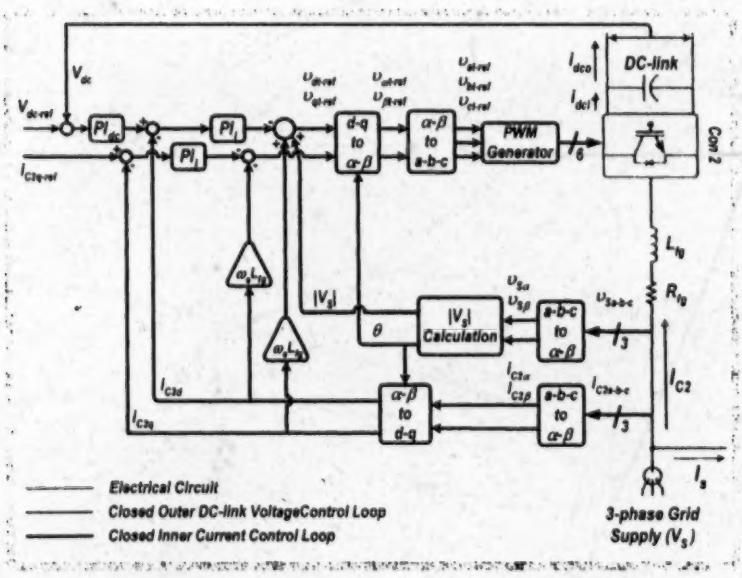

Figure 3.19: Grid-side converter controller schematic

By referring to the electrical circuit in Fig. 3.19, the dq frame voltage and current relation could be expressed as follow:

$$\begin{aligned} \upsilon_{sd} &= R_{fg} i_{C2d} + L_{fg} \frac{di_{C2d}}{dt} - \omega_e L_{fg} i_{C2q} + \upsilon_{C2d} \\ \upsilon_{sq} &= R_{fg} i_{cq} + L_{fg} \frac{di_{C2q}}{dt} + \omega_e L_{fg} i_{C2d} + \upsilon_{C2q} = 0 \end{aligned} \tag{3.22}$$

where v_{C2d} and v_{C2q} were the direct and quadrature axis voltage at the ac terminal.

After rearranging (3.22), the ac-side transfer function (3.23) was determined with the application of Laplace-transform. By inspection, the discretized z-domain function was very similar to (3.19) except that R_r' and L_r^* were replaced with R_{fg} and L_{fg}, respectively.

$$F(s) = \frac{i_{C2q}}{v_{C2q}^*} = \frac{i_{C2d}}{v_{C2d}^*} = \frac{1}{sL_{fg} + R_{fg}} \tag{3.23}$$

where

$$\begin{aligned} v_{C2q-ref} &= v_{C2q}^* - \omega_e L_{fg} i_{C2d} \\ v_{C2d-ref} &= v_{C2d}^* + \omega_e L_{fg} i_{C2q} + v_{sd} \end{aligned}$$

3.4.3.4 Grid-Side Converter PI Controller Design

For the indirect voltage control, two layers of PI controllers were required. The fast acting inner layer controlled the current following in the ac supply line. However, the outer dc voltage control-loop would act much slower because of the large time constant associated with the huge DC-link capacitance.

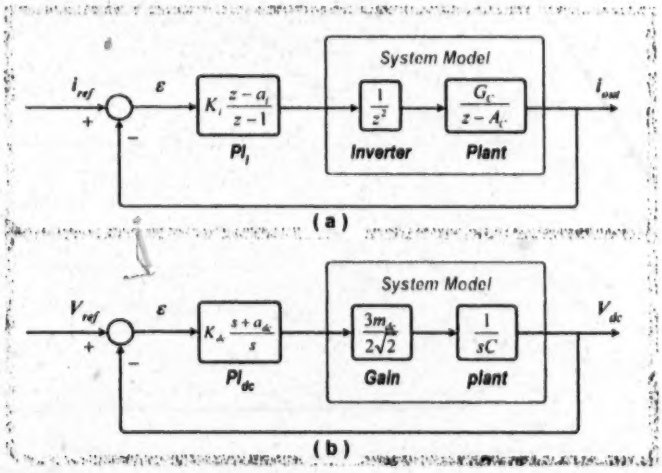

Figure 3.20: Block diagrams for PI controller design: (a) inner grid-side current control loop; (b) outer dc voltage control loop

Having the ac system model in place, the root-locus method was deployed for the inner layer current managing PI controller design. The design procedures were

identical as that was described in the previous sections. With the proper closed-loop system, Fig. 3.20 (a), MATLAB® was used to trace the paths of the roots, Fig. 3.21, Appendix E. One of the two *poles* located at the edge of the unit circle have been compensated by the *zero* created from the PI controller with a_i equal to 0.996591. However, the other *pole* would push one of the roots out of the unit-circle if the gain (K_i) exceeded the limit of 13.1. With the boundary in mind, K_i was selected to be 0.8799 for the most desirable step response, Fig. 3.22 (a). The over-damped characteristic and $0.012s$ settling time would ensure unruffled yet rapid current step-responses.

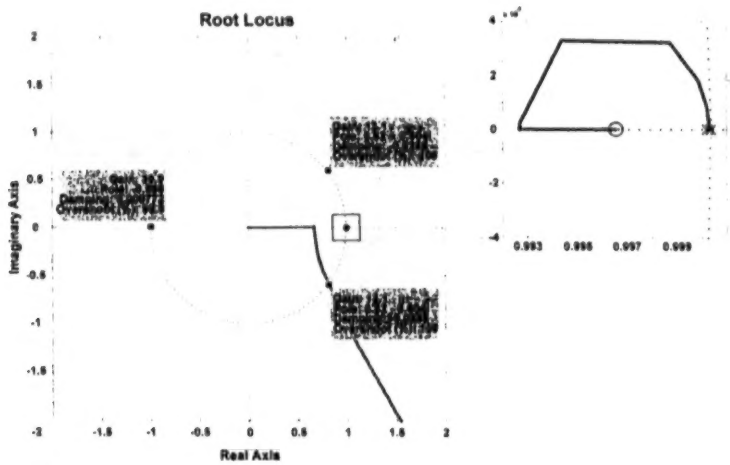

Figure 3.21: Root-locus for the inner grid-side current control loop in z-domain

Design of the dc voltage governing PI controller was much simpler as the system model only included the transfer function of the capacitance and a gain factor. The ac-side models were excluded due to their relatively small time constants. Because the large capacitance would result in very long closed-loop response, the dc voltage controller was designed in the continuous s-domain [38], Fig. 3.20 (b) ; and, the PI controller transfer function was rearranged to suit the design procedures, where $K_{dc} = K_p$ and $a_{dc} = K_i/K_p$. m_{dc} was defined as the ac/dc conversion ratio, and a typical value of 0.75 was assigned [38].

In Fig. 3.23, the root-locus plot indicated that the right-hand-plane *zero* created

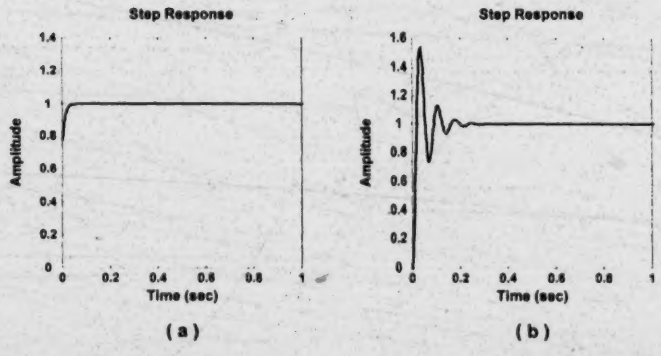

Figure 3.22: Designed step responses for the grid-side converter: (a) inner-loop current response; (b) outer-loop dc voltage response

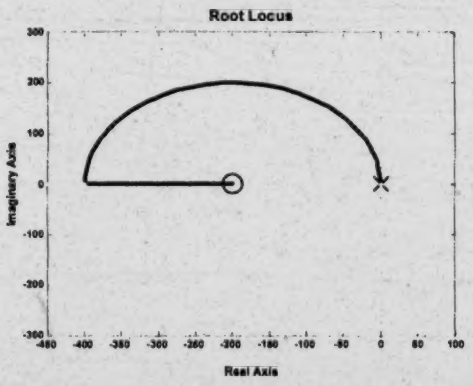

Figure 3.23: Root-locus for the outer DC voltage control loop in s-domain

by a_{dc} has successfully directed the double-*pole* from the origin toward the stable region of the s-domain. After many trials, the final values assigned to K_{dc} and a_{dc} were settled at 1.25 and 200, respectively. With this given PI controller specification, the DC-link capacitor would be charged up with an oscillatory overshoot, Fig. 3.22 (b). The reason for this design was to allow excess power flowing through the DC-link during the uninitialized generator startup. If the controller did not permit brief over-voltage across the capacitor, the in-rush starting demand from the WRIM rotor might collapse the dc voltage.

3.5 Summary

Control of the WTGS was accomplished through the cooperative operations of the mechanical and electrical controllers. The control objectives and limitations were clearly stated in this chapter. Since the complete mechanical control was found from the collected documentations, only the design of the electrical controller was presented. To help clarify the electrical controller design, the principles of vector control theory, the operations of the PI controller, the functionality of the PWM were briefly reviewed. Conventional root-locus method was employed for fine-tuning the electrical responses.

4

Off-Line and Real-Time DFIG Model Simulation, Comparison, and Validation

4.1 Introduction

For studying the impacts of integrating WTGSs to the existing power system, software simulations would be the logical first step. Aside from the cost and time benefit resulting from the faster model development cycle, fully digital simulations release researchers from the various limitations associated with the physical size of the components, the power rating requirement, and the availability of the devices.

Since the 60's when Dr. H. W. Dommel proposed the concept of electro-magnetic transient program (EMTP) for electrical system studies, computer simulation algorithm and tool development have been in the spotlight of power engineering research and study. Many organizations have packaged and commercialized their knowledge and techniques from decades of research and development in the form of simulation software. The current leading EMTP-type simulation software, such as PSCAD™/EMTDC™, MATLAB®/SIMULINK®, and EMTP-RV, provide users

with many built-in control modules, basic electrical elements, and mathematical tools to lessen the initial system modeling burden. With the given mathematical engine and computer language compiler, users can even develop their own model within the software environment.

Even if the basic principles are very similar, the implementation of the algorithms in different software packages can be different. These differences may be attributed to the dissemblance of the target audience and the technical background. Therefore, validation of the software model has became an important topic. Whether it is built-in or custom, the equivalent model should be simulated in different software packages, and the results must be compared. The comparison should show a high degree of agreement among the simulation results for the model to be validated. This is an very efficient method without the requirement of addition hardware implementation.

As the computing technology advance, more complicated calculation can be completed within an reducing amount of time. This advancement has encouraged researchers to explore into the realm of real-time (RT) simulation [67,69–71]. During RT simulation, memory access, communications, and dynamics computation of the entire model must be finished within the predefined time-step. In another words, RT simulation has a very strict requirement on the amount of time required for producing the response of the complete model. If the processing time exceeds the limit, the simulation will be defined as off-line. In order to meet the time restriction while still retaining enough accuracy to reflect the true behavior of the system under study, the RT model shall be simplified from the validated off-line model. Then the corresponding simulation results should be compared to ensure the optimized model is producing proper results in RT.

4.2 Background

Before illustrating the execution of the DFIG model for off-line and real-time simulations, in this section the readers would be prepared with the basics of the hardware and the software packages employed in the study. For the hardware,

general information regarding the configuration, installed software, and main functionalities were discussed. The general review for the software packages would indicate the release version used for the study, the available solvers, the solution method, and the expansion features of each software packages.

4.2.1 Hardware

The research study is conducted in the **R**eal-**T**ime e**X**perimental **LAB**oratory (RTX-LAB) of University of Alberta. The backbone of the lab is the state-of-the-art sixteen CPU real-time simulator shown in Fig. 4.1. This simulator is manufactured by OPAL-RT using commercial-off-the-shelf (COTS) components. The sixteen 3.0 GHz Hyper-Threading (HT) enabled Intel® Xeon™ CPUs built-up eight computational *nodes*. Each *node* has its own RT Linux® based operating system (OS) controlling 30 Giga-bits-per-second (Gbps) inter-*node* communication, 800MHz memory shared between the CPUs, external hardware interaction through the custom analog-to-digital and digital-to-analog I/Os, model loading, and real-time simulation execution. For more detail regarding this simulator, [71] can be consulted.

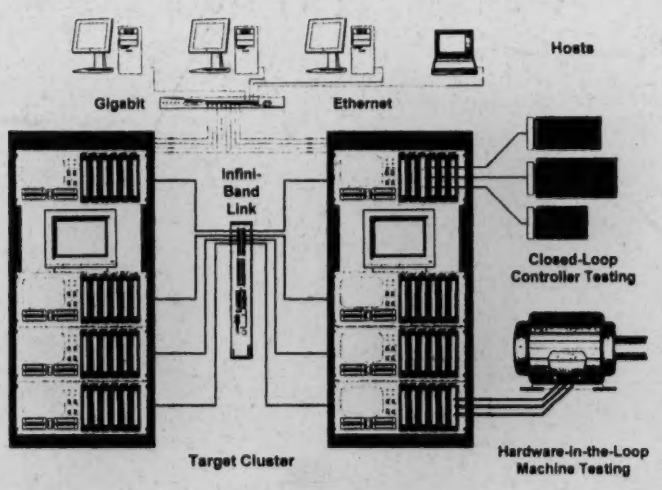

Figure 4.1: RTX-LAB real-time simulator hardware configuration

Four personal computers (PCs) equipped with 3.06GHz HT enabled Pentium® VI and 1G of memory are employed for off-line model development and validatioin. On these PCs the three aforementioned off-line simulation software packages were installed under Windows® XP. Besides model development, the PCs are also operated as the hosts for the RT simulator. When acting as a host, the PC would sent the pre-compiled executable to the simulator through the Gigabit Ethernet, and command the execution in RT.

4.2.2 Software Packages

Capitalizing on many years of research and technical know-how, Manitoba-HVDC Research Center, a subsidy of Manitoba Hydro, developed the PSCAD™/EMTDC™ software specifically for the power system related simulation studies. After four generations of refinement, version 4.01 of the software provides an intuitive graphical interface and a huge selection of built-in electrical and control models. Users were allowed to port their custom model through the Fortran code. The complete electrical model would be solved base on nodal-analysis with the fixed user-defined time-step. Active components and integrations modules are solved using Trapezoidal method. The simulation results from the PSCAD™/EMTDC™ are considered the benchmark [72, 73] in the research field since many of the built-in electrical models have been validated against the real world counterparts.

The relatively new EMTP-RV, version 1.1, is deployed by the power system research and development authority IREQ of Hydro Québec. The software sports its own unique graphical user interface (GUI), and the vast built-in components have made model development very time efficient. Custom models could be integrated through the cross-platform Java Script. When it comes to solving the integrals, the software allows its user to choose among three different discrete integration methods: the Backward Euler, Trapezoidal, and Backward Euler & Trapezoidal.

Developed by the MathWorks, Inc., MATLAB®/SIMULINK® V7.0.1 is a

powerful package used in different fields of research and industry. MATLAB® is the background mathematical engine that specializes in matrix operations and state-space model solutions. Through the SIMULINK® graphical interface, users could access the huge selection of built-in toolboxes to develop the electrical, mechanical and control system visually. If the provided toolboxes could not fulfill the specific need, user could always develop their own model through the S-function structure using either C, C++, Fortran, ADA or the MATLAB® language. The models developed in SIMULINK® could be solved with either variable or fixed time-step. Because of the model validation process, only the fixed-step solver was utilized with the `'discrete(no continuous state)'` option selected; this combination ensured that the Trapezoidal integration method was applied for solving the discretized linear electrical models.

The real-time simulation software package provided by OPAL-RT came in the form of three MATLAB®/SIMULINK® based toolboxes: ARTEMIS™, RT-EVENTS™, and RT-LAB™; and, the package required two OSs: Window XP and RT Linux®. ARTEMIS™ 4.0 provides additional discretization methods, improved solving algorithms, and a pre-computation mechanism to boost the overall performance of the SimPowerSystem (SPS) blockset that was built into MATLAB®/SIMULINK®. RT-EVENTS™ 2.4 targets specifically the power electronics modeling, operation, compensation, and optimization. RT-LAB™ 7.2.3 contains the modules that are required for the pre-compilation of the source code, RT hardware and software interface, and simulation result acquisition. Power system models could be developed off-line in the sophisticated SIMULINK® graphical environment under the popular Windows® XP. When the model optimizations are completed and verified with off-line simulations, the RT-LAB™ utility is used to transfer the pre-compiled source code into the RT Linux® operating system, which resides on the *nodes* of the simulator. The execution of the loaded model could be directly controlled through the Windows® based utility without dealing with the Linux® OS.

4.3 Off-line DFIG Simulation Result Comparison and Model Validation

For the DFIG-based WTGS, the WRIM and the power electronics switches are the two major electrical components that must be modeled and set up properly. Since all three off-line simulation software have their own built-in electrical models and each model provides different options, a comparable setup must be achieved before any further result comparison and validation process. In this section, two simple test models, namely the machine starting and capacitor charging, would be developed in the three off-line simulation packages for searching the proper use of the built-in induction machine and power electronic switch models, respectively.

4.3.1 Induction Machine Modeling

The simple induction machine (IM) starting case as depicted in Fig. 4.2 was incorporated for finding the proper WRIM parameter setups, as given in Appendix F. Since only the ratings of the WRIM were given in [34], the machine equivalent parameters were calculated from the hypothetical name plate values. These values were reasonably chosen to approximate a generator with very similar ratings. For the preliminary test, only the lumped-mass model was assigned to simplify the analysis.

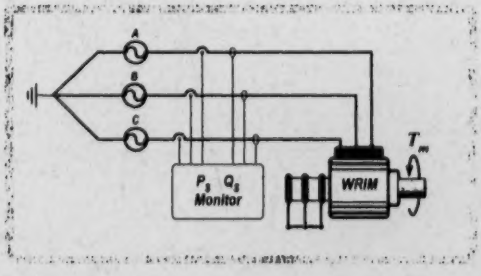

Figure 4.2: Un-controlled WRIM starting with shorted rotor terminals

Because this was a uncontrolled starting test, the rotor terminals were shorted together, and the rated voltage, $575V_{l-lrms}$, was directly fed to the stator terminals.

Constant mechanical torque of $-0.7pu$ was applied at the rotor shaft to increase the rotor speed from standstill and to generate active power at the stator terminals in steady-state. The model was simulated for $3s$ for capturing the starting transient and steady-state results of the stator-side active and reactive power.

In the first comparison, the simulation time-step was set to $50\mu s$. The stationary reference frame was selected for the IM models in SIMULINK® and EMTP-RV. Even the PSCAD™/EMTDC™ IM model had the reference frame fixed to the rotor, the simulation results were included as benchmarks.

The comparison shown in Fig. 4.3 revealed that the built-in SIMULINK® IM model was producing undesirable results at $t > 1s$. Unusually large transient oscillations were observed for the active power, and the steady-state of the reactive power was opposite of that produced from the other two software. These discrepancies triggered a sequence of comparisons with the variations in the model reference frame, numerical integration method, and the simulation time-step.

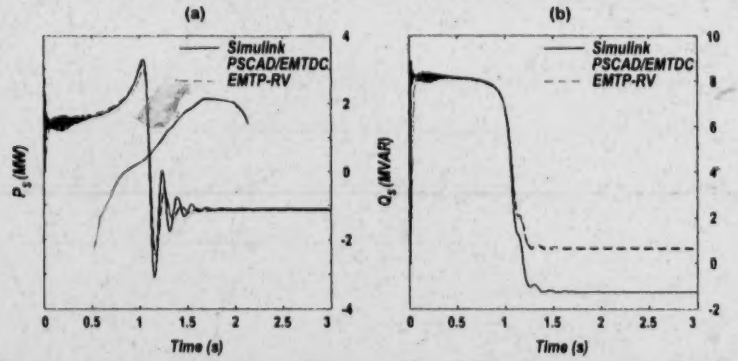

Figure 4.3: Simulation results for WRIM modeled in stationary reference frame: (a) stator-side active power; (b) stator-side reactive power

With simulation time-step kept constant at $50\mu s$ and the IM model reference frame switched to the rotor frame, the SIMULINK® IM model was able to produce results that were very closely agreeing with that generated from the other two software, Fig. 4.4. However, when changed to the synchronous reference frame, the transient phase delay was detected in the SIMULINK® results,

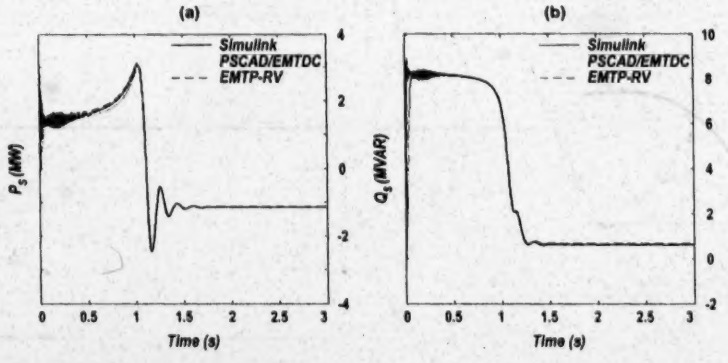

Figure 4.4: Simulation results for WRIM modeled in rotor reference frame: (a) stator-side active power; (b) stator-side reactive power

Fig. 4.5. The IM model from EMTP-RV was very robust; affirming with the PSCAD™/EMTDC™ results, the simulation result across all three reference frames were identical.

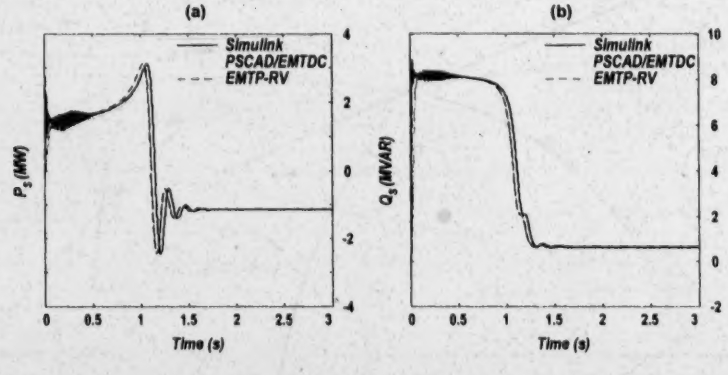

Figure 4.5: Simulation results for WRIM modeled in synchronous reference frame: (a) stator-side active power; (b) stator-side reactive power

Next, the impact of varying simulation time-step on the results was investigated. In the stationary and synchronous frames, the simulation time-step would have to be reduced to $5\mu s$ and $10\mu s$, respectively, for the SIMULINK® IM model to produce proper results. However, the smaller time-steps would create huge computational burdens on the hardware, and result in unreasonably long simulation time for a simple system involving IM model.

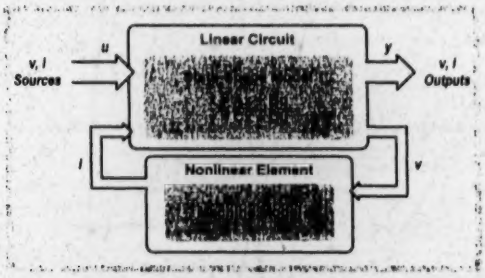

Figure 4.6: Linear electrical system model with nonlinear machine modeled as current feedback

The comparisons associated with the varying reference frame and simulation time-step lead to the conclusion that the integration method applied for the SIMULINK® IM model was the main cause of the discrepancies. It must be made clear that the IM model in SIMULINK® is not part of the linear state-space (SS) electrical model [71]. Because of its non-linear characteristic, the IM model was solved separately as a current feedback module constructed using the discrete components from the built-in SIMULINK® toolboxes, Fig 4.6.

To model the machine as a current source, (2.13) was rearranged into (4.1) for the computation of the stator and rotor currents from the corresponding fluxes.

$$\begin{aligned} i_{qs} &= \frac{(\psi_{qs} - \psi_{mq})}{L_{ls}} \\ i_{ds} &= \frac{(\psi_{ds} - \psi_{md})}{L_{ls}} \\ i'_{qr} &= \frac{(\psi'_{qr} - \psi_{mq})}{L'_{lr}} \\ i'_{dr} &= \frac{(\psi'_{dr} - \psi_{md})}{L'_{lr}} \end{aligned} \tag{4.1}$$

where

$$
\begin{aligned}
\psi_{qs} &= \int [v_{qs} - \omega\psi_{ds} - i_{qs}R_s]\omega_b dt \\
\psi_{ds} &= \int [v_{ds} + \omega\psi_{qs} - i_{ds}R_s]\omega_b dt \\
\psi'_{qr} &= \int [v'_{qr} - (\omega - \omega_r)\psi'_{dr} - i'_{qr}R'_r]\omega_b dt \\
\psi'_{dr} &= \int [v'_{dr} + (\omega - \omega_r)\psi'_{qr} - i'_{dr}R'_r]\omega_b dt \\
\psi_{md} &= L_{ad}(\frac{\psi_{ds}}{L_{ls}} + \frac{\psi'_{dr}}{L'_{lr}}) \\
\psi_{mq} &= L_{aq}(\frac{\psi_{qs}}{L_{ls}} + \frac{\psi'_{qr}}{L'_{lr}}) \\
L_{aq} &= L_{ad} = \frac{1}{\frac{1}{L_m} + \frac{1}{L_{ls}} + \frac{1}{L'_{lr}}}
\end{aligned}
$$

By default, the fluxes in (4.1) were solved using the Forward Euler integration method. As shown in Fig. 4.7 (a), Forward Euler is the least accurate elementary integration method that produces largest error, shaded area, when $f(x,t)$ is rapidly changing to a higher magnitude within the fixed sample time h. This explained why the selection of reference frames and simulation time-steps would affect the simulation results. As discussed in Chapter 3, the stator and rotor electrical values, due to the relative motion, are seemingly oscillating at higher frequencies when observed from the stationary frame. If the magnitude of the oscillations increased suddenly, the integration using Forward Euler method will result in enormous error.

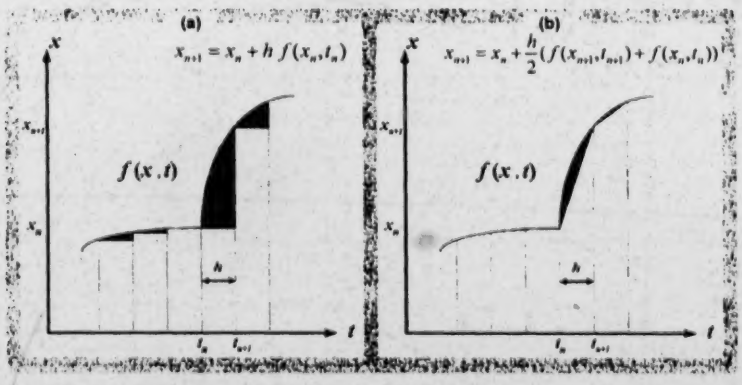

Figure 4.7: Elementary integration methods: (a) Forward Euler; (b) Trapezoidal

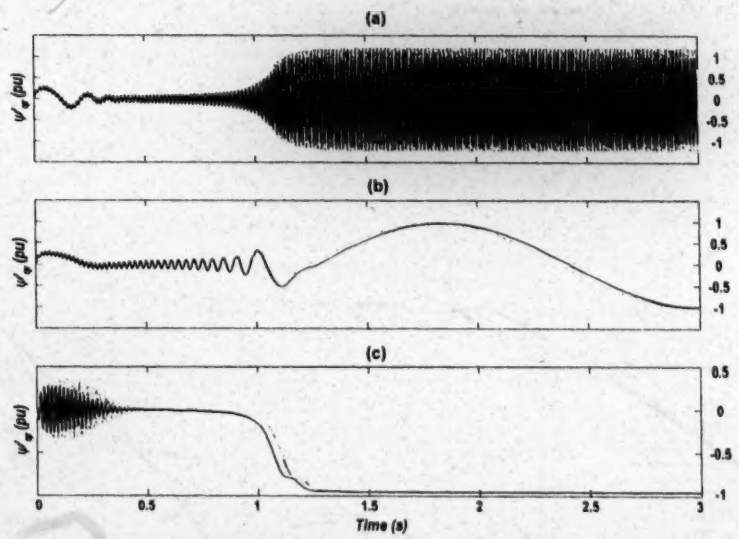

Figure 4.8: Observations of quadrature rotor flux integration using forward euler method: (a) in stationary reference frame; (b) in rotor reference frame; (c) in synchronous reference frame, where the black and grey lines indicate the results obtained with $5\mu s$ and $50\mu s$, respectively

Fig. 4.8 clearly demonstrated the combined effects of reference frame and time-step selection. The quadrature rotor flux (ψ'_{qr}) was measured in all three reference frames with the thin black lines and thick grey lines representing the results of Forward Euler integration obtained with the simulation time-step of $5\mu s$ and $50\mu s$, respectively. As a prove of the early statement, Fig. 4.8 (a) showed that the Forward Euler method had created substantial distortions to the integration of the high frequency high magnitude rotor flux in the stationary reference frame. In contrast, the integration error were much smaller when the same rotor flux was integrated in the rotor and the synchronously rotating reference frame, Fig. 4.8 (b) and 4.8 (c). In the rotor frame, the low amplitude high frequency component at $t < 1s$ was properly evaluated with $50\mu s$ time-step; when the flux amplitude increased moderately, the integration error was still relatively low. The transient phase error observed in the synchronous frame was caused by the cumulative error arising from the integration of the high amplitude high frequency flux component.

There are two solutions for the problems associated with the SIMULINK® IM model. The most obvious solution is to reduce the simulation time-step. However, smaller time-step will proportionally increase the total simulation time. By applying the second solution, all the integrations within the WRIM model would have to be solved using the more robust Trapezoidal method, Fig. 4.7 (b). Due to the acquisition of present state ($f(x_{n+1}, t_{n+1})$), integrating with Trapezoidal method demands much longer time than with Forward Euler method. However, this shortcoming could be offset by the allowable increase in simulation time-step. When simulating in the rotor and synchronous frame, the application of Trapezoidal method would allow the step-size to be increased beyond $1ms$ for this particular test case. Therefore, the best IM model setup in SIMULINK® is the combination of Trapezoidal method with either the selection of rotor or synchronous reference frame.

4.3.2 Multi-Mass Model

Using the machine starting setup, the proper implementation of the two-masses-spring model is investigated in this section. Out of the three software packages, only SIMULINK® does not provide the multi-mass (MMs) model interface. Fortunately, the MMs could be easily implemented with the elementary built-in blocks. The schematic shown in Fig. 2.5 was directly implemented in SIMULINK®, and the simulation results, Fig. 4.9 (a), were used as the benchmark for validating the MMs model in the other two software packages.

The IM model in PSCAD™/EMTDC™ required an external block for the activation of the MMs mechanical dynamic. However, the IM model that came with the software could not interface with the external block correctly. After replacing the original IM model with the revised one from PSCAD™/EMTDC™ technical support, the simulation results for electrical torque (T_{elec}) and rotor speed (ω_r) were found to be very close to that obtained from SIMULINK®, Fig. 4.9 (b).

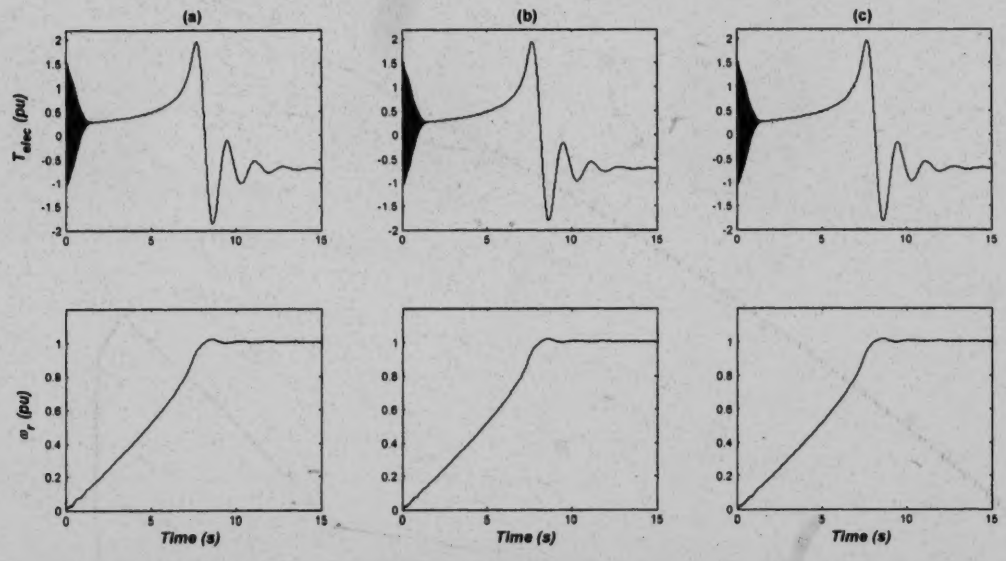

Figure 4.9: Electrical torque and rotor speed of the multi-mass system simulated in: (a) MATLAB®/SIMULINK®; (b) PSCAD™/EMTDC™; (c) EMTP-RV

$$K_{S.I.} = K_{pu}(\frac{p}{\omega_b})^2 P_{rated} \tag{4.2}$$

$$D_{S.I.} = D_{pu}(\frac{p}{\omega_b})^2 P_{rated} \tag{4.3}$$

EMTP-RV had the MMs feature integrated into its IM model. However, the spring constant (K) and damping (D) must be entered in S.I. unit. To convert the data from the per-unit system used in PSCAD™/EMTDC™ to S.I. unit, (4.2) and (4.3) are used, where p represents number of pole pairs and ω_b equals to $2\pi 60$. With correct data, the two mass IM model in EMTP-RV successfully produced the mechanical dynamics that had been generated from both SIMULINK® and PSCAD™/EMTDC™, Fig. 4.9 (c).

4.3.3 Power Electronics Modeling

A capacitor charging simulation was setup to validate the power electronic switch models provided by PSCAD™/EMTDC™, MATLAB®/SIMULINK®, and EMTP-

RV, and to verify the grid-side converter controller design presented in the previous chapter. The schematic was identical to the grid-side converter setup shown in Fig. 3.19. Three-phase supply voltage from an ideal source would be rectified to charge up the dc capacitor. However, the dc voltage (V_{dc}) should only be controlled by the direct axis current (i_d) from the source. By decoupled vector control, the quadrature current (i_q) should be manipulated without creating noticeable interference on the controlled V_{dc}.

Setting up the electrical model in PSCAD™/EMTDC™ and SIMULINK® was simplified with the built-in discrete IGBT and Universal Bridge models as shown in Appendix G Fig. G.1 and Fig.G.2, respectively. In EMTP-RV, the setup was more challenging since only the ideal switch model was provided. As illustrated in Fig. 2.10 (b), the combination of an ideal switch, a discrete diode, and two resistors could sufficiently model the properties of the power electronic switch in its different operating states, given in Appendix G Fig. G.3. However, a unique 'Simultaneous Switching' block must be included to compensate for the switchings occurring between the simulation time-steps. In PSCAD™/EMTDC™ and SIMULINK®, switching compensation features were activated in the background.

The reason for incorporating switching compensation techniques for the simulation studies involving fast switching power electronics was due to the finite simulation time-step [67, 74]. When a switching event is detected between the fixed sampling time instants, the simulation will be halted, and interpolation mechanism would recalculate the network equations without advancing the time-point.

The vast built-in control, mathematics, and logic libraries provided by the three software packages had made the controller model realization straightforward. Although the built-in libraries had different interfaces, the available options and features were intuitively similar, Appendix G Fig. G.4 - Fig. G.6.

The simulation time-step was fixed to $50\mu s$, which provided reasonably high resolution for the $1080Hz$ carrier signal associated with the PWM pulse generation. As shown in Fig. 4.10, the simulation results from the three software packages

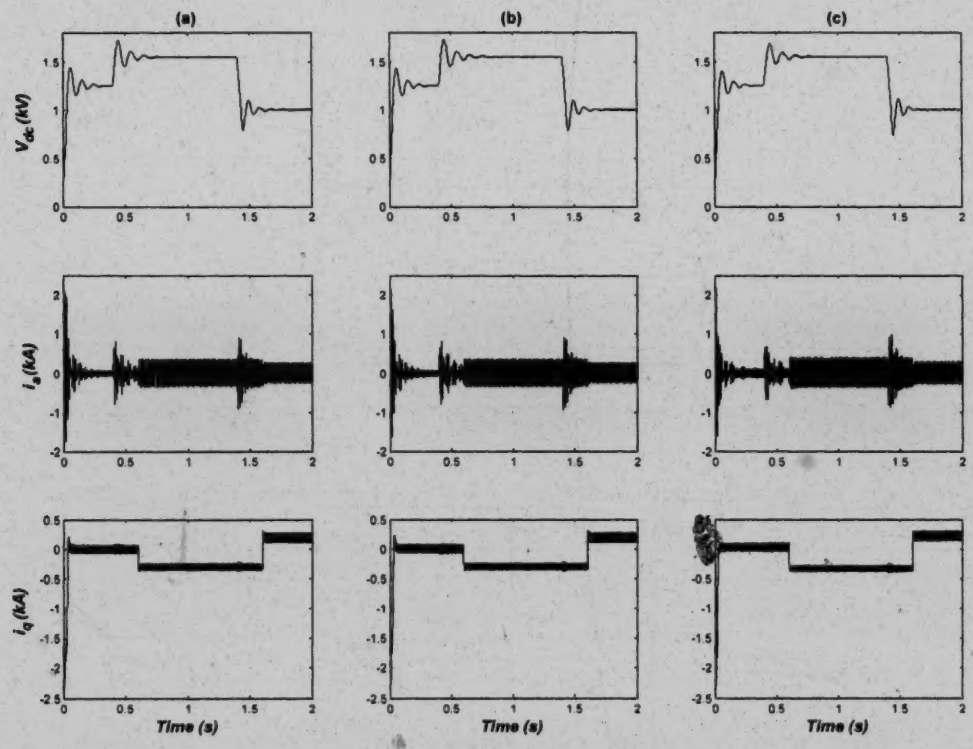

Figure 4.10: Control of grid-side converter voltage and current simulated in: (a) PSCAD™/EMTDC™; (b) MATLAB®/SIMULINK®; (c) EMTP-RV

were very similar, and the responses were closely resembling the designed characteristics. Especially for V_{dc}, the overshoot and the oscillatory settling pattern closely agreed with the designed step-response shown in Fig. 3.22 (b). Initially the DC-link voltage was charged up to $1.25kV$. After reaching the steady-state, step commands given at $t = 0.4s$ and $1.4s$ had successfully altered V_{dc} to $1.55kV$ and $1kV$, respectively.

Following a step-up command, under-damped spikes were found in the results of i_q collected from PSCAD™/EMTDC™ and MATLAB®/SIMULINK®, Fig. 4.10 (a) and 4.10 (b). This slight difference from the designed response, Fig. 3.22 (a), was only an indication renouncing that the model applied for the controller design was simplified. From EMTP-RV, the over-damped i_q response could be benefited from

the discrete resistor used for switch modeling, Fig. 4.10 (c). The initially zero i_q was first stepped down to $-0.3kA$ at $t = 0.6s$. Obeying the step-up command at $t = 1.6s$, the current was rapidly pushed up to positive $0.2kA$.

The results of i_a were included to demonstrate how would the changes in V_{dc} and i_q affect the current waveform observed in the *abc* frame. Since the simulation results were nearly identical, and no divergency nor uncontrollable situations were detected from the simulation results generated by any of the three software packages, the power electronic switch model and the converter controller design were validated.

4.3.4 Complete DFIG Configuration

The systematic step-by-step approach has prompted the final development and validation of the complete DFIG configuration in all three software packages. Benefited from the previous experiences and results, the complete model was finished with the addition of the rotor-side converter and its controller model. However, there was some minor difficulties stemming from the limitations of the software tools. In this section, the solutions for overcoming these limitations would be discussed along with the simulation results for the complete DFIG model. Since there were power electronics involved, the simulations were run with a $50\mu s$ simulation time-step in all three softwares. Close attention has been made to ensure correct data entry and to preserve the exactness in simulation parameter setup.

Similar to redrawing the schematics using the built-in graphical models, the proposed DFIG model and electrical controllers were directly implemented in PSCAD™/EMTDC™, Appendix H Fig. H.1 and Fig. H.2, respectively. Clearly shown in Fig. 4.11 (b), the stator side active (P_s) and reactive (Q_s) power, and DC-link voltage (V_{dc}) were closely following the step commands. A step change in any one of the three parameters occurred only when the other two parameters were in their steady-states, e.g. the step-change in P_s only happened when Q_s and V_{dc} were settled to their steady-states. In this way, the merit of decoupled vector

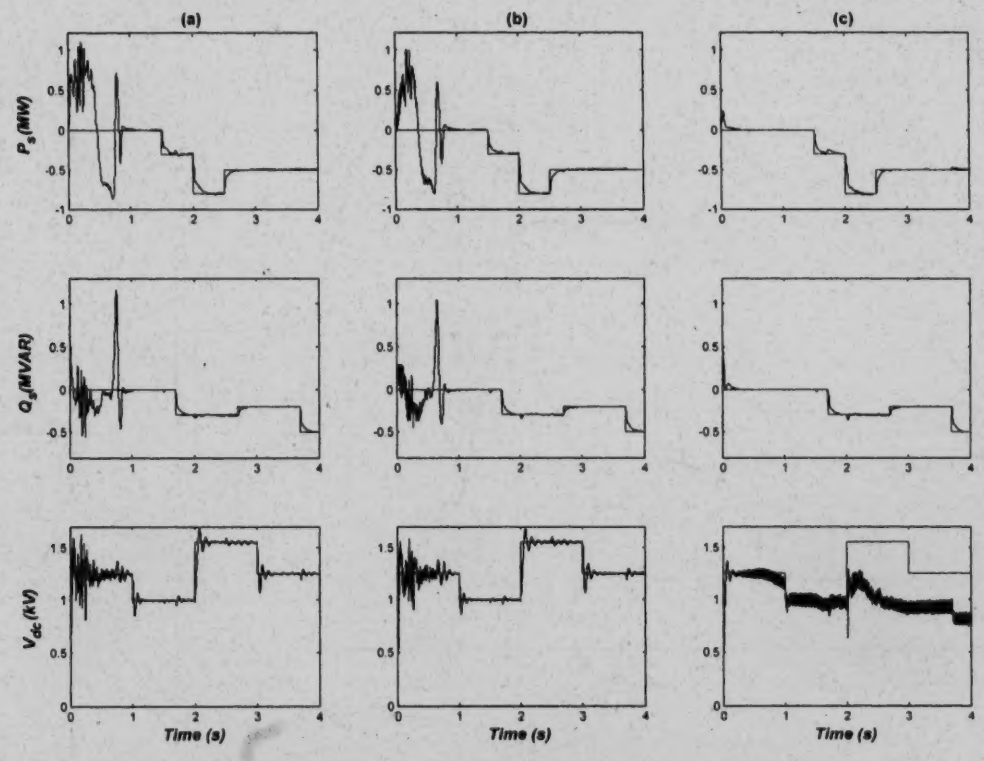

Figure 4.11: DFIG stator-side active and reactive power, and DC-link voltage simulated in: (a) MATLAB®/SIMULINK®; (b) PSCAD™/EMTDC™; (c) EMTP-RV

control could be better appreciated.

After the un-initialized generator starting transient, P_s and Q_s were steadily maintained at zero until their first step-command occurred. At $t = 1.5s$, the DFIG was ordered to generate $0.3MW$ of active power from the stator. $0.2s$ later, Q_s was adjusted to $-0.3MVAR$. Shortly after Q_s reached its steady-state, P_s was furthered to $-0.8MW$ at $t = 2.0s$. The final adjustment of P_s within the $4s$ simulation occurred at $t = 2.5s$, and the final state was at $-0.5MW$. For Q_s the last two step commands came at $t = 2.7s$ and $t = 3.7s$ with the final values of $-0.2MVAR$ and $-0.5MVAR$, respectively.

By observation, a small pulse was resulted in the P_s waveform whenever a step-change of operating point was performing on Q_s; similarly, the step-changes in

P_s have correspondingly caused pulses in the waveform of Q_s. This phenomena was caused by the coupling voltages v_{dx} and v_{dy} shown in Fig. 3.13. However, the extremely short pulses did not cause any problem in controlling the power quantities.

The disturbances in V_{dc} were not cause by the coupling in the control algorithm since the controller were totally independent. Rather, the coupling was in the electrical system at where the two converters shared the same DC-link. The sharp changes in P_s and Q_s created abrupt vibrations in rotor current (I_r). These vibrations in I_r was then directly reflected across the dc capacitor voltage. Despite the disturbances, the V_{dc} has been accurately controlled to the desired levels through the simulation. At the instances of $t = 1.0s$, $2.0s$, and $3.0s$, V_{dc} has obeyed the step-command changed from its initial steady-state of $1.25kV$ to the designated levels of $1kV$, $1.55kV$, and $1.25kV$, respectively.

The implementation of the IM model as a current source in SIMULINK® has triggered the fatal error when the current filtering inductors (L_{fr}) were connected to the rotor terminals, Fig. 3.13. In SIMULINK®, current source models were not allowed to be connected in series with any inductive models. Without L_{fr}, the initial line currents between the rotor-terminal and the BBC would become unbounded. In order to save time from developing of a custom IM model, L_{fr} was integrated into the machine model, Appendix H Fig. H.3 and Fig. H.4. The filter inductance was summed to the rotor equivalent inductance (L_r) in per-unit. This solution was justified because the electrical dynamics were mainly determined by the controller, and the mechanical dynamics were dominated by the larger turbine mass [42, 43]. By comparing the SIMULINK® simulation results to that obtained from PSCAD™/EMTDC™, Fig. 4.11 (a) and 4.11 (b), it was clear that the integration of L_{fr} had minimal effect on the overall simulation results.

The available version of EMTP-RV was found unsuitable for the study of power system involving complicated power electronics devices, and the technical support from EMTP-RV had confirmed that the 'Simultaneous Switching' block was still in the development stage for compensating complex multiple switchings. In the

attempt to rectify this shortfall, the 'Simultaneous Switching' block along with the proven switch model presented in Fig. 2.10 (b) were discarded, and the power electronic switches were re-modeled with the second alternative model given in Fig. 2.10 (c), Appendix H Fig. H.5.

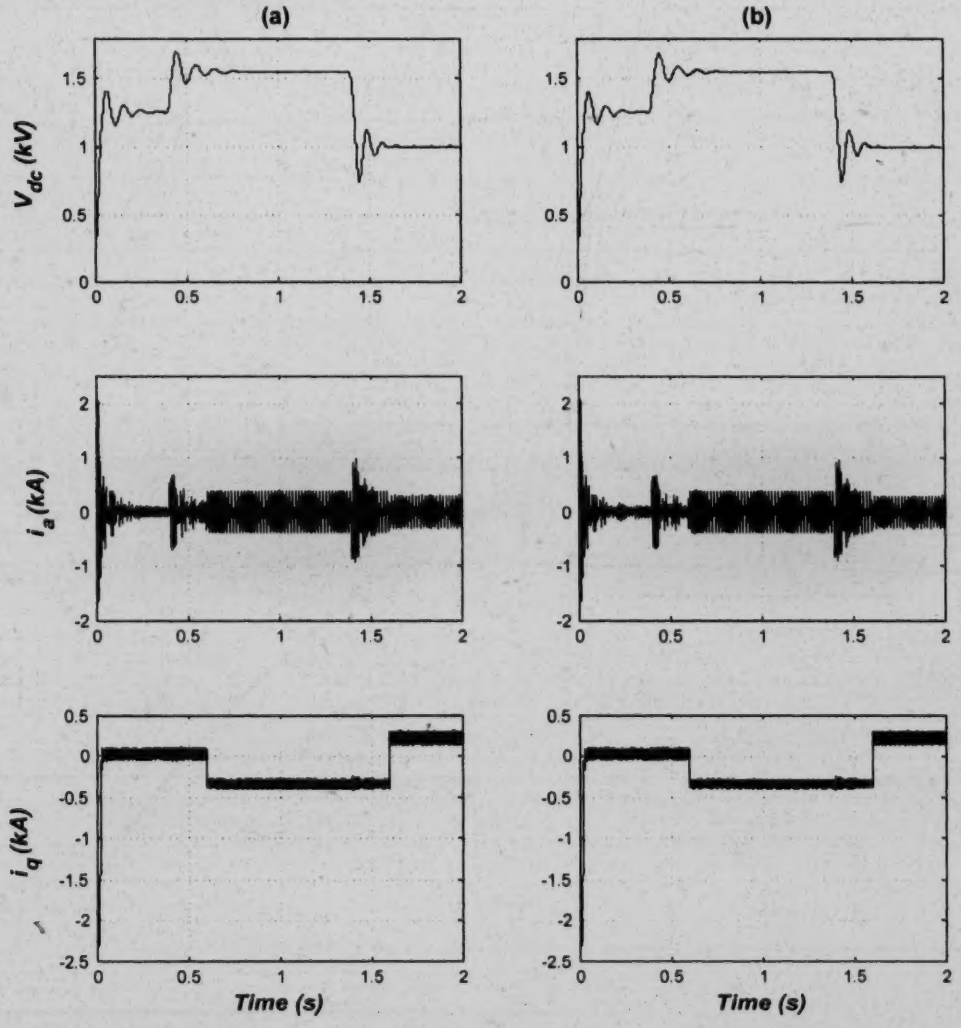

Figure 4.12: Control of grid-side converter voltage and current simulated using; (a) the ideal switch, diode and resistor model; (b) the ideal switch, capacitor and resistor model

After re-modeling the switches with the different concept, the new converter

model were validated using the capacitor voltage regulating setup from the previous section. Although the nearly identical simulation results shown in Fig. 4.12 proved the competency of the new replacement model, the complete DFIG configuration using this switch model was not producing the correct simulation results. Fig. 4.11 (c) indicated that the uninitialized starting transient of the machine at $t < 1s$ were not generated by EMTP-RV. Even the P_s and Q_s were properly controlled, the collapsing V_{dc} would still lead the simulation to instability. The controllers were repeatedly verified, and found identical to the implementations in the other two software, Appendix H Fig. H.6. Since the modeling difficulty was associated with the software itself, EMTP-RV was eliminated from any further model comparison and verification.

From the multi-stage ratification, the complete DFIG model were finalized. Out of the three off-line software simulation packages, PSCAD™/EMTDC™ and SIMULINK® proved to be the better equipped and more stable utilities for the modeling and simulation of the DFIG model created from built-in models. After finding the proper IM reference frame, selecting the robust integration method, and resolving the modeling issue bounded to the filtering inductor, the DFIG model in SIMULINK® was validated against the similar model implemented under the industrial standard PSCAD™/EMTDC™.

4.4 Real-Time DFIG Model Preparation and Model Validation

Having the detailed off-line DFIG-based WTGS model as reference, the counterpart suitable for RT simulation was ready to be developed. Due to its compatibility with RT-LAB™ models, MATLAB®/SIMULINK® V.7.0.1 was designated to be the RT model development platform. Intuitively, the two most complex electrical models required optimizations were the BBC and the WRIM. In this study, the focus was on finding the applicable optimization techniques, and discovering their feasibility.

4.4.1 Off-Line DFIG Model Complexity

Before exploring the RT model optimization techniques, the complexity of the off-line DFIG model is identified. The quantitative measures include the total simulation time of the off-line model and the dimension of the state-space (SS) solution matrix under MATLAB®/SIMULINK®.

The complete DFIG configuration presented in the previous section was repeatedly simulated for ten times. With the simulation time-step of $50\mu s$, the average time required for the $4s$ simulation was found to be $231.7422s$. This lengthy computation is the product of high order solution matrix manipulation combined with looping integration method. Using the built-in `power_analyze` function in MATLAB®, the linear system SS matrix dimensions were found and listed in Table. 4.1.

Table 4.1: Off-line DFIG Model SS Matrix Dimensions

Matrix	Dimension
A	3×3
B	3×19
C	29×3
D	29×19

The dimension of **A** implied that the state vector $\mathbf{x} \in \mathbb{R}^3$, and the three states were associated with the DC-link capacitor and the filtering L_{fg} on the balanced three-phase network. Since L_{fr} was integrated into the WRIM rotor under SIMULINK®, it did not appear as a state in the linear network SS matrix. The $\mathbb{R}^{29}$ output vector (y) along with the $\mathbb{R}^{19}$ input vector (u) has created the 29×19 **D** matrix overloading the gigahertz CPU during the simulation.

When the non-linear WRIM and controller models were also put into consideration, the total number of states jumped to 65. Although the SS matrix associated with these added states might have been relatively small, the additional computation would further slow down the already heavily loaded computational hardware.

Beside the huge number of states and high order matrixes, the Trapezoidal integration method, discussed in the previous sections, has also contributed to the demand on computational time. The four discrete Trapezoidal integration blocks in the WRIM model has created an algebraic-loop containing 48 individual model elements. The involvement at this scale would hamper the computational speed at every time-step since all the elements were held-up waiting for the integration blocks to retrieve the states from the previous time-step. Therefore, the model optimization should come in three-folds:

- reduce the size of the matrix associated with the linear electrical network;
- minimize the total number of states for the complete DFIG configuration;
- break out the algebraic-loop.

4.4.2 BBC Optimization

BBC is the most complex linear electrical component containing total of twelve power electronic switches, and each switch demands state defining input at every time-step. When the operations of the switches are collectively represented by a functional model, the individual switches can be excluded from the linear circuit. With less components, the SS matrixes will have smaller dimensions, and the complete DFIG model can be simulated more efficiently. However, the accuracy and the efficient of this switching function model shall be justified with the comparisons of simulation results.

From the efforts of many researchers [67, 75, 76], it has been proven that the modeling of the power electronics and its control units will significantly influence the accuracy of the simulation. The most sensitive subject is the timing. As the PWM based control required the determination of the switching events, the exact moment of when the switchings happened should be definitely recorded and sent to the corresponding switches. However, the discrete nature of digital simulator only allows the execution of the switchings at the beginning of each time-step; the corrupted timing information will cost the integrity of the simulation results.

In order to reduce the damage of the corrupted timing, many compensation techniques have been proposed [74, 75]. The main theme is to preserve the timing information and re-calculate the system solution in the next time-step only when the change of switch status has been detected. Then, the re-calculation would provide the corrected starting states for the system simulation in the current time-step. However, these advanced compensation techniques were not built-in to the current version of MATLAB®/SIMULINK®. Fortunately, the custom SIMULINK® toolboxes provided by OPAL-RT have included a set of time-stamped (TS) power electronic models to justify the situation.

As the name of the custom model suggested, the TS model are used to account for the switching event timings. To capture the timing information, the comparative RT-EVENTS™ blocks must be applied in the controller models, as shown in Appendix I Fig. I.1. In Chapter 3, Fig. 3.11, generation of the switching pulse was demonstrated; a comparison mechanism was utilized to determine the states of the switches. On top of the state information, the RT-EVENTS™ blocks also record when the state alteration has occurred relative to the $10ns$ resolution. With the state and timing information, the TS models can precisely apply the compensation for the switching events.

Nevertheless, the TS models have their own limitations. The 2-level 6-pulses time-stamped bridge (TSB) used to replace the SPS universal bridge is a so-called switching function model [51–57], Appendix I Fig. I.2. No individual switches are modeled; so, representation of the rectifying effect during the shut-off of all the converter switches is not possible. Instead, this technique imitates the converter ac-side with voltage sources and the dc-side with current sources, as shown in Fig. 4.13. The ac-side voltages are built from the dc voltage and gating pulses while keeping the instantaneous power equal on both sides. This technique is fast as it avoids reformulating SS equations when the converter switch status is changed.

With a $50\mu s$ time-step, the simulation results shown in Fig. 4.14 proved that the TSB is suitable for replacing the universal bridge model. During $t < 1s$, the uninitialized starting transients in P_s and Q_s were properly produced. When

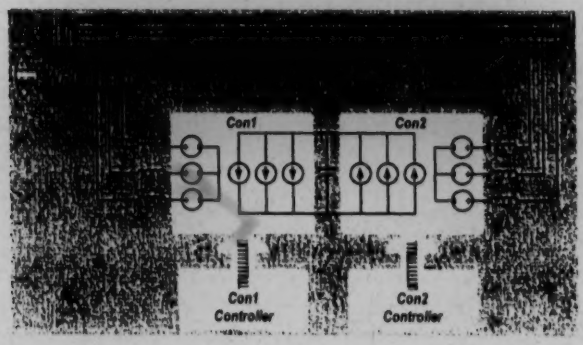

Figure 4.13: Switching function based converter model

closely inspected, the waveforms of P_s and Q_s given in Fig. 4.14 (b) appeared to be very similar to that given in Fig. 4.14 (a), which were generated using the validated DFIG model in SIMULINK®.

Table 4.2: SS Matrix Dimensions of the Optimized DFIG Configuration

Matrix	Dimension
A	2 × 2
B	2 × 13
C	19 × 2
D	19 × 13

Following the quantitative complexity measurement, the average simulation time was found reduced to 213.9203s. As expected, the dimensions of the linear electrical system SS matrixes have also been reduced, as shown in Table 4.2. Reduction of the **A** matrix was caused by the application of the custom capacitor model at the DC-link. Since the dc-side of the TSB was modeled by controlled current sources, the built-in capacitor model from MATLAB®/SIMULINK® SPS could not be used. The custom capacitor model was treated as a computational block, and it was not included in the **A** matrix. The shortened **B** matrix was obviously affected by the new TSB model. Without the actual power electronic switches, a total of 12 inputs should be eliminated. However, the six controlled voltage sources substituted at the ac-sides of the two TSB models had the number

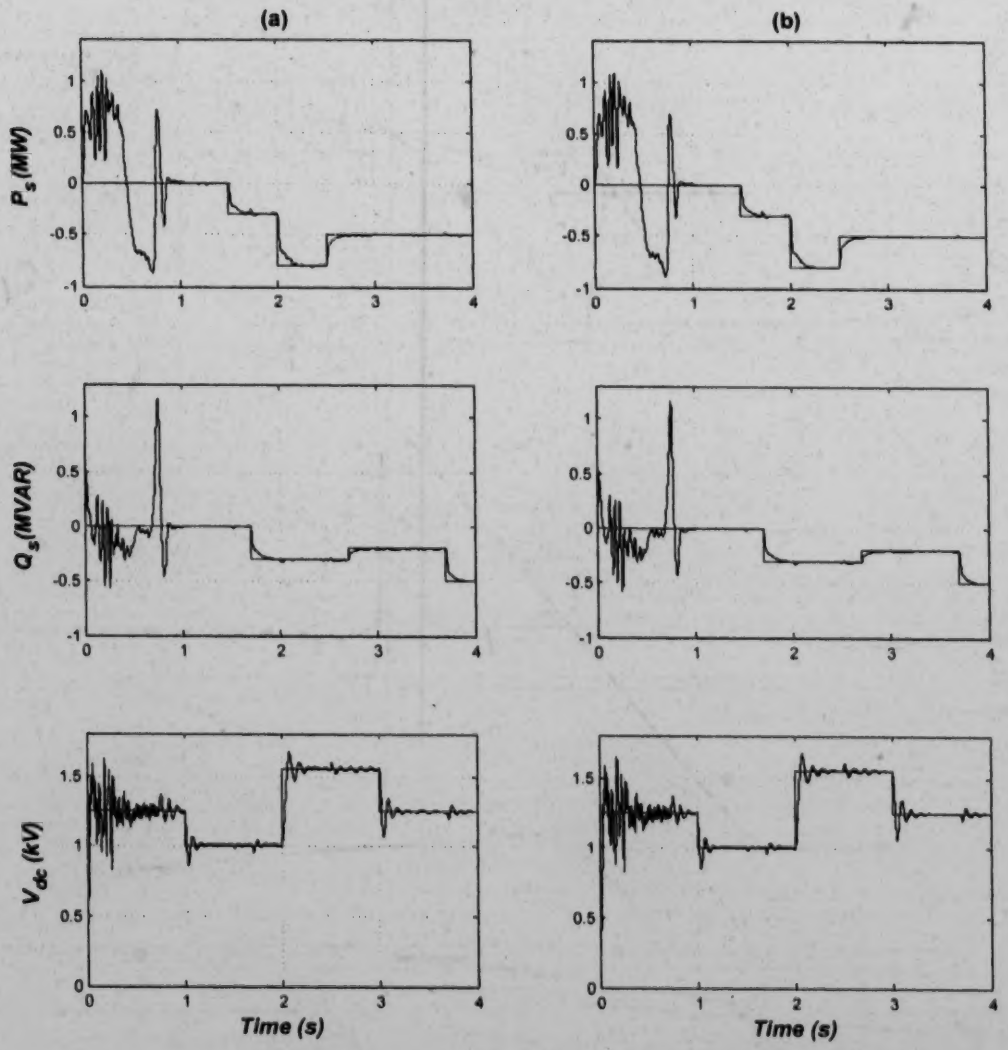

Figure 4.14: Stator-side active and reactive power, and DC-link voltage simulated with: (a) the validated detailed off-line DFIG model in SIMULINK®; (b) the DFIG model implemented with 5^{th} order IM model integrated with Trapezoidal method and TSB model

of required inputs finalized to 13. As the linear electrical model was simplified, the request on system solution was lightened. Therefore, the output vector was reduced to 19. At this point, it is clear that the TSB is acting as a stand alone computational module interacting with the linear circuit as well as the non-linear

machine model, as shown in Fig. 4.15. Finally, the total number of states of the optimized DFIG configuration was decreased to 54.

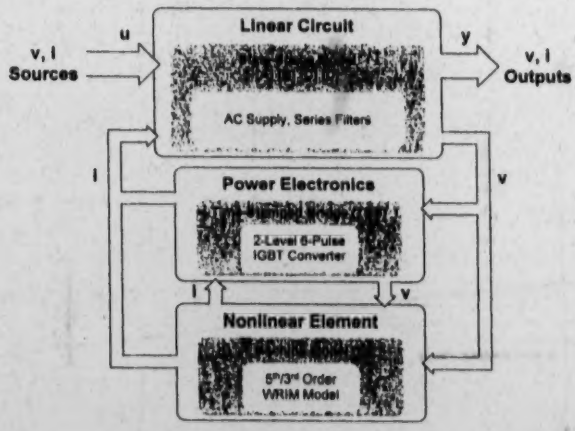

Figure 4.15: Interactions of the DFIG electrical model in SIMULINK®

4.4.3 WRIM Model Reduction

The algebraic-loop associated with the WRIM Model was obviously the most laborious process slowing down the entire simulation since the implementation of TSB has only gained marginal improvement in simulation time. As discussed before, the algebraic-loop was inherited from the application of discrete Trapezoidal integration block inside the WRIM model. Trapezoidal method's demand on the present state value would halt the computation of all the blocks within the loop. To break out the algebraic-loop, the standard way would be inserting a memory block to provide the previous state to the integration block. However, memory block will not only break the loop, but also affect the stability of the machine model. Because a memory is essentially a delay buffer, the arbitrary inclusion of a time delay will alter the system dynamic.

To compensate for the addition of a memory delay, a prediction mechanism could be employed. In discrete-time domain, the single step delay is $\frac{1}{z}$, which will create an un-compensated *pole* at the origin of the z-plane. With a prediction

function taking the form of:

$$G_{pre}(z) = 2 - \frac{1}{z} = \frac{2z-1}{z} \tag{4.4}$$

in series, the single *pole* will become a compensated double-*pole*, and the *poles* will be constrained by the *zero* created at $(0.5, 0)$. Thus, the overall transfer function for the algebraic-loop compensator is given as:

$$G_{com}(z) = \frac{2z-1}{z^2} \tag{4.5}$$

From another point of view, the prediction block improves the estimation of the current state value by calculating the average of the previous state value and the state value obtained at $t - 2\ \Delta t$.

By inserting the combination of delay and prediction function after each Trapezoidal integration block, as shown in Appendix J Fig. J.1, the average simulation time was drastically reduced to $29.3438s$ with $50\mu s$ step-size, and the algebraic-loop warning from SIMULINK® disappeared. From Fig. 4.16, the closely matching simulation results affirmed the validity of the loop breaking compensation method. Since there were no changes to the linear electrical components, the dimensions of the linear circuit SS matrixes remained the same as in Table 4.2. However, the total number of states was increased to 62 because eight memory blocks were inserted to achieve the compensated Trapezoidal integration.

The increase of the total number of states may seems against the optimization criteria. Alternately, the default Forward Euler integration method can be restored inside the WRIM model to eradicate the algebraic-loops; but, due to the limited accuracy accompanied with the Euler method, the time-step must be limited below $5\mu s$ for the study of rapidly changing high amplitude transients, i.e. matching the starting transient. Predictably, the reduction in step-size directly increased the average simulation time to $270.2500s$. Even when the total number of states was preserved, the overall efficiency of the simulation was worsened. Thus, the algebraic-loop free Trapezoidal method with a large time-step was deemed as a superior optimization solution.

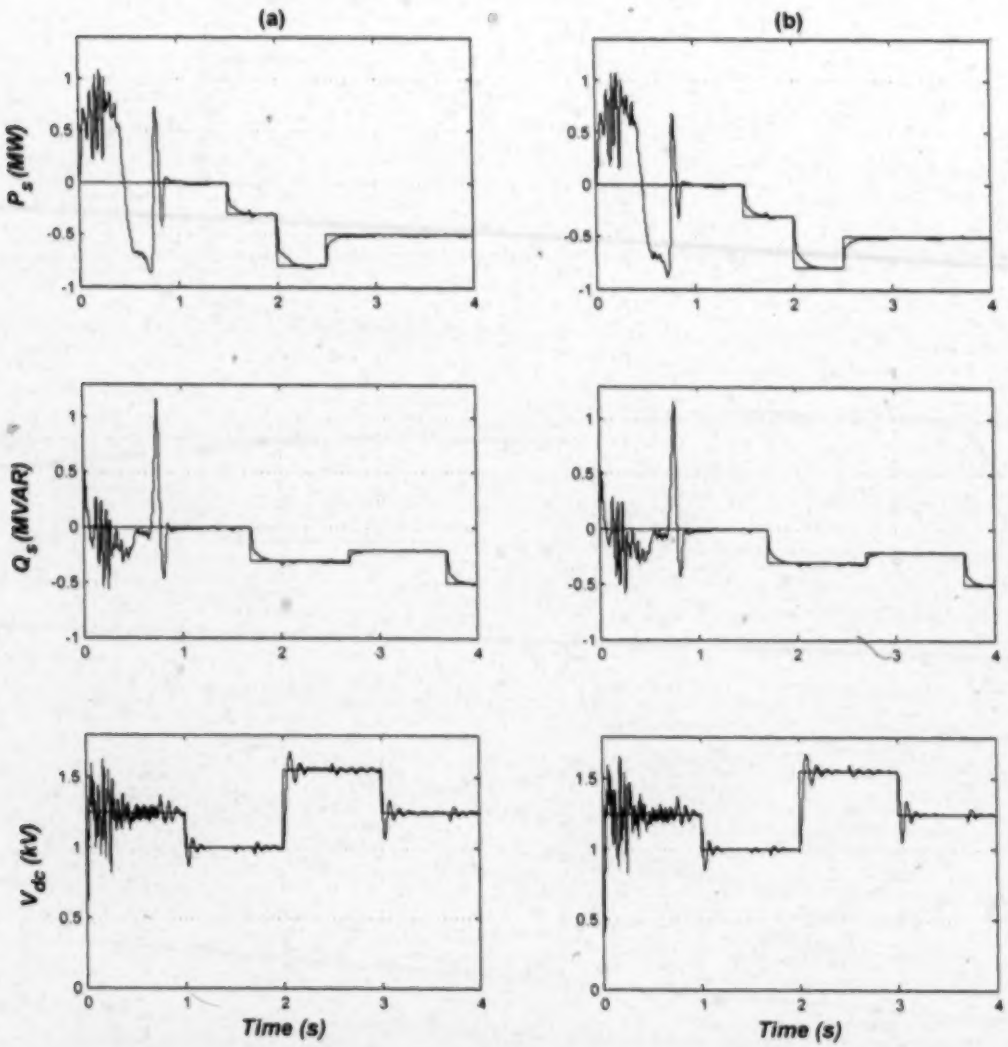

Figure 4.16: Stator-side active and reactive power, and DC-link voltage simulated with: (a) the validated detailed off-line DFIG model in SIMULINK®; (b) the DFIG model implemented with 5^{th} order IM model integrated with loop-free Trapezoidal method and TSB model

In SIMULINK®, the built-in asynchronous machine model was based on the 5^{th} order Park's model. However, several researchers have demonstrated that the 3^{rd} order model, which has the stator-side transient derivative terms removed, could provide enough accuracy while lightening the computational effort [41, 58, 59].

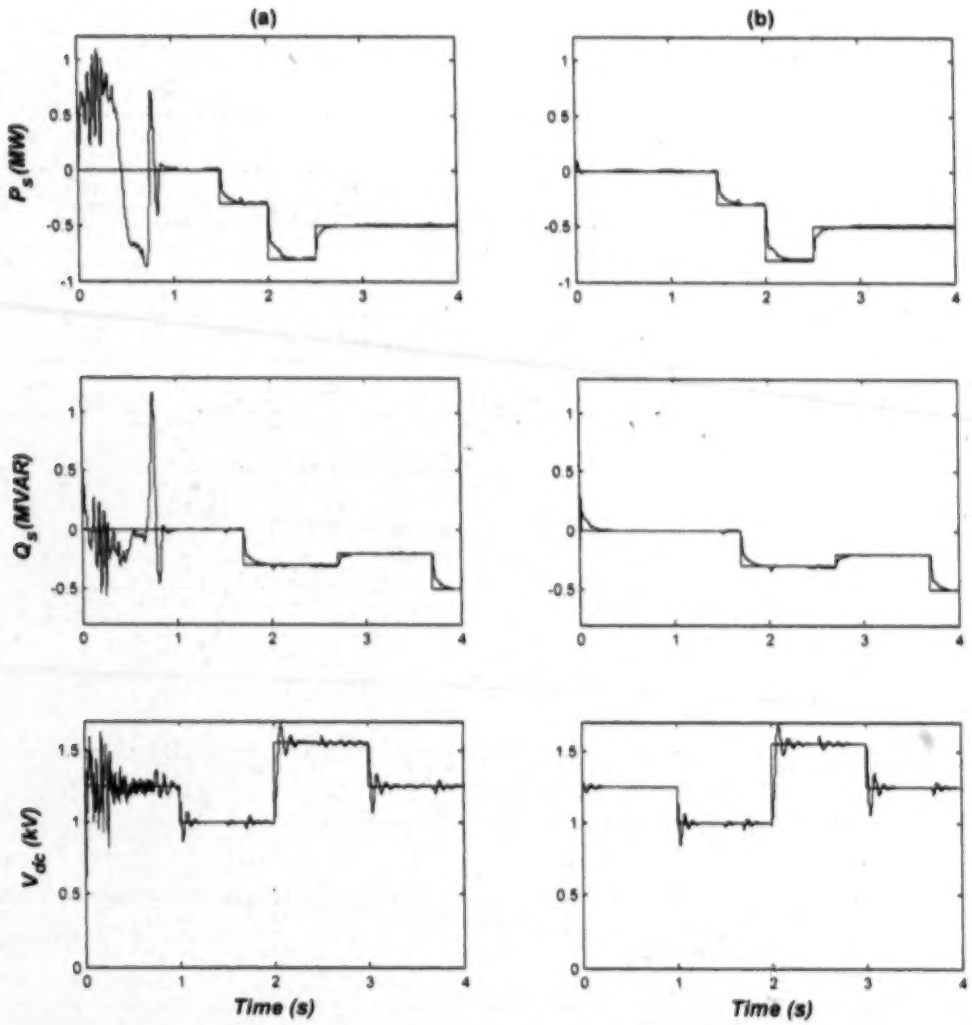

Figure 4.17: Stator-side active and reactive power, and DC-link voltage simulated with: (a) the validated detailed off-line DFIG model in SIMULINK®; (b) 3^{rd} order IM model integrated with loop-free Trapezoidal method and TSB

The enactment of the altered stator-side equations in the qd frame are given in Appendix K Fig. K.1.

Comparisons of the simulation results presented in Fig. 4.17 revealed that the removal of the stator-side transient has resulted in the omission of the WRIM starting transients. Nevertheless, the controlled steady-state and transient

responses were accurately preserved. It was also found that the slow transient of the DFIG could be simulated with larger time step when loop-free Trapezoidal method and TSB were applied. By increasing the time-step to $100\mu s$, the average simulation time has been further lowered to $14.6250s$. Since the linear electrical system was not altered, the improvement was attributed to the reduction of the total number of states by 2.

4.4.4 Implementation of the Lumped-Mass Mechanical Model

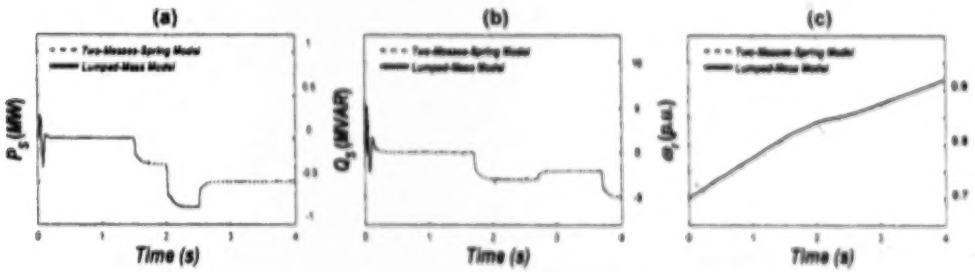

Figure 4.18: : Comparing the difference between two-masses-spring and lump-mass model with the simulation results of: (a) stator-side active power in SIMULINK®; (b) stator-side reactive power; (c) rotor speed

To further speed-up the simulation, the lumped-mass mechanical model discussed in Chapter 2 was implemented along with the 3^{rd} order WRIM and the TSB models. In Fig. 4.18 (a) and 4.18 (b), the simulation results obtained for P_s and Q_s has proved that the decoupling effect created by the operations of the BBC could shield the electrical grid from mechanical oscillations at the rotor shaft. The slowly varying electrical waveforms looked essentially the same with the implementation of either mechanical model. However, the lumped-mass model could not reproduce the oscillatory shaft vibrations, and only the general trend of the ω_r was found, Fig. 4.18 (c).

After repetitive simulations and comparisons, it was verified that the simplified mechanical model will mitigate the average simulation time by 1 to $3s$. Although no alterations will be made in the linear electrical matrices, the lower order mechanical model will reduce the total number of states by 4.

4.4.5 Real-Time Simulation Model Validation

As the optimized off-line model was running reasonably fast and accurate, a decision was made to move on to the exploration of RT simulation of the complete DFIG configuration. Since the optimized DFIG configuration already fulfilled the zero algebraic-loop modeling criteria, the entire model only needed to be contained in a subsystem with the prefix of 'SM_' for it to go through a sequence of RT simulation procedures.

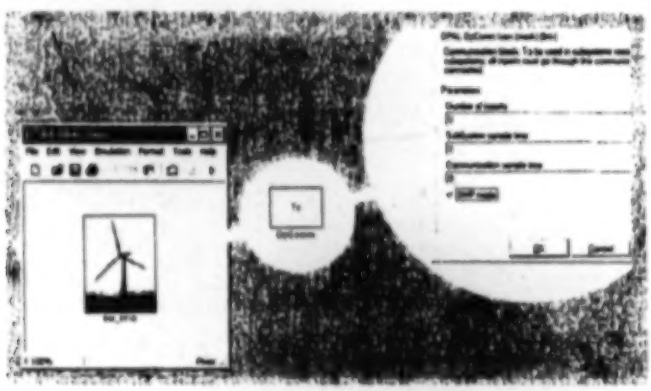

Figure 4.19: : Including the OpComm block to activate the XHP mode for real-time simulation

Before compiling the SIMULINK® model into C-code, the proprietary OpComm block from OPAL-RT is added into the subsystem, Fig. 4.19. By enabling the XHP (eXtremely-High-Performance) mode, one of the two CPUs in the specific RT simulator *node* will be dedicated for solving the DFIG model. The dedicated GHz CPU will only perform arithmetic computations and maintain critical communication to the shared memory. RT Linux® OS will be loaded onto the second CPU to manage data feeding to the shared memory and to interact with the peripheral hardware.

All the possible combinations of the proposed optimization techniques were investigated. Their effect on the real-time and off-line simulation time were conclusively listed in Table 4.3, where FE, Tra., and CTra. represented Forward Euler, Trapezoidal, and compensated loop-free Trapezoidal, respectively. By

Table 4.3: Conclusive Overview of the RT and Off-line Simulation Results with Various Optimization Options (FE: Forward Euler; Tra.: Trapezoidal; CTra.: Compensated Trapezoidal)

Setup	WRIM Model		BBC Model	Mech. Model	$T_s(\mu s)$	$T_{avg}(s)$	$T_{RT}(\mu s)$
	order	method					
1	3^{rd}	FE	TSB	Lumped	100	11.4063	5.615000
2	3^{rd}	FE	TSB	MMs	100	12.9375	5.715000
3	3^{rd}	FE	SPS	Lumped	–	–	–
4	3^{rd}	FE	SPS	MMs	–	–	–
5	3^{rd}	Tra.	TSB	Lumped	100	50.7031	–
6	3^{rd}	Tra.	TSB	MMs	100	52.4063	–
7	3^{rd}	Tra.	SPS	Lumped	50	101.3500	–
8	3^{rd}	Tra.	SPS	MMs	50	103.6406	–
9	3^{rd}	CTra.	TSB	Lumped	100	14.6250	5.867333
10	3^{rd}	CTra.	TSB	MMs	100	15.5938	5.980000
11	3^{rd}	CTra.	SPS	Lumped	–	–	–
12	3^{rd}	CTra.	SPS	MMs	–	–	–
13	5^{th}	FE	TSB	Lumped	5	267.8594	5.220000
14	5^{th}	FE	TSB	MMs	5	270.2500	5.295000
15	5^{th}	FE	SPS	Lumped	–	–	–
16	5^{th}	FE	SPS	MMs	–	–	–
17	5^{th}	Tra.	TSB	Lumped	50	210.6937	–
18	5^{th}	Tra.	TSB	MMs	50	213.0203	–
19	5^{th}	Tra.	SPS	Lumped	50	229.7609	–
20	5^{th}	Tra.	SPS	MMs	50	231.7422	–
21	5^{th}	CTra.	TSB	Lumped	50	27.2969	5.475000
22	5^{th}	CTra.	TSB	MMs	50	29.3438	5.537333
23	5^{th}	CTra.	SPS	Lumped	–	–	–
24	5^{th}	CTra.	SPS	MMs	–	–	–

comparing the optimal step-size (T_s), average off-line simulation time (T_{avg}), and maximum RT execution time (T_{RT}), the robustness and efficiency of each optimization technique are indirectly evaluated.

By inspecting the sixth column of Table 4.3, the results of T_s revealed that Trapezoidal integration method was the most robust integration method among the three. Using Trapezoidal method, the 3^{rd} and 5^{th} order WRIM model could be coupled with any of the two BBC models to produce proper simulation results. Next, the superiority of the loop-free Trapezoidal method over the Forward Euler

method is confirmed by comparing the T_s for Setup 13 and 21. With Forward Euler, the simulation time-step must be substantially reduced for the WRIM model to generate accurate results.

Since the loop-free Trapezoidal and Forward Euler method were less robust, the WRIM model implemented with these two methods could only be adhered to the more accurate TSB model. While the TSB model has been successfully combined with all the different WRIM models, the SPS universal bridge model only worked properly with the most accurate 5^{th} order WRIM model implemented with Trapezoidal integration method.

The reason for investigating the 3^{rd} order WRIM model became clearer when the T_s used for the simulation of Setup 1, 2, 5, 6, 9, and 10 was found. The possible use of larger T_s was directly benefitted by the reduction in modeling detail. Since the 3^{rd} order machine model was not able to simulate the uninitialized high frequency oscillations in the power waveforms, the time-step can be increased for the simulation of the slowly varying steady-states. Accuracy of a model is relative to the study. If the study only involves slow transients and non-oscillatory responses, application of the 3^{rd} order machine model will not only provide accurate results, but also help reducing overall simulation time.

Depending on the results for T_{avg}, the most appropriate configuration for off-line simulation was found to be Setup 1. This configuration has benefitted from the inclusion of the reduced order WRIM model, Forward Euler integration method, efficient TSB, simplest mechanical model, and larger time-step. Because the stator-side transient is eliminated in the 3^{rd} order machine model, the WRIM model involving less integration equations can be solved much faster with larger step-size. Implementing the WRIM model with either the Forward Euler or loop-free Trapezoidal method, the algebraic-loop problem can be bypassed, and the simulation time can be significantly reduced. Further analysis on the T_{avg} for Setup 1, 5, and 9 has unveiled that the least robust Forward Euler method required the least amount of solution time. When compared the T_{avg} results for Setup 18 and 20, the advantage of using TSB becomes more obvious. For off-line simulation,

the time saved by switching to the simplest lumped mass mechanical model may seem marginal. However, this saving will become more critical when multiple DFIG systems are simulated at the same time.

In Table 4.3, the results listed under T_{RT} have revealed the suitable configurations for RT simulation and their maximum RT computation time. First of all, the configuration must be free of algebraic-loop. That was why Setups 5-8 and 17-20 can only be simulated in off-line mode. Selection of the BBC model is, however, predetermine by the stability issue discussed above. Therefore, the TSB model must be used to construct the BBC for RT simulation. The orders of the machine and mechanical model do not have direct influence on the creation of a valid RT configuration; nevertheless, they do affect the computational time, and the outcomes are very interesting. Looking at the T_{RT} for Setup 9-10 and 21-22, it was found that the higher order WRIM model was actually providing better dynamic in RT simulation. Although this was an interesting discovery, the topic was out of the scope of this study.

After successful compilation, the model can be simulated in the RT simulator. But, this does not automatically qualify the simulation as running in RT. To be qualified as RT simulation, all the processes related to solving the complete model must be finished within the given time-step. The results for Setup 13 and 14 were included as examples of un-qualified RT simulation since their T_{RT} have exceeded the corresponding T_s. For the six Setups (1, 2, 9, 10, 21, and 22) that can be simulated in RT, the time distribution within a fixed time-step is presented in Table 4.4.

The distribution of a single time-step has clearly shown that computation was the main task taking up most of the processing time. On top of computation, other processes, such as communication, also occupied a small portion of the given time-step. Idle time is the best indicator for successful RT simulation. As long as all the processes are fitted into the fixed time-step, the idle will be positive. The large idle time indicates that the single DFIG configuration has only taken up a small portion of the available capacity from the simulator, and more complexity can be packed

Table 4.4: Execution times for individual tasks within one time-step for various setups

Time Distribution (μs)	Setup 1	Setup 2	Setup 9	Setup 10	Setup 21	Setup 22
Computation Time	5.615	5.715	5.867	5.980	5.475	5.537
Idle Time	91.758	92.182	91.75	91.637	42.242	42.085
Data Acquisition	1.302	0.94	1.068	1.040	1.065	1.048
Status Update	0.307	0.195	0.295	0.305	0.302	0.265
Target Request Time	0.040	0.047	0.040	0.070	0.062	0.082
Host Request Time	0.035	0.038	0.032	0.038	0.042	0.037
Synchronization	0.035	0.035	0.045	0.035	0.035	0.052
Others	0.882	0.938	0.773	0.982	0.780	0.822
Total Step-Size	100.000	100.000	100.000	100.000	50.000	50.000

into the system model.

To prove the authenticity of the simulator, the RT simulation results were recorded onto an oscilloscope through the digital interface. In Fig. 4.20 and 4.21, the RT simulation results for Setup 21 and 22 are presented next to their associated SIMULINK® off-line simulation results, respectively. Comparisons of the waveforms clearly ascertain the accuracy of the RT simulator.

The waveforms for Setup 21 and 22 have also uncovered an issue related to the mechanical model for the DFIG configuration. When using the lumped-mass model, the starting oscillations in the power waveforms were exaggerated. The main cause of this phenomenon was associated to the lack of damping elements in the lumped-mass model. Also, the under-damped model will prolong the propagation of the mechanical vibrations. Therefore, the lower order mechanical model should be used with care. All in all, the un-initialized starting of the DFIG is only a special case for model validation. In real-world operation, the generating unit should be properly initialized to eliminate the violent electrical and mechanical oscillations.

Because of its efficiency and accuracy, the most detailed configuration, Setup 22, should always be used for both off-line and real-time simulations. This recommendation is based on the results given in Table 4.3. Instead of lowering the computation time, the incorporation of the reduced order WRIM model has

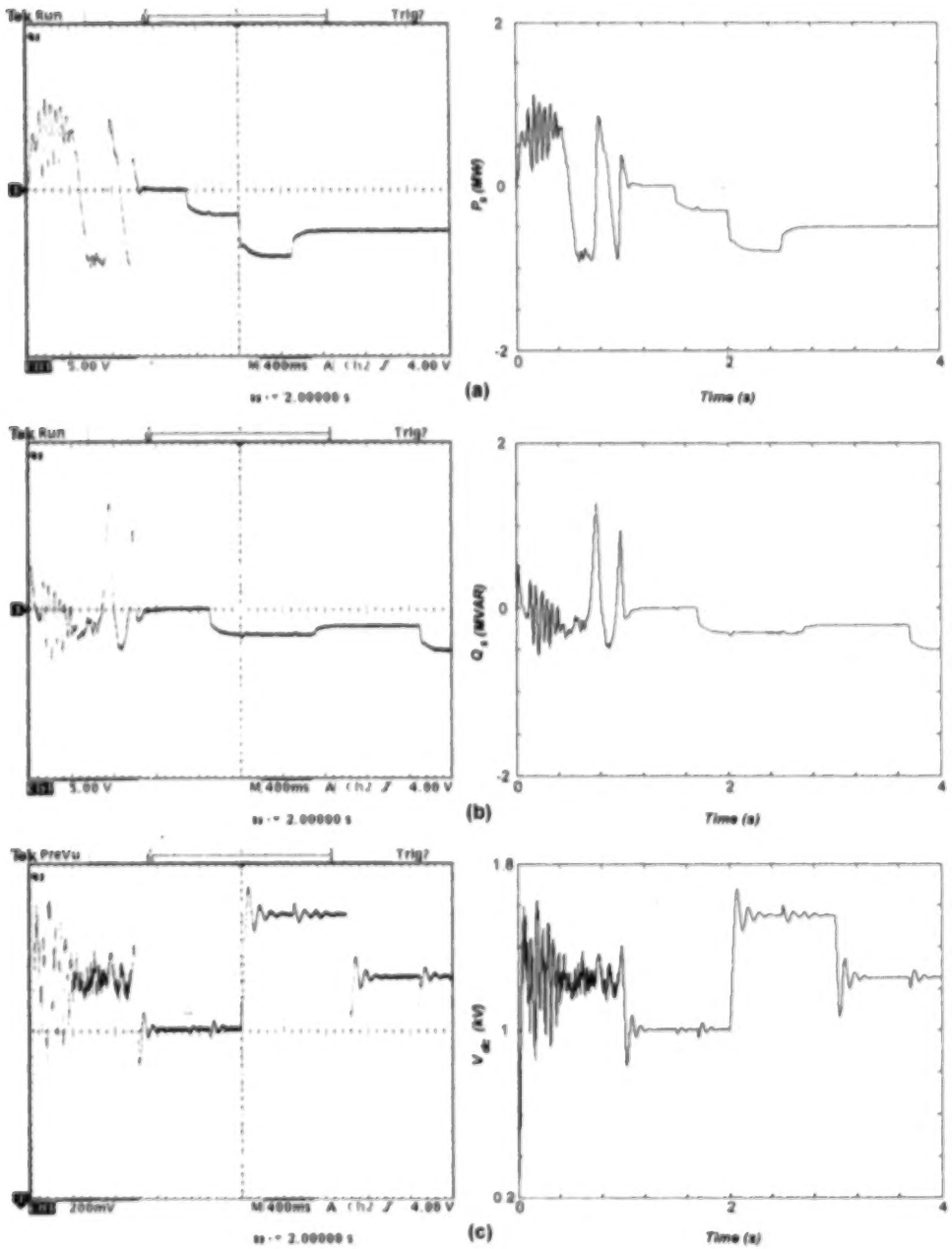

Figure 4.20: : Real-time and off-line simulation results for Setup 21: (a) stator-side active power; (b) stator-side reactive power; (c) DC-line voltage

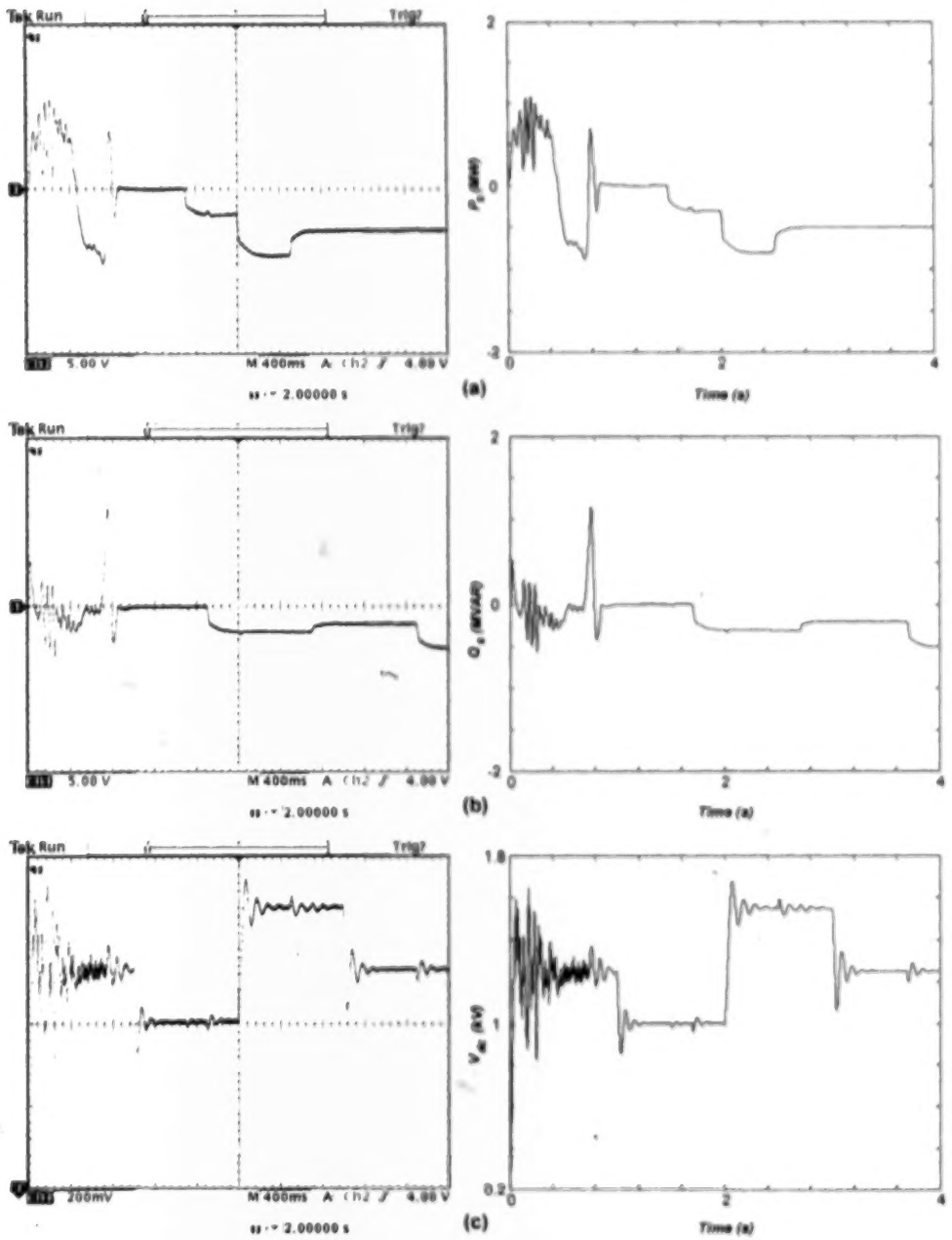

Figure 4.21: : Real-time and off-line simulation results for Setup 22: (a) stator-side active power; (b) stator-side reactive power; (c) DC-line voltage

hampered the entire system's dynamic in RT. With the trade off of accuracy, the application of a lumped-mass mechanical model has saved less than $3s$ and $0.1\mu s$ during off-line and real-time simulations, respectively. All these facts encourage the use of Setup 22 for the study of the complete DFIG configuration.

4.5 Summary

In this chapter, the complete DFIG configuration and its controllers developed in Chapter 2 and 3 was verified and validated through the off-line simulations in PSCAD™/EMTDC™, MATLAB®/SIMULINK®, and EMTP-RV. After sequence of model simplification, different configurations suitable for real-time simulation were proposed. Through the exhaustive analysis and comparison, the most feasible configuration (Setup 22) consisted of the WRIM model implemented with the compensated loop-free Trapezoidal method and the BBC modeled with TSB was recommended for the further studies of the complete DFIG-based WTGS in both off-line and real-time simulations.

5

Wind Farm Dynamics and Aggregation

5.1 Introduction

To effectively supplement the vast electrical network, wind farms are formed of numerous WTGSs for greater generation capacity. The collective capacity of modern GW wind farm is capable of satisfying the needs from thousands of households. In order to study the effect of wind farms on the grid, an appropriate representation for the network connected wind farms is needed. However, a wind farm model consisting of multiple highly complicated WTGS and detailed transmission systems is difficult to setup, and the demand on computational power can easily overwhelm the modern simulators. To resolve this problem, lower order aggregated wind farm models which represent the collective behavior of all the WTGSs at the collection bus were developed.

The behavior of the grid-connected wind energy facilities generally unfamiliar to the mass majority. Therefore, this chapter starts with the simulation of a single grid-connected WTGS. Through the smaller scale study, the variable wind speed and fault interactions of the modern WTGS are clearly demonstrated. After building the necessary knowledge and tools through the illustrative studies, a

wind farm consisting of ten WTGSs is modeled for real-time simulation and aggregation analysis.

5.2 Background

For a very long time, WTGSs are modeled as a simple negative load in power system simulation study. The main reason was that the low capacity fixed-speed WTGSs could not participate in reactive power regulation, and disturbances in the collection system could easily knock this kind of WTGS off-line [3]. However, the emergence of variable-speed WTGSs has promoted the change in modeling and simulation practice. The advancements in design and control allowed the variable-speed WTGSs to participate in reactive power regulation, and have better fault ride-through capabilities. Studies [3,77] have shown that integration of the newer wind facilities has increased the electric network stability.

Authorities have also recognized the growing capacity of wind generation and the progression in the related technologies [2,6,26]. In the upcoming standardized operation codes, the wind farm is required to support the grid and achieve certain levels of disturbance ride through capability. This creates the need for a efficient wind farm model to assist operators to accurately assess the wind farm operation and make the correct decisions in real-time.

5.3 Single WTGS Dynamics

The online performance of a stand-alone WTGS can be easily projected for the understanding of wind farm operations. In this section, the interaction of a DFIG-based WTGS to variable wind source and grid faults are investigated using the schematic shown in Fig. 5.1. Constructed from the detailed DFIG configuration, Setup 22, presented in Chapter 4, the WTGS was connected to the $25kV$ infinite bus B1 through the distribution transformer and two sections of identical three-phase transmission lines represented with the conventional distributed line model.

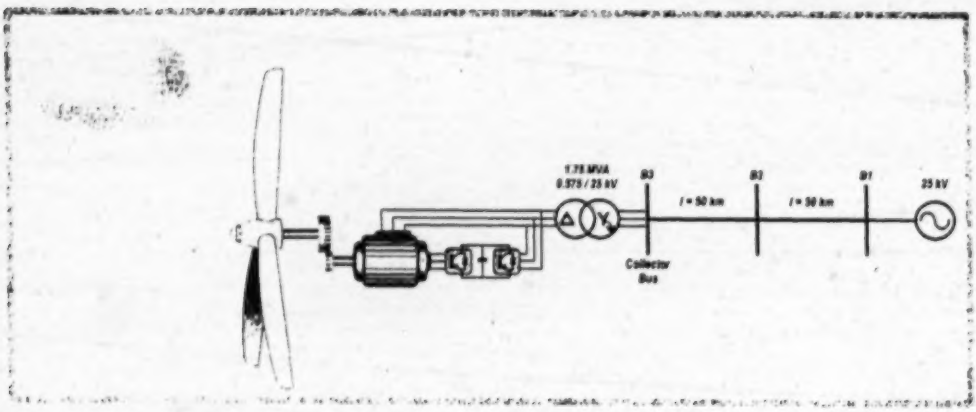

Figure 5.1: Single grid-connected DFIG-based WTGS

5.3.1 Interaction of the Stand-Alone WTGS with Variable Wind Speed

The coordination between the mechanical and electrical controllers is verified by exserting variable wind speed to the grid-connected WTGS shown in Fig. 5.1. For the $40s$ off-line simulation in SIMULINK®, the initial turbine speed was set to $0.7pu$, and initial power generation from the WRIM was set to zero. To achieve reasonable resolution, the simulation time-step was fixed to $50\mu s$.

By convention [18, 26, 43], the variable wind source (ν_w) was made up of four components: average speed, gust, ramp, and turbulence (Fig. 5.2). As shown in Fig. 5.3 (a), average wind speed for the case study was set to $11.3m/s$. Starting at $t = 0s$, the parabolic gust was given the amplitude of $3.0m/s$ and period of $33.3s$. With the amplitude of $10m/s$ and the slope of $0.5m/s^2$, the ramping component was started at $t = 20s$. Finally, the turbulence was generated as bandlimited white-noise with variance of $1.2m/s$. Although the generation of the turbulence can be made more non-stationary [29, 41], the simulation results proved that would be unnecessary for the DFIG-based WTGS.

In Fig. 5.3 (b), the smooth ω_T indicated that the turbine was working as a low-pass filter screening out the effects of the high frequency turbulence in ν_w. By

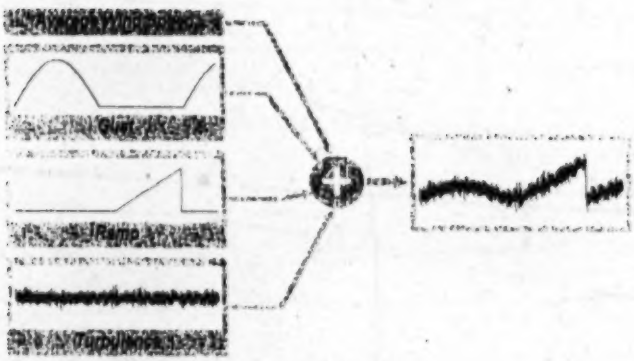

Figure 5.2: Synthesis of the variable wind speed

comparing the waveforms shown in Fig. 5.3 (a) and Fig. 5.3 (b), it was easy to notice the $5s$ lag between the variations in ν_w and ω_T. As discussed in Chapter 3, this delay was designed into the mechanical controller to prevent the massive spinning turbine from wearing the mechanical components during the abrupt response to the ever changing wind.

As shown in Fig. 5.3 (b) and (c), before reaching the speed limit of $1.2pu$, ω_T was directly regulated by altering the active power generation (P_{elec}). Maintaining the proper coordination between ω_T and P_{elec} is critical for the WTGS control. If too much power were extracted, the turbine speed would be pushed out of the optimal generation region. On the other hand, insufficient harvesting of the available power would allow the turbine to accelerate to the hazardous speed range. When ω_T reached its limit at $t = 30s$, active power generation was significantly increased to diffuse the load on the turbine and the mechanical components.

As soon as the generator reached its capacity at $t = 31.8s$, the pitch control was activated, Fig. 5.3 (e), in order to lessen the amount of power being extracted from the wind. When the ceasing ramp caused a huge dip in the available wind power at $t = 32.9s$, the mechanical controller quickly responded by resetting θ_{pitch} to zero to increase power collection from the turbine, and ordered the electrical controller to reduce P_{elec} to prevent ω_T from collapsing. The simulation results in Fig. 5.3 demonstrated that the existing controllers can effectivly coordinate

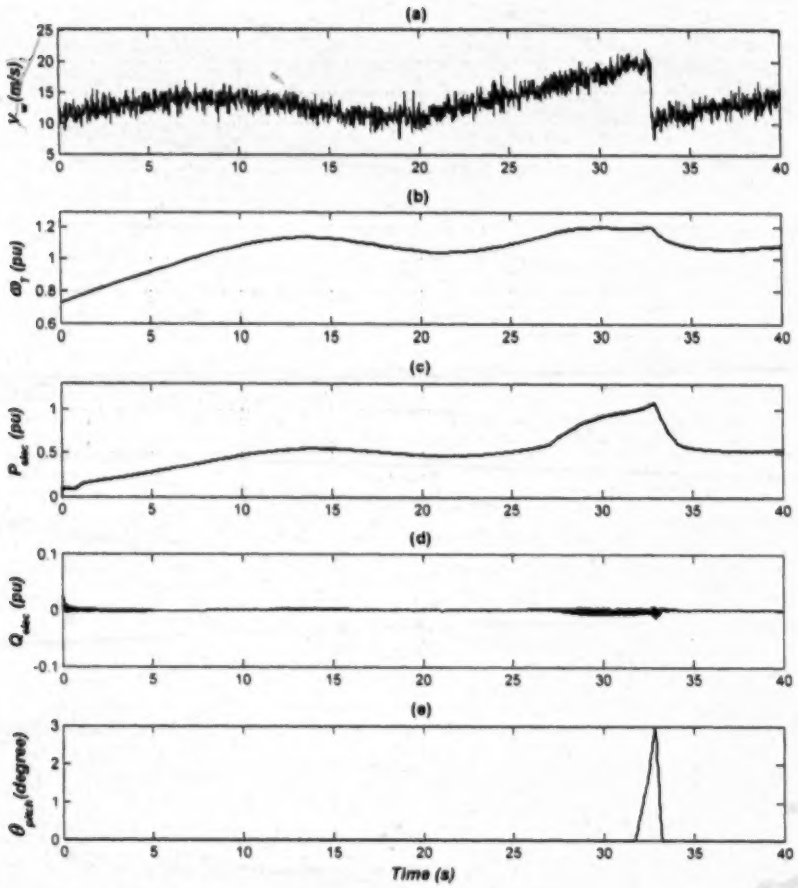

Figure 5.3: Response of the single DFIG-based WTGS to variable wind speed: (a) variable wind signal; (b) turbine rotational speed; (c) generated active power; (d) generated reactive power; (e) turbine blade pitch angle

the mechanical and electrical parameters to stabilize the WTGS to withstand the disruptive variations, and prepared the entire system for the next rising wave in ν_w. In spite of the variations in other system parameters, the sophisticated vector control has kept the generated reactive power (Q_{elec}) close to zero throughout the entire simulation, Fig. 5.3 (d).

Through the wind speed interaction study, the complete mechanical and electrical controller design was verified. To allow maximum unity power

generation, turbine speed was continuously adjusted. When the system components reached their limits, proper control sequence was engaged to sustain the stability.

5.3.2 Interaction of the Stand-Alone WTGS with Grid faults

Referring to the WECC low voltage ride-through standard presented at the California Energy Commission hearing, wind plant will be required to ride through a "normally cleared single-line-to-ground or three-phase fault on a transmission line connected to the plant switchyard or substation" [2]. Therefore, three case studies were setup to examine the reactions of DFIG-based WTGS to disturbances in the transmission system. For better compliance with the standard from WECC, the first two studies were specifically designed to investigate the influence of the most common single-line-to-ground and three-phase fault on a grid-connected WTGS for a period of $0.15s$. Although the two-phase-to-ground fault is rare [79], the study is included to provide more information on the control, protection, and operation of a WTGS under hazardous conditions.

In the off-line simulator SIMULINK®, the study cases were evenly distributed along a $40s$ time line and simulated with $50\mu s$ resolution. This collective examination provides a comparative overview on the impacts generated by various fault situations on different system parameters. Since the focus of this simulation was to study the fault response of the given WTGS, the wind speed was kept constant at $11.3m/s$, and no extra protective devices were implemented. To allow fast convergence towards the steady-state, the WTGS was initialized to have the turbine rotation speed $(\omega_T) = 0.96pu$, generated active power $(P_{elec}) = 0.46pu$, generated reactive $(Q_{elec}) = 0.0pu$, and BBC dc-link voltage $(V_{dc}) = 1250V$.

5.3.2.1 Case 1: Single-line-to-ground fault

When the system reached its steady-state at $t = 10s$, a $9cycle/0.15s$ single-phase-to-ground fault was created in the middle of the transmission system. As shown in Fig. 5.4 (a) and (c), the phase-a voltage at bus B2 and B3 were immediately

dropped to zero. At the distribution transformer low-voltage side, the loss of phase-*a* voltage caused disruptive ripples in $|V_s|$ (Fig. 5.5 (a) and 5.6 (a)) which was the magnitude of the WTGS supporting voltage. From the ripples recorded in the waveform of V_{dc}, Fig. 5.5 (e) and 5.6 (d), it was realized that the oscillation in $|V_s|$ has been propagating through the electrical components during the fault.

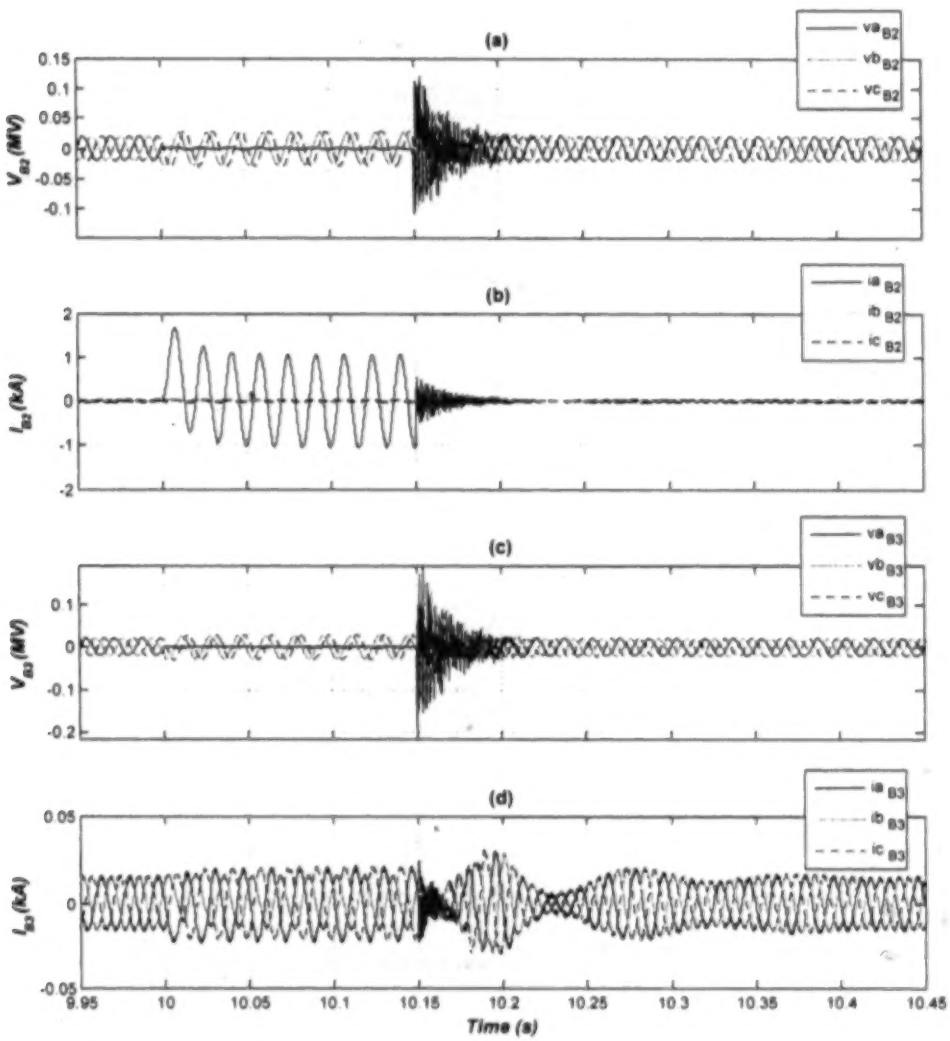

Figure 5.4: Three-phase voltage and current waveforms at bus B2 and B3 during the single-phase-to-ground fault

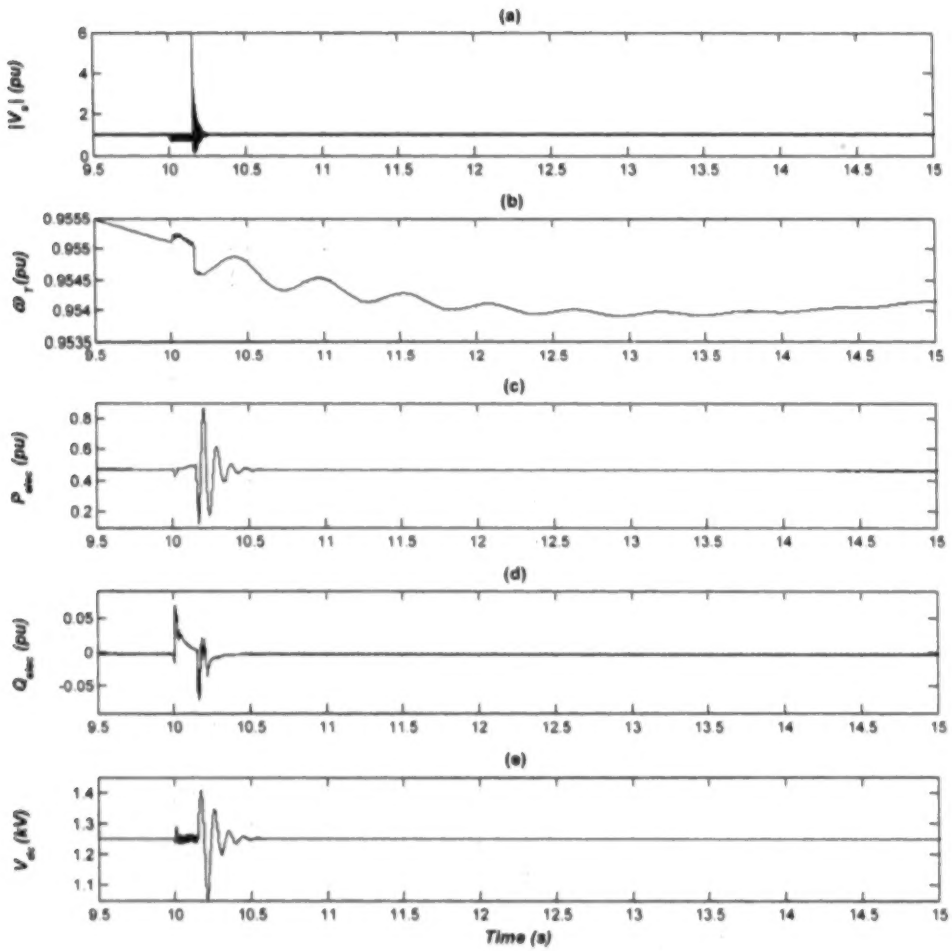

Figure 5.5: Impacts of the single-line-to-ground fault on the WTGS internal parameters: (a) magnitude of the supporting voltage; (b) turbine rotational speed; (c) generated active power; (d) generated reactive power; (e) DC-link voltage

With phase-*a* grounding through a small impedance at bus B2, a huge unbalanced current was drawn to ground, Fig. 5.4 (b), distorting the balance along the line. Fig. 5.4 (d) shows that the single-phase-to-ground current has caused the swelling in phase *a* and *c* current at bus B3.

Under the given fault conditions, the controller was able to maintain the WGTS online. Only a small dip in P_{elec} and Q_{elec} were observed in Fig. 5.6 (b) and

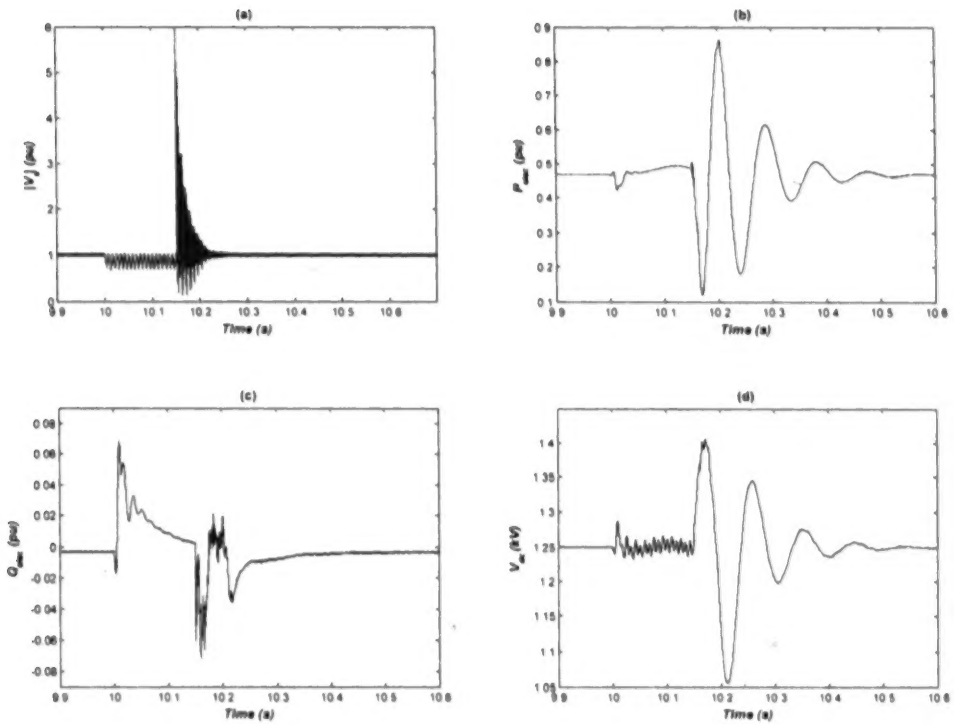

Figure 5.6: Zoom-in view of Fig. 5.5: (a) magnitude of the supporting voltage; (b) generated active power; (c) generated reactive power; (d) DC-link voltage

(c), respectively, at the beginning of the fault. This temporary capacity loss was caused by the sudden reduction in average $|V_s|$. As active power generation fell while the mechanical power captured from the wind stayed constant, the turbine accelerated (Fig. 5.5 (b)) resulting in the increase in reactive power generation. However, the fast acting controller resumed P_{elec} to its pre-fault level within $0.02s$. In order to sustain balance between the mechanical and electrical torque, active power generation was increased to slow down the turbine. Reduction in ω_T was then directly mirrored in the falling of Q_{elec} from $t = 10.02s$ to $t = 10.15s$.

When the fault was normally cleared at $t = 10.15s$, huge in-rush current from the sudden engagement of phase-a has created high frequency oscillations in all three phases, as shown in the voltage and current waveforms in Fig. 5.4. With

relatively low damping in the $50km$ line, the oscillations lasted for approximately $0.075s$. At the end of the oscillation, $|V_s|$ was stabilized to its pre-fault value.

From the post-fault response shown in Fig. 5.5 (a), (c), and (e), the grid-side converter controller was found sensitive to the changes in $|V_s|$. When the fault was cleared, huge in-rush current caused high amplitude jump in $|V_s|$ with the duration less than $0.001s$. However, the controller was sensitive enough to pick up the variation and tried to reset the DC-link voltage. Because the variation in V_s was very abrupt, the controller perceived that as a command for step-change in V_{dc}. This was why the signature under-damped response appeared in V_{dc} after the fault, and propagated through the line causing variations in P_{elec}.

By restoring $|V_s|$, a new set-point was reached for ω_T. This abrupt shift in turbine speed has caused minor disturbance in Q_{elec}. Since the speed variation was small (0.02%), Q_{elec} was quickly driven back to its optimal value for unit power generation. With the given shaft stiffness, the multi-mass mechanical system settled to its steady-state in $5s$.

5.3.2.2 Case 2: Three-phase-to-ground fault

After all the transient from the previous fault study has completely settled, a $9cycle/0.15s$ three-phase-to-ground fault was triggered at $t = 20s$. As shown in Fig. 5.7 (a), the voltages at the grounded bus B2 were reduced to zero. However, Fig. 5.7 (c) showed that the voltage at bus B3 was only lowered to a minimum point and then gradually increased. By inspecting the waveform of $|V_s|$ in Fig. 5.8 (a) and 5.9 (a), it was found that the voltage took $0.02s$ diving to its lowest point at $0.0268pu$ and slowly increased to $\approx 0.3pu$.

Since the line section between bus B2 and B3 was cut off from the ideal source, the only voltage support was from WTGS. Because the electrical controller lost its frequency reference, the grid supporting voltage was generated at an arbitrary reference frame with very high frequency. This loss in synchronism has also affected the current through bus B3. Fig. 5.7 (d) shows that the three-phase currents were derailed from the normal abc frame. Down the line to bus B2, the

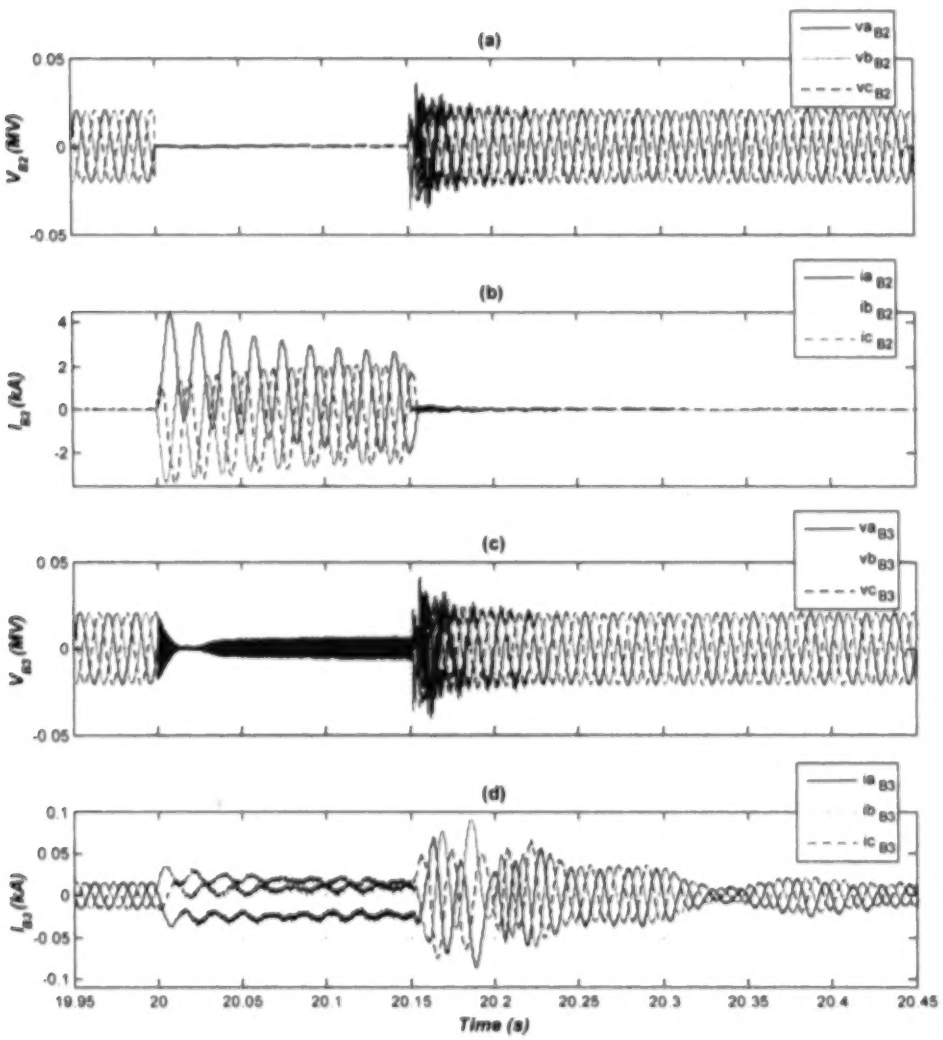

Figure 5.7: Three-phase voltage and current waveforms at bus B2 and B3 during the three-phase-to-ground fault

currents were increased because of the near zero grounding resistance. However, the balanced common ground has converged the current back into the ordinary three-phase reference frame at the grounded bus B2 (Fig. 5.7 (b)).

At the instant $|V_s|$ reached its lowest point, Fig. 5.8 (c) and (d) show that P_{elec}

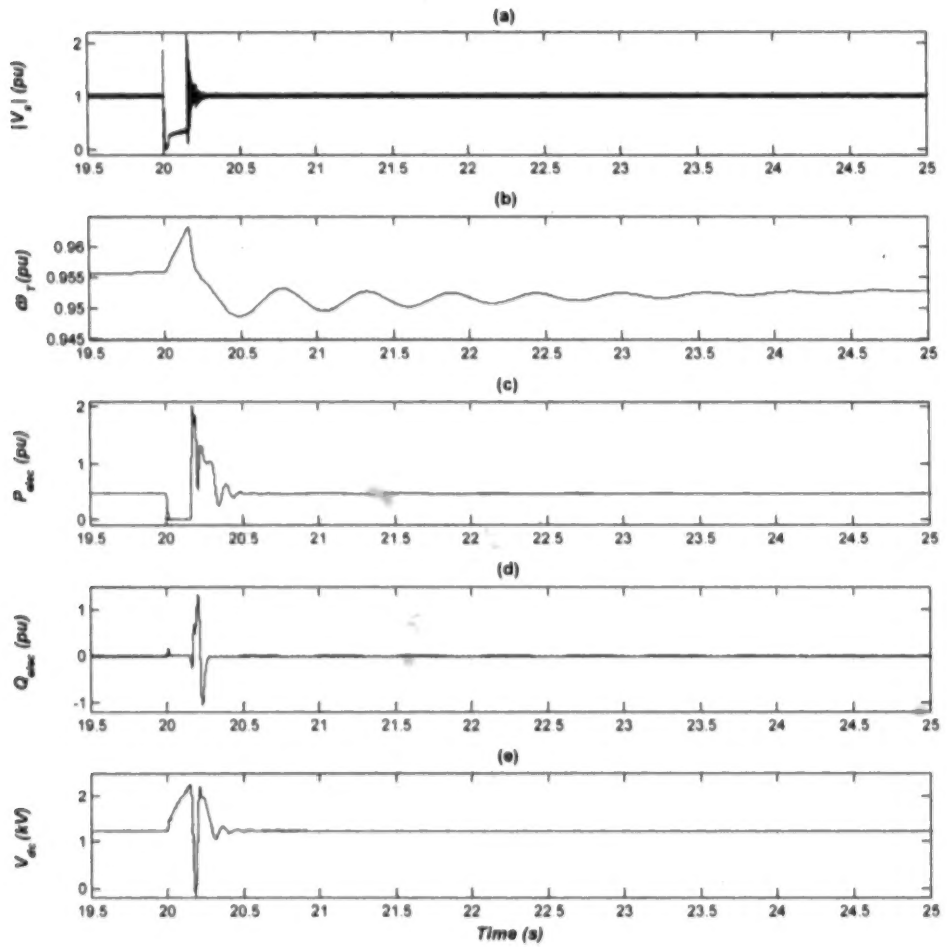

Figure 5.8: Impacts of the three-phase-to-ground fault on the WTGS internal parameters: (a) magnitude of the supporting voltage; (b) turbine rotational speed; (c) generated active power; (d) generated reactive power; (e) DC-link voltage

and Q_{elec} were dropped to zero and remained constant until the fault was cleared. Inspecting waveform of V_{dc} in Fig. 5.8 (e) and 5.9 (d) revealed that the grid voltage supporting power the was provided from the rotor through the BBC. During the fault, V_{dc} was continuously increased to almost double the controlled value to release the power from the rotor. When $|V_s|$ was reduced, the amount of power

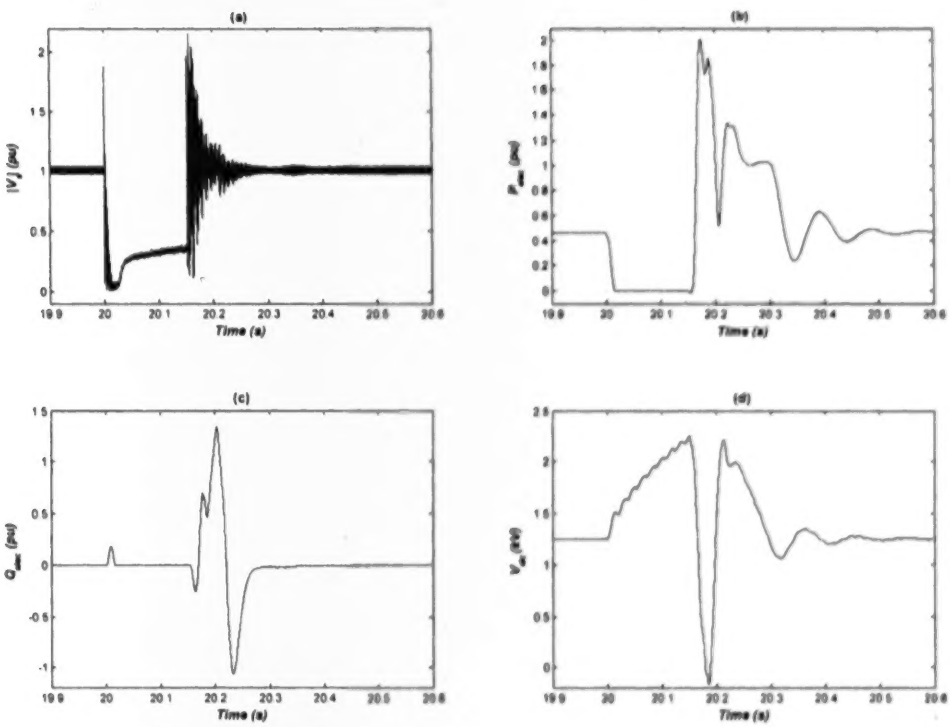

Figure 5.9: Zoom-in view of Fig. 5.8: (a) magnitude of the supporting voltage; (b) generated active power; (c) generated reactive power; (d) DC-link voltage

flowing from the stator was decreased. To direct the constant mechanical power to the grid, the only remaining path was through the rotor terminal. This increase in power transfer has increased $|V_s|$ and V_{dc} over time. Nevertheless, the rotor could only release a portion (30%) of the total power available. Consequently, the imbalance in mechanical and electrical torque drove the turbine to higher speed, as shown in Fig. 5.8 (b).

When the fault was normally cleared at $t = 20.15s$, the ideal source forced all the voltages and currents in the transmission system back to the normal three-phase reference frame with the same fundamental frequency. Simulation results presented in Fig. 5.7 demonstrate that the damping of in-rush current created high frequency oscillations through the transmission system. Although the magnitude

of the three-phase fault was much larger, the balanced post-fault behavior was far less damaging than that observe in Case 1; the transient voltage and current amplitudes were very close to their steady-state values.

Because the transient behavior in the grid was moderate, the post-fault oscillations in $|V_s|$ were relatively small. When $|V_s|$ was restored, the system regained its generation capacity through the reactivated stator path. Huge amount of power release were recorded in the P_{elec} and Q_{elec} waveforms, Fig. 5.9 (b) and (c). This sudden shift in the power direction has collapsed the DC-link voltage. Steady reduction of V_{dc} (Fig. 5.9 (d))to zero after the fault indicated that less and less power was transferred from the rotor. Instead, the turbine speed was reduced during the post-fault energy release, and power started to flow back into the sub-synchronously rotating rotor. This was why the V_{dc} was pushed back to a very high value momentarily after dipping to zero. As the entire WTGS reaches its steady-state, all the electrical parameter rested their pre-fault operating conditions.

Since the power variation was significant during the three-phase fault, the acceleration and deceleration of the turbine became more obvious. However, the waveform of ω_T showed that the maximum change in speed was less than 3%.

5.3.2.3 Case 3: Two-phase-to-ground fault

This case study investigates the effects of $9cycle/0.15s$ two-phase-to-ground fault at bus B2. As shown in Fig. 5.10 (a) and (c), the fault applied at $t = 30s$ forced the phase-a and b voltage at bus B2 and B3 to zero. With the unbalanced three-phase voltage and small grounding resistance at bus B2, huge distortions in the line currents were observed in the results presented in Fig. 5.10 (b) and (d).

During the fault, the waveform for $|V_s|$ shown in Fig. 5.11 (a) was essentially the same as the phase-b waveform given in Fig. 5.10 (c) with dc offset, and the average was $\approx 50\%$ below the nominal value. Unlike the single-phase-to-ground fault studied in Case 1, the huge oscillations propagating through the WTGS has caused the divergence in electrical control, which was proved by the collapsing V_{dc} waveform shown in Fig. 5.11 (e) and 5.12 (d). This break down of electrical control

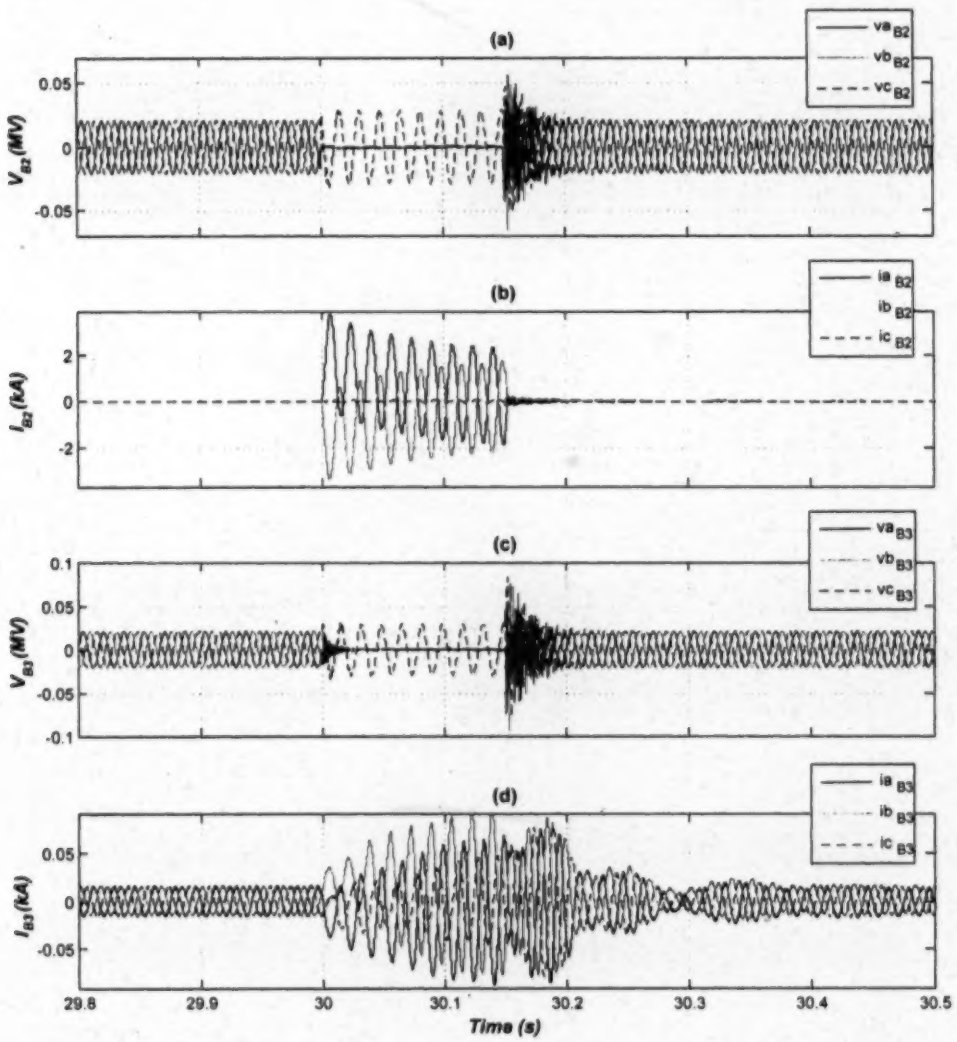

Figure 5.10: Three-phase voltage and current waveforms at bus B2 and B3 during the two-phase-to-ground fault

was resulted from the loss of synchronism. As two of the three phases disappeared, the controller has loss its ability to accurately calculate the positions of the various reference frames, in which the essential vector control took place. Blindly imposing control in some arbitrary frame has only prompted the divergence.

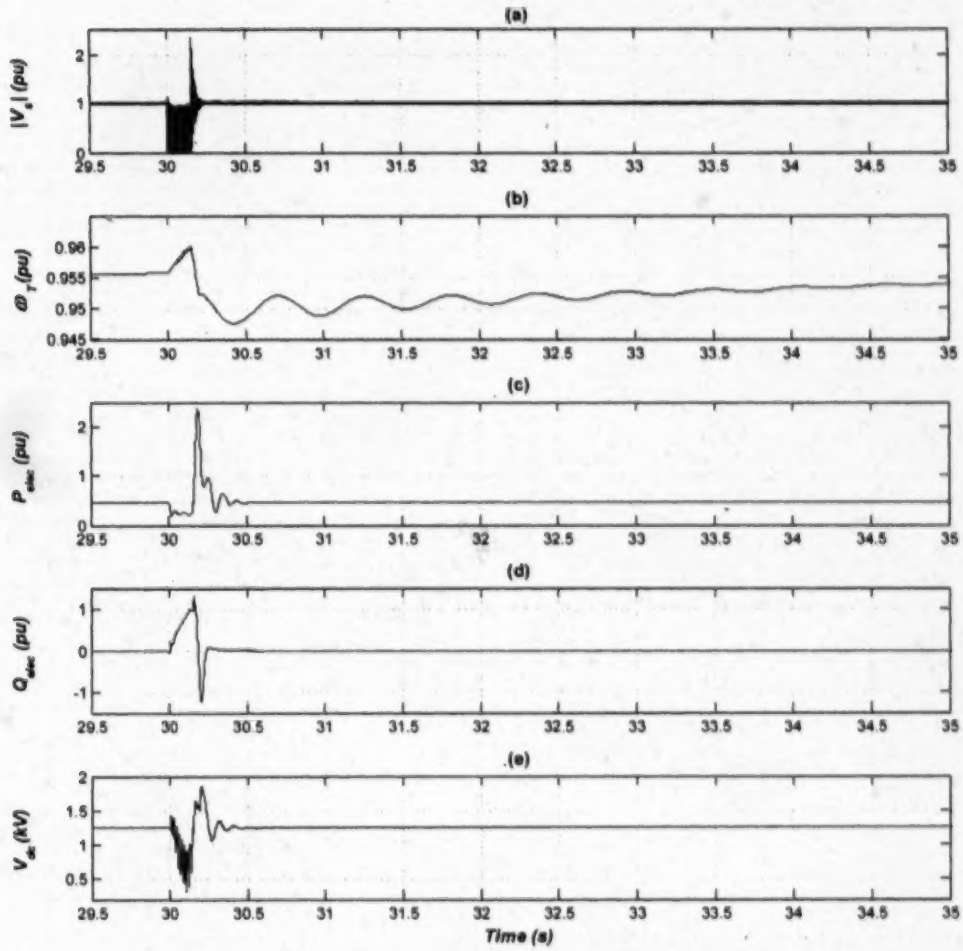

Figure 5.11: Impacts of the two-phase-to-ground fault on the WTGS internal parameters: (a) magnitude of the supporting voltage; (b) turbine rotational speed; (c) generated active power; (d) generated reactive power; (e) DC-link voltage

Since the average $|V_s|$ was reduced by half, the throughput of active power from the stator was deducted by almost the same amount, Fig. 5.11 (c) and 5.12 (b). Predictably, the imbalance of the internal torque has accelerated the turbine and forced a higher output of reactive power, as shown in Fig. 5.11 (b) and (d), respectively.

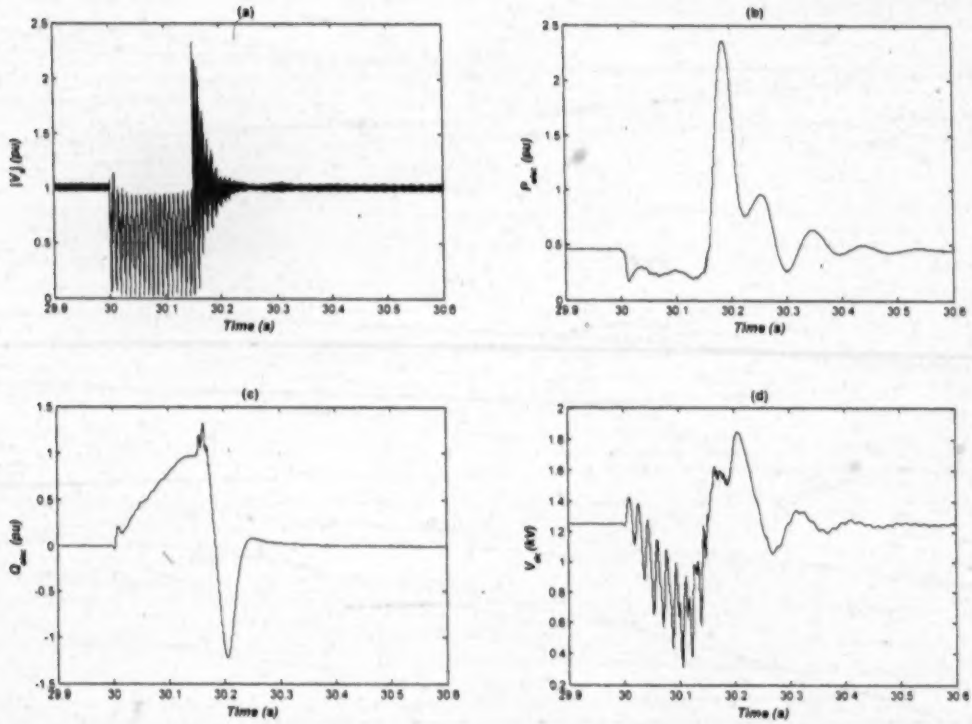

Figure 5.12: Zoom-in view of Fig. 5.11: (a) magnitude of the supporting voltage; (b) generated active power; (c) generated reactive power; (d) DC-link voltage

Before complete system failure, the fault was cleared at $t = 30.15s$. As shown in Fig. 5.10, the immediate in rush of current from phase-a and b has created the high frequency transients in the line voltage and current waveforms. Sequentially, the increase of $|V_s|$ has boosted the active power generation from the WTGS. Extracting the energy stored in the rotating turbine and rotor masses has reduced ω_T and Q_{elec}. Before the internal torques reached the equilibrium, reactive power was absorbed through the DC-link to strength the rotor flux for transmitting more power to the stator through the magnetic flux linkage.

Benefited by the rapid reaction of the controller, V_{dc} was quickly recovered to support the power demand from the rotor. For the electrical system to reach its steady-state, approximately $0.6s$ was needed. With the much larger inertia and

slower controller, the post-fault oscillation in ω_T lasted for $5s$.

5.3.2.4 Summary of Case Studies

The results from the three case studies proved that the DFIG-based WTGS has its inherited capabilities to withstand different kinds of line faults in the transmission system. More information were gathered for the further studies in controller improvement, protective device design, and operation practice for a wind energy supported network.

Summarizing overviews of the simulation results given in Fig. 5.13 helps in comparing the impact aroused by different line faults on various parameters that are internal to the WTGS. Excellent immunity to single-line-to-ground fault was observed in the first case study. Relatively small disturbance was recorded in the generated active and reactive power during the fault. However, the post-fault response has demonstrated the need for current-limiting device in the line to reduce the influences of the unbalanced post-fault in-rush current on $|V_s|$, Fig. 5.13 (a). It was also found that the reduction in the grid-side electrical controller's sensitivity to terminal voltage will improve the post-fault transient response in active power generation.

By qualitative measure, the simulation results for the three-phase fault highly agreed with that reported in [47]. Even without any protection device implemented, the WTGS was still able to survive the most severe line fault. Nevertheless, the study has revealed the vitality of the converter protection devices. When the three-phase fault was encountered, the converters will be highly stressed by the reversal voltage and current from the rapid charging and discharging processes (Fig. 5.13 (e)). Without a protection device, the magnitude and duration of the high voltage and current might push individual switches over their thermal limit causing break down.

Among the three line faults studied, it was concluded that the two-phase-to-ground fault was the most damaging as it caused the divergence in the electrical system control. To prevent damage to the components, the WTGS must be

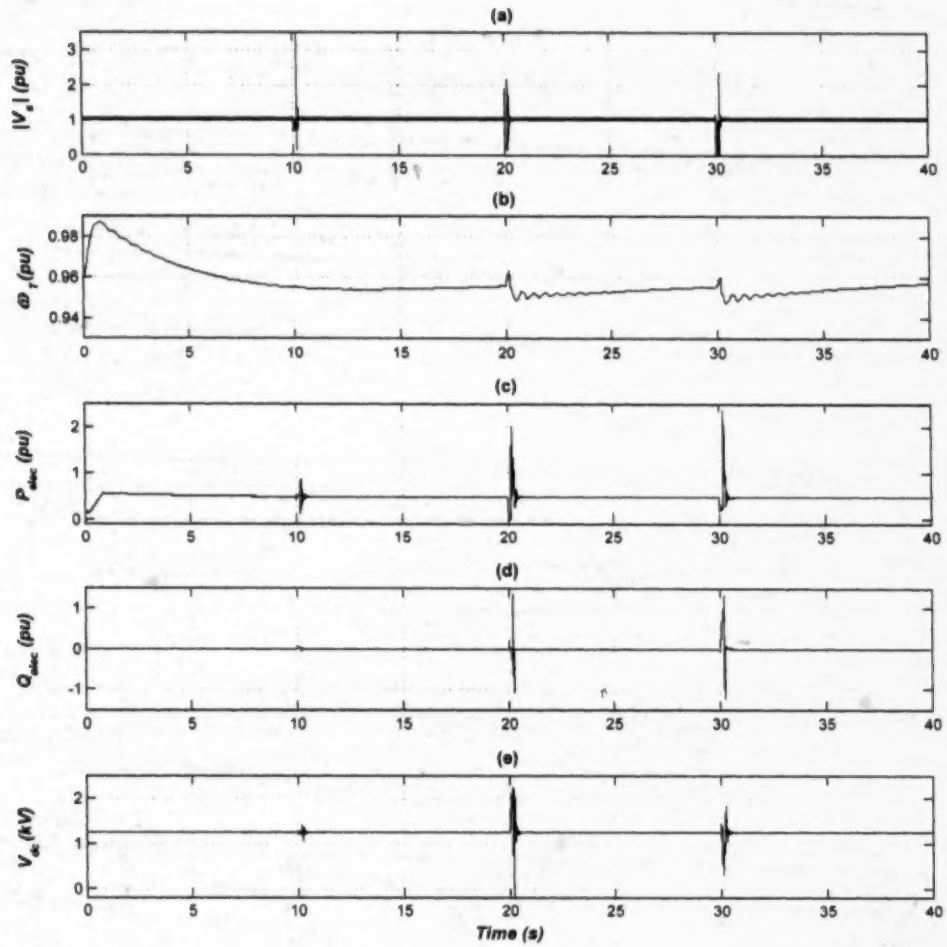

Figure 5.13: Overviews of the impacts from the various line faults

disconnected from the grid when the length of the fault exceeded a specific threshold. However, the stability maybe improved by modifying the controller to retain its synchronism with the only remaining phase voltage.

The relatively constant w_T shown in Fig. 5.13 (b) should encourage the ongoing development of higher rating WTGSs [2]. High rating WTGS requires a larger turbine to capture more power from wind, and the increase in turbine mass will substantially increase the stability of the entire system. From the

fault response studies, the captured power was found buffered in the spinning mechanical components. When the electrical parts failed to distribute the power, the mechanical components will be accelerated to temporarily sustain the excess power. If the mass of the turbine and stiffness of the shaft were increased, the unevenness in w_T during faults might be further reduced. Nevertheless, the electrical system must be strengthened, and more systematic fault clearing procedures should be taken to handle the huge amount of post-fault active and reactive power discharge and absorptions, as shown in Fig. 5.13 (c) and (d).

Mainly benefitted by the fast acting power electronics and controllers, the DFIG-based WTGS has proven competent in meeting the emerging LVRT requirements. To further improve the performance and stability, the recommendations discussed above can be considered. With the given WTGS model, new controller design or protection device concepts can be easily implemented and tested using software simulators off-line. Nevertheless, if users wish to verify the functionality of an existing hardware, employing real-time simulation with a HIL setup will be an accurate and economical option.

5.3.3 Real-Time Simulation of the Complete DFIG-based WTGS

To maximize the benefit of the complete DFIG-based WTGS model presented in the previous sections, a RT time counterpart can be developed with the hardware interfacing feature enabled. On the RT simulator, the developer can simulate the RT WTGS model in high resolution and generate the necessary results for the external devices connected through the fast digital and analog I/O modules. If the device is still in the pre-fabrication stage or has limited availability, it can be modeled and simulated in a separate *node*, and interfaced with the main *node* that is executing the grid-connected WTGS in RT.

In order to demonstrate the HIL concept using RTX-LAB simulator, the setup presented in Fig. 5.1 was simulated in RT. Measurements at different points of the system was exported through the digital I/O. By feeding these simulation results to an external oscilloscope, which could be replaced by any other hardware

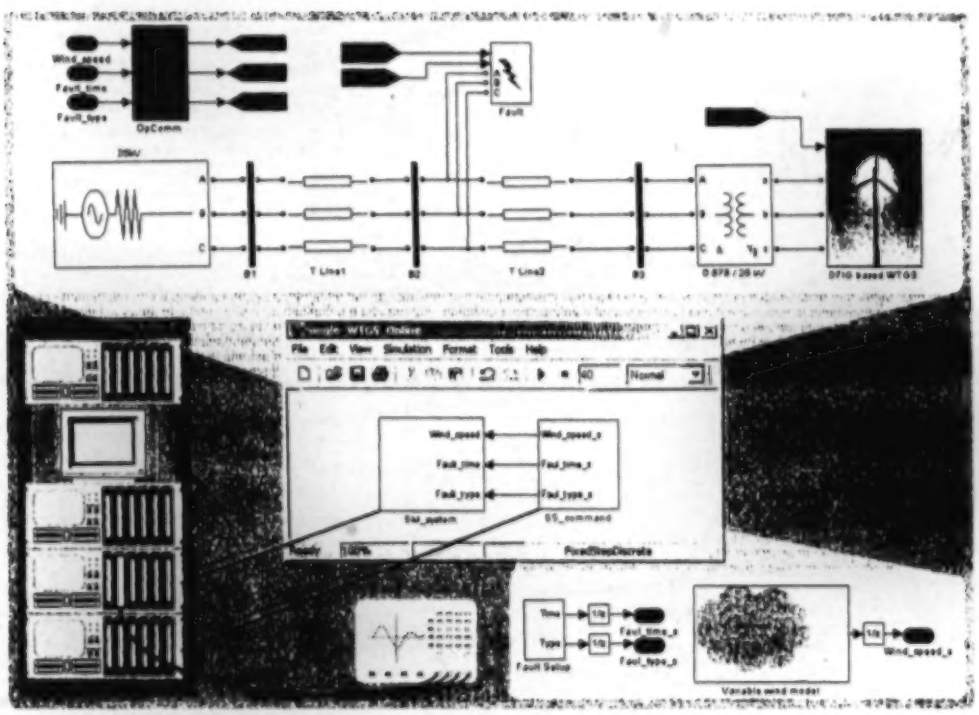

Figure 5.14: Voltage and current waveforms at bus B2 and B3 : (a) at the beginning; and (b) at the end of the supply voltage sag

devices, RT behavior of the WTGS was monitored. To mimic the commands sent from the external devices, the wind speed model and the fault generator were simulated in a separate *node*.

As shown in Fig. 5.14, the master subsystem, prefixed with 'SM_', contains the complete WTGS and the transmission system models; the slave subsystem, prefixed with 'SS_', contains only the wind speed and fault generator models. Since the preparation of the most complex DFIG configuration for RT simulation has been demonstrated in Chapter 4, developers only need to ensure that the transmission system were constructed using the built-in discrete SPS models.

The signals transmitted between the subsystems must be defined as states with the postfix '_s'. By inserting a step-delay, as shown in Fig. 5.14, the scalar value was automatically converted into a state. If more accuracy is required, the pole-

zero compensation technique discussed in section 4.4.3 can be applied.

For exporting data through the I/O module, a hardware synchronizing controller block called "OpHSDIO" must be included in the model. By simply feeding the desired signals to the controller block, external devices would receive the corresponding signals at the assigned ports.

After the pre-compilation, the executables for the subsystems were loaded onto two separate *nodes*. While the wind speed signal and the fault command were sent from the slave to the master subsystem, measurements were simultaneously taken and delivered to the oscilloscope. This high bandwidth communication is centrally managed by the Field Programmable Gate Array (FPGA) controlled network interfacing card. Although no actual device was involved in this demonstration, the operation principle, setup, and demand on computation resources would be nearly identical.

The RT simulation was executed with $50\mu s$ time-step. To examine the simultaneous response of the WTGS to variable wind speed and line faults, the wind signal similar to that illustrated in Fig. 5.3 (a) was fed to the aerodynamic model, and similar line faults patterns investigated in the previous section were imposed to the transmission line.

In Fig. 5.15-5.17, the side-by-side comparison of the oscilloscope traced RT simulation results with the corresponding off-line simulation results recorded from SIMULINK® prove the accuracy and stability of the RT model. Over the $40s$ simulation time frame, the simulator capabilities were able to perform the complex mathematical calculation while supervising the intensive communication among different hardware components. However, the simulator was still under utilized. From the performance monitoring log, Table 5.1, the maximum computation time was $15.375\mu s$ for the *node* running the master subsystem. To finish the execution cycle for the slave subsystem, only $2.257\mu s$ was needed. Including the $6.628\mu s$ overhead for communication, the maximum execution time was still well below $50\mu s$.

The virtual HIL RT simulation presented the opportunity for applying the

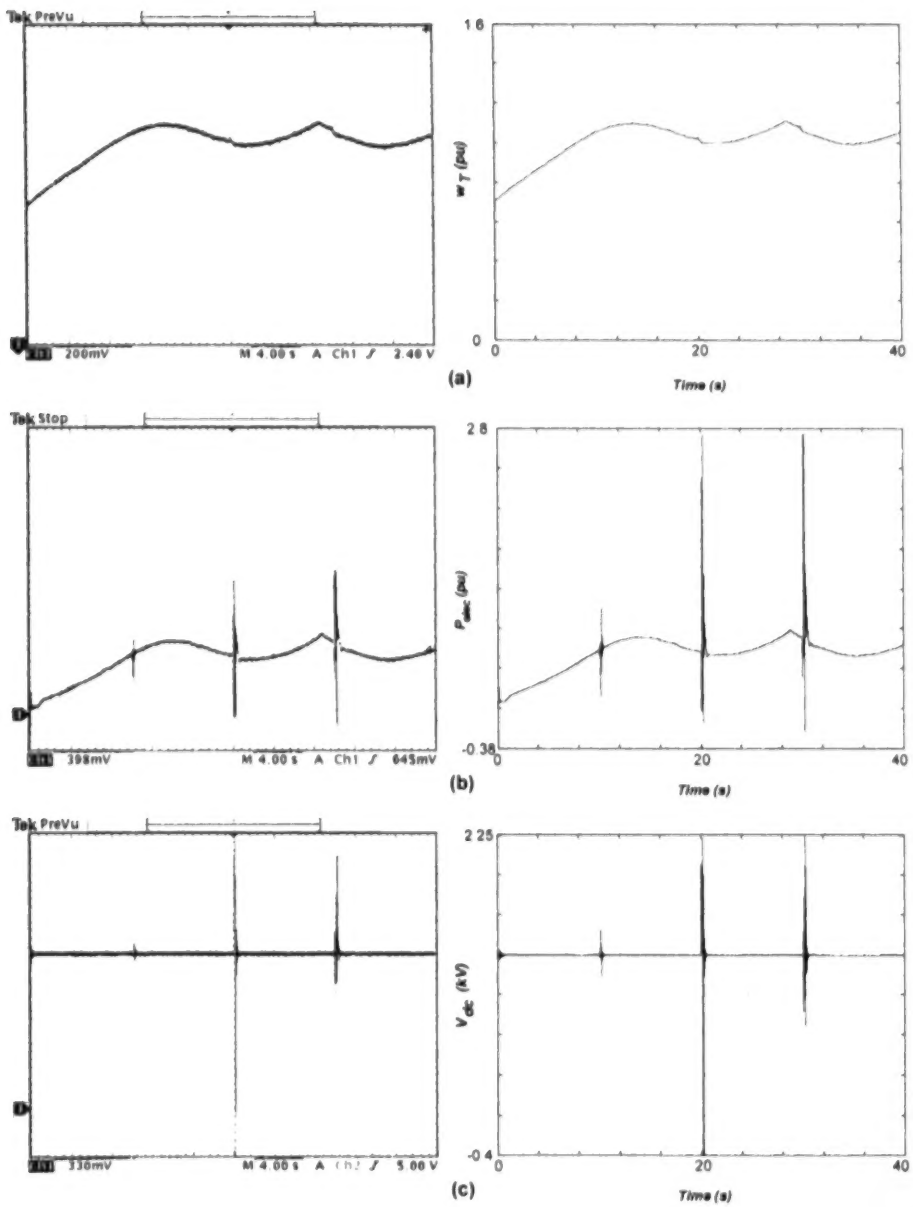

Figure 5.15: Comparisons of the oscilloscope traced RT simulation results (left) with the corresponding off-line results generated using SIMULINK® (right): (a) turbine rotational speed; (b) generated active power; (c) generated reactive power

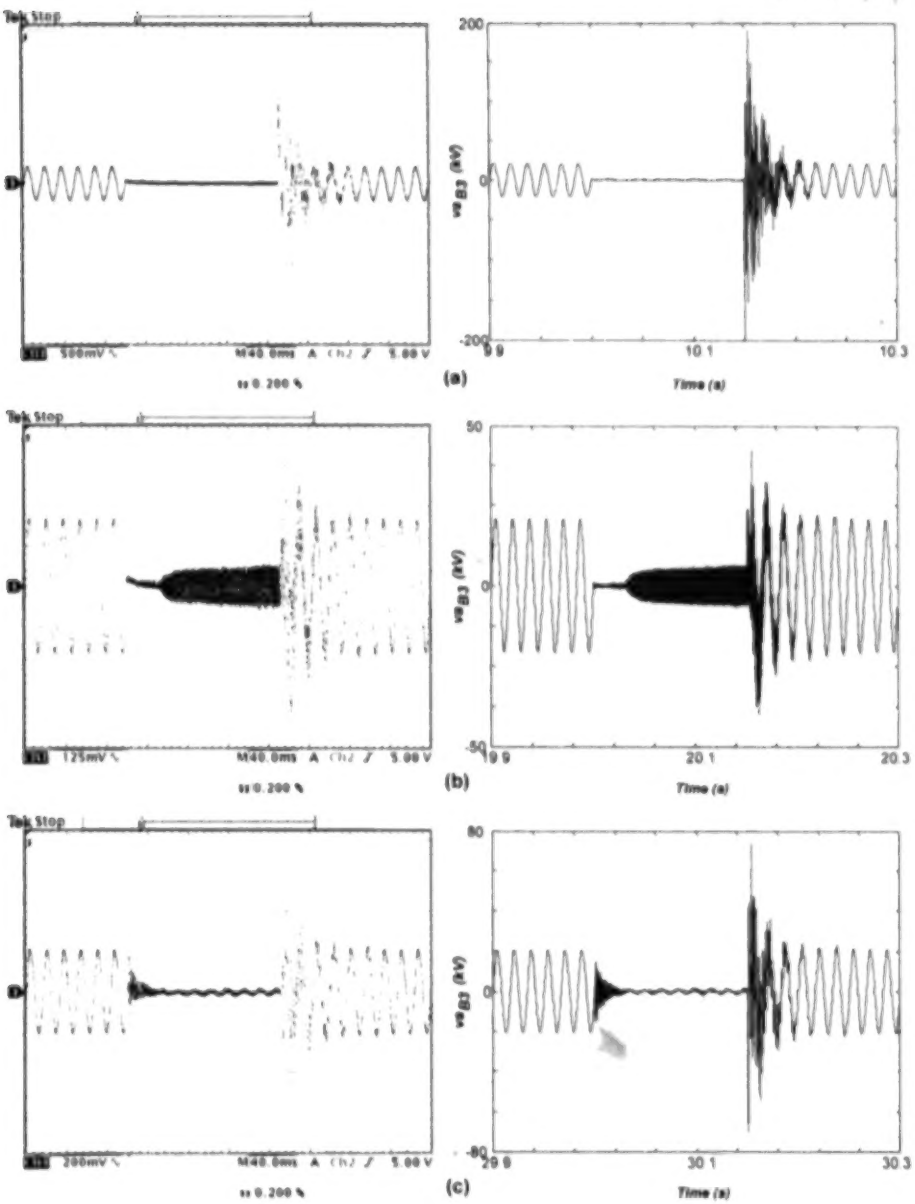

Figure 5.16: Comparisons of the oscilloscope traced RT simulation results (left) with the corresponding off-line results generated using SIMULINK® (right): phase-*a* voltage at bus B3 during (a) single-phase-to-ground fault; (b) three-phase-to-ground fault; (c) two-phase-to-ground fault

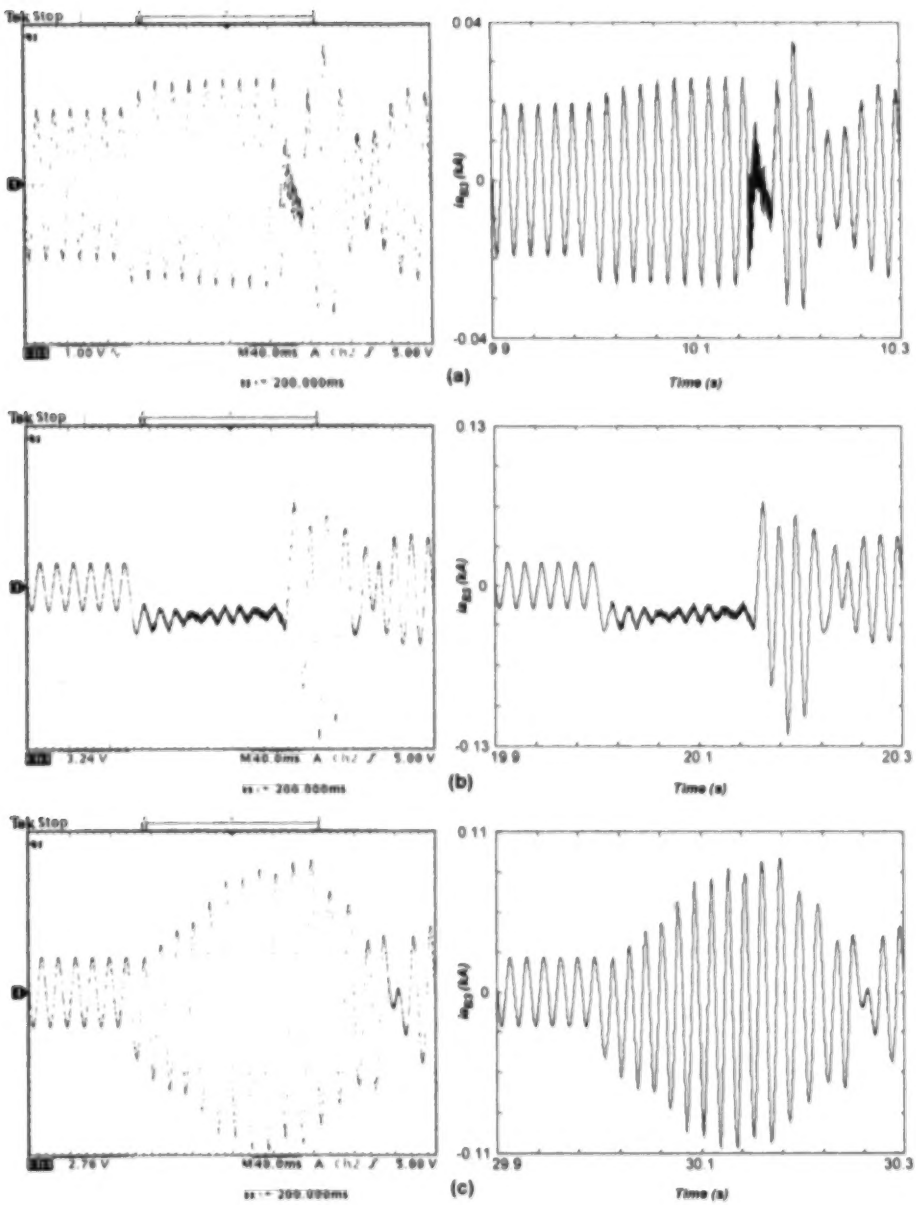

Figure 5.17: Comparisons of the oscilloscope traced RT simulation results (left) with the corresponding off-line results generated using SIMULINK® (right): phase-*a* current at bus B3 during (a) single-phase-to-ground fault; (b) three-phase-to-ground fault; (c) two-phase-to-ground fault

Table 5.1: Performance log for the RT virtual HIL simulation

Time Distribution	Master (μs)	Slave (μs)
Computation Time	15.375	2.257
Idle Time	24.770	39.819
Data Acquisition	0.995	0.305
Status Update	0.290	0.290
Target Request Time	0.062	0.067
Host Request Time	0.045	0.047
Synchronization	0.075	0.054
Signal To Master	–	6.628
Signal From Master	–	–
Signal To Slave	–	–
Signal From Slave	6.628	–
Others	0.840	0.533
Total Step-Size	50	50

complete WTGS model into practical research and development studies. Using the proposed WTGS model as the fundamental building block, developers can easily modify the system to meet their specific needs. With the flexible software and hardware configuration, the study can be expanded to include more details and more components.

5.4 Wind Farm Structure and Dynamics

Studies on the single grid-connected WTGS has provided the fundamental building blocks and the necessary tool-set for the model construction and analysis of a wind farm. To bring out the most salient characteristics of a wind farm, its electrical connections and physical attributes must be clearly defined.

5.4.1 Structure of the Wind Farm

As shown in Fig. 5.18, the ten DFIG-based WTGSs of a wind farm were electrically divided into four groups. Each WTGS had its own 0.575/25kV distribution transformer connected to the sub-collector bus (cB1 - 4). Through the collector transformer, the voltage is boosted to transmission level $138kV$. At the end of the

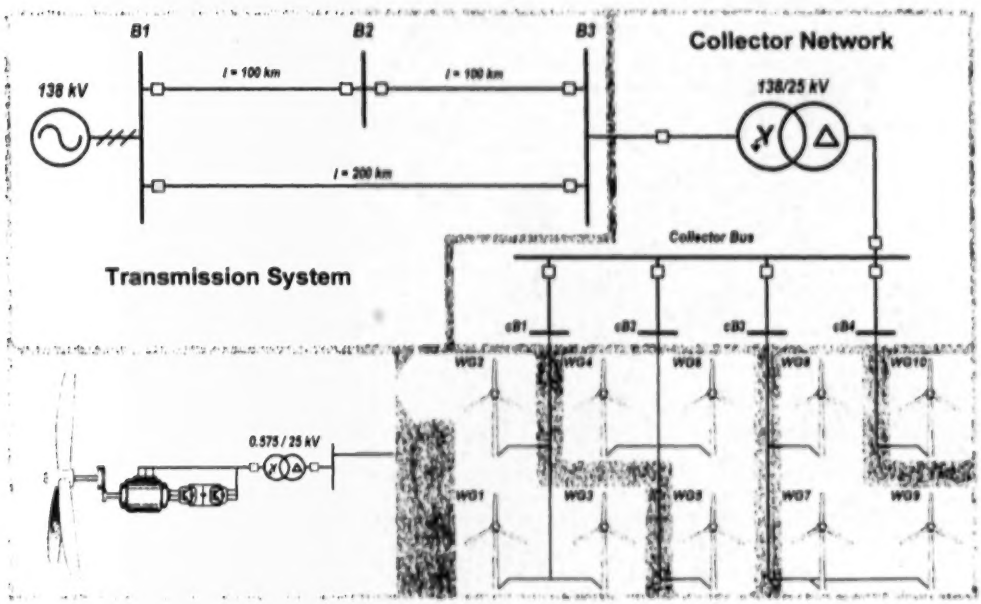

Figure 5.18: Wind farm schematic

parallel feeder, the infinite bus B1 is backed by an ideal three-phase voltage source.

The geographical illustration shown in Fig. 5.19 indicates that the WTGSs were equally spaced on the same altitude with no surrounding obstacles. Average wind speed was assumed to be the same across the entire wind farm. In the direction indicated in Fig. 5.19, the gust, ramp, and turbulence riding on the average wind speed would concurrently affect WTGS 1, 2, and 3 first; then 4 and 5; and so on.

Referring to the physical descriptions given above, the detailed wind farm model was developed under MATLAB®/SIMULINK®. For the best accuracy, the complete WTGS model verified in the previous section was employed. Since the study was not focused on the protection system, the relays and circuit breakers were ignored. Wirings internal to the wind farm were omitted mainly due to their low impedances and relatively short length. Nevertheless, the cables connecting the sub-collector buses to the main collector bus, and the transmission lines supporting the entire wind farm were represented with the conventional distributed parameter line model.

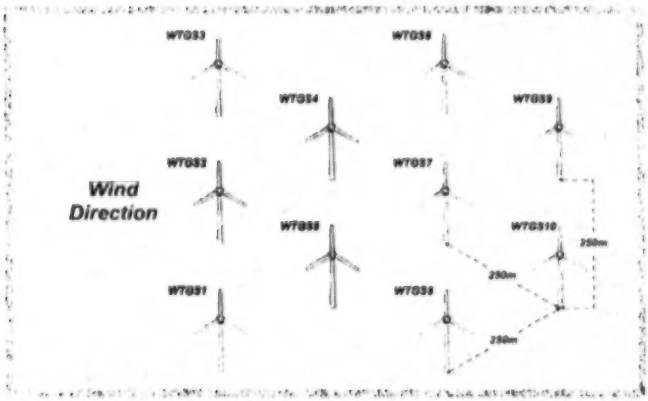

Figure 5.19: Physical attributes of the wind farm and the hypothetical wind direction

The main reason for modeling the line sections between the collector and sub-collector buses with the $50km$ distributed parameter line model was to introduce a time delay. This delay is critical for the latter model separation technique employed for the real-time simulation of the detailed wind farm model. Although the line length and the impedances associated with the line may not reflect the real world situation, the practice is considered valid for the study of real-time simulation realization and aggregation technique development.

5.4.2 Dynamics of the Wind Farm

In order to reflect the geographical location and distance, the wind speed signals feeding to different WTGSs were individually coordinated. Since WTGS 1, 2, and 3 were the first to be affected by the wind digressions, the wind speed patterns, Fig. 5.20 (a), experienced by these three WTGSs became the modulation reference. As the average wind speed was set to $11.3m/s$, a $19.16s$ delay was created for the forefront of the wind variations to reach the consecutive sets of WTGSs. This explains why the variations in the wind speed signals sent to WTGSs 4 and 5, Fig. 5.20 (b), was started at $t = 19.16s$. Based on the same principle, the wind signals delivered to WTGS 6, 7, and 8, Fig. 5.20 (c), and those generated for WTGS 9 and 10, Fig. 5.20 (d), were respectively delayed by $38.32s$ and $57.48s$ with respect to

Fig. 5.20 (a).

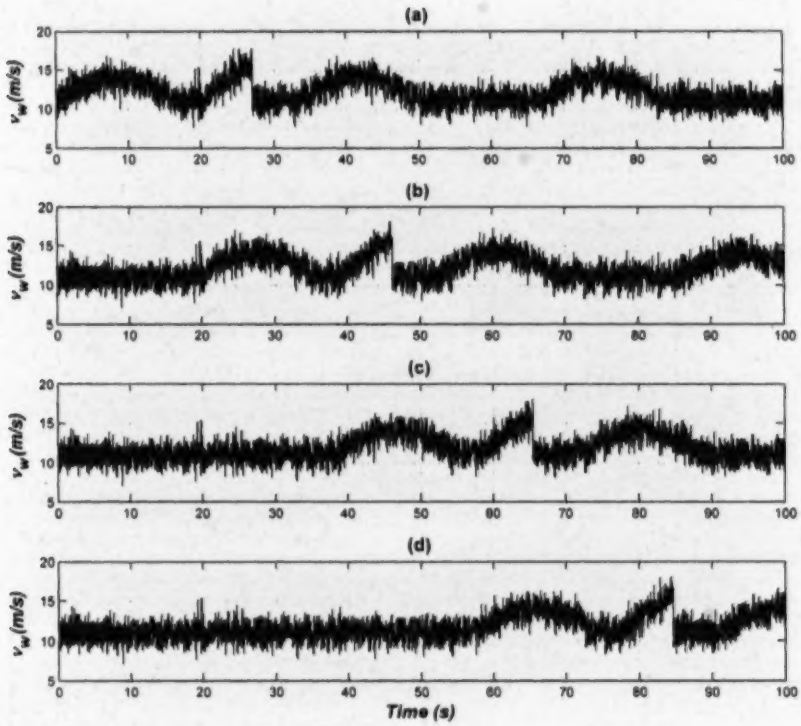

Figure 5.20: Synthesis of the variable wind speed signals for (a) WTGSs 1, 2, and 3; (b) WTGSs 4 and 5; (c) WTGSs 6, 7, and 8; (d) WTGSs 9 and 10

For the $100s$ off-line simulation, all the WTGSs were initialized under exactly the same conditions. Control objective for the WTGSs was to produce maximum active power at unit power factor. Simulation time-step was fixed to $50\mu s$. As the aggregated behavior of the wind farm is more important, the active (P_{coll}) and reactive (Q_{coll}) powers at the collector bus were measured and presented in Fig. 5.21.

The variations in P_{coll} were the recordings of the collective wind farm response to the wind alternations. Since the measurements were taken at the collector bus, the waveform of Q_{coll} showed how would the $50km$ line section affect the collective reactive power. With the given controller design, the WTGSs would only monitor

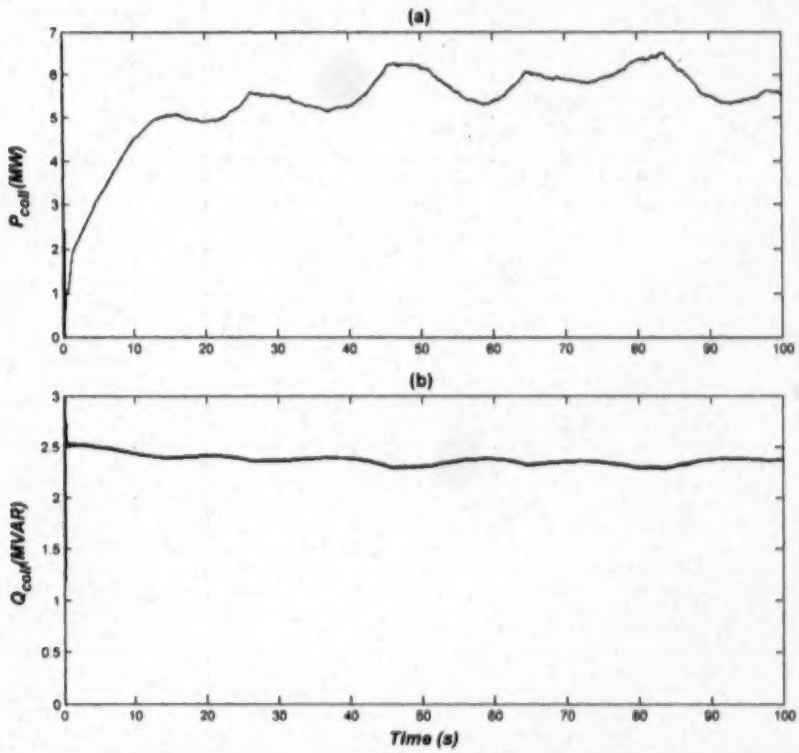

Figure 5.21: Wind farm response to variable wind speed measured at the collector bus: (a) generated active power; and (b) generated reactive power from the wind farm

and regulate the reactive power at the low-voltage side of their own distribution transformer to zero. As the internal wirings were ignored, the power factor at the sub-collector buses should be very close to unity. However, the active currents flowing toward the collector bus have excited the shunt capacitances associated with the cables, and in turn increased the reactive power generation.

To form a high resolution benchmark for later aggregation studies, fault response of the wind farm was investigated. The three kinds of grid faults studied in Section 5.3.2 were imposed on the first transmission line at bus B2, Fig. 5.18. By observing the collector bus active and reactive power waveforms depicted in Fig. 5.22, the wind farm was proved to be capable of riding through all the fault disturbances, and the responses were very closely resembling the corresponding

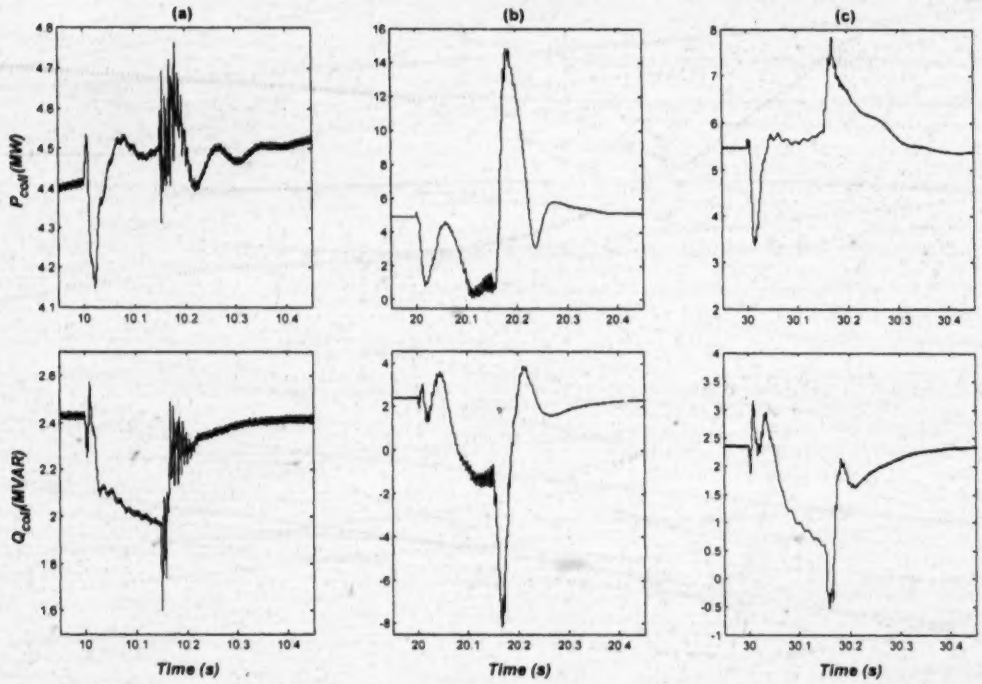

Figure 5.22: Wind farm responses to various grid faults measured at the collector bus: (a) single-line-to-ground fault; (b) three-phase-to-ground fault; (c) two-phase-to-ground fault

results recorded for the single grid-connected WTGS.

5.4.3 Real-Time Simulation of the Wind Farm

Solving the wind farm model demanded computation power of eight 3GHz CPUs. To complete the $100s$ off-line simulation in SIMULINK®, 10022.0s was needed on average. One way to increase the simulation turnaround time would be executing the model on a RT simulator. Besides speed increase, the added features from the simulator will also extend the range of investigations, such as HIL testings.

By referring to the computation time recorded for the RT simulation of a single grid-connected WTGS in Table. 5.1, it was concluded that a maximum of three detailed WTGS models can be simulated on a single *cluster node* with the time-step fixed to $50\mu s$. In order to evenly distribute the computation load across a *target*

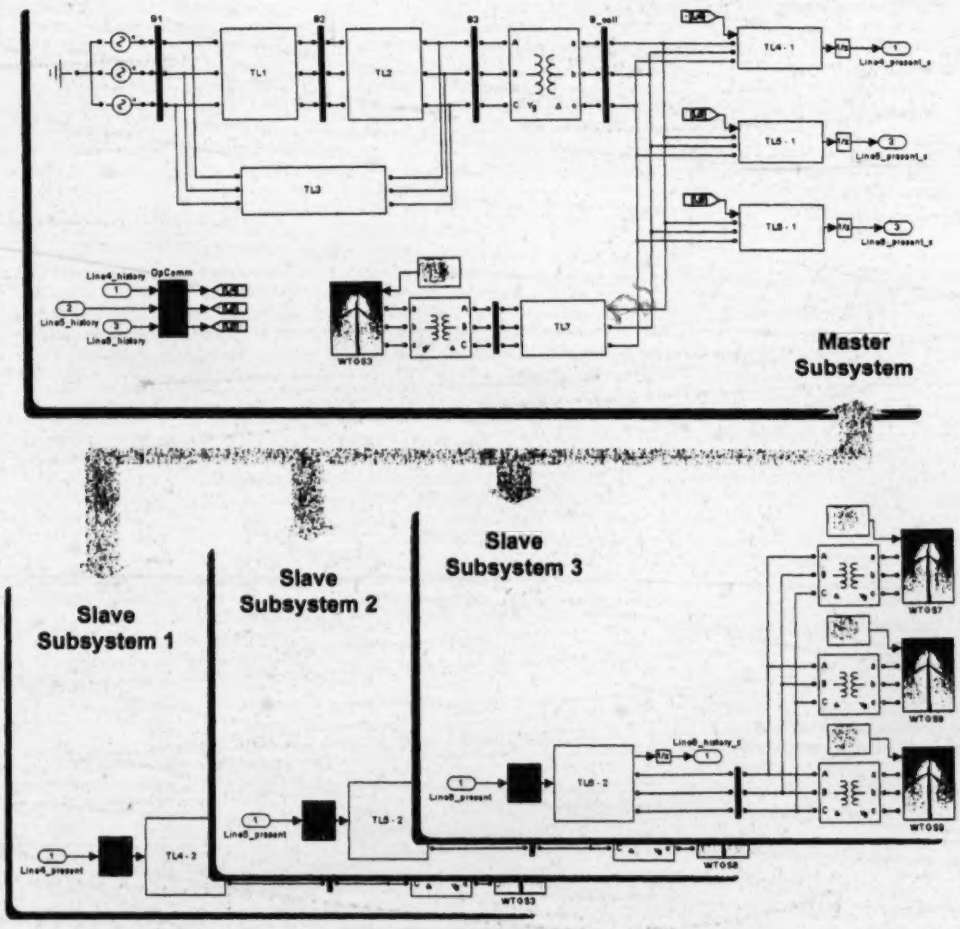

Figure 5.23: Division of the detailed wind farm model for RT simulation

cluster, the complete wind farm was divided into four subsystems, as shown in Fig. 5.23. Communication between the master and slave subsystems was established through the Bergeron transmission line model [80].

Due to the length and characteristic impedance, electrical signals send from one end of a transmission line will be received at the other end with a time delay τ. Because of this delay, the transmission line can be model as two separate yet interdependent portions. By knowing the history terms from one portion, the

other portion can calculate its present state using simple nodal analysis. After splitting the transmission line model in two, one portion was retained in the master subsystem connecting to the collector bus, and the second portion was accommodated in the slave subsystem linking the WTGSs. Only the history terms from both portions were communicated to either side with a step-delay.

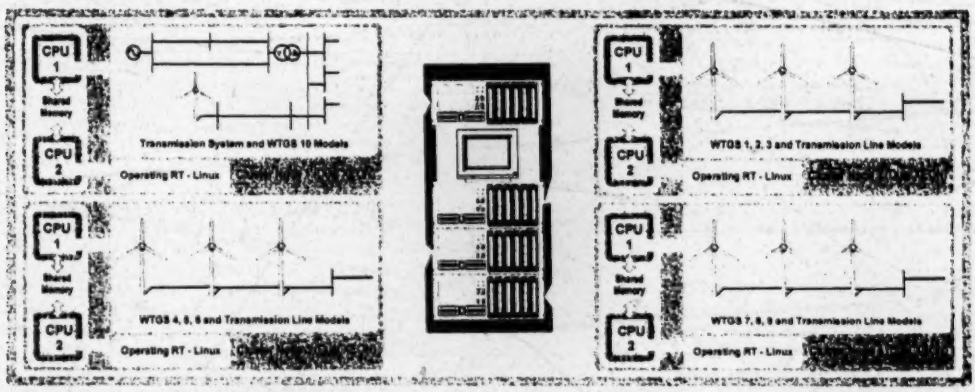
CPU 1
Shared Memory
CPU 2
Transmission System and WTGS 10 Models
Operating RT - Linux
WTGS 1, 2, 3 and Transmission Line Models
Operating RT - Linux
WTGS 4, 5, 6 and Transmission Line Models
Operating RT - Linux
WTGS 7, 8, 9 and Transmission Line Models
Operating RT - Linux

Figure 5.24: Distribution of the subsystems across the *target cluster*

In theory, this model division technique should also increase the simulation speed. Since the entire electrical network was divided into four parts linked with data signals, four smaller sets of state-space matrices should be formed to represent the linear electrical components. Based on the DFIG optimization studies in Section 4.4, a smaller state-space matrix can be solved with less time.

After loading the executables for the four subsystems onto the *target cluster* (Fig. 5.24) RT simulation of the wind farm was started and simulation results were exported to an external oscilloscope. By comparing the RT simulation results with the corresponding off-line simulation results from SIMULINK® (Fig. 5.25 and 5.26), the model division technique was validated. However, the performance log tabulated in Table 5.2 signalled the need for further model simplification. Summation of the communication overheads and the computation time revealed that the *cluster nodes* were working at their limit under the $50\mu s$ time constraint.

The last row of Table. 5.2 showed that the time-step has overrun the $50\mu s$ limit.

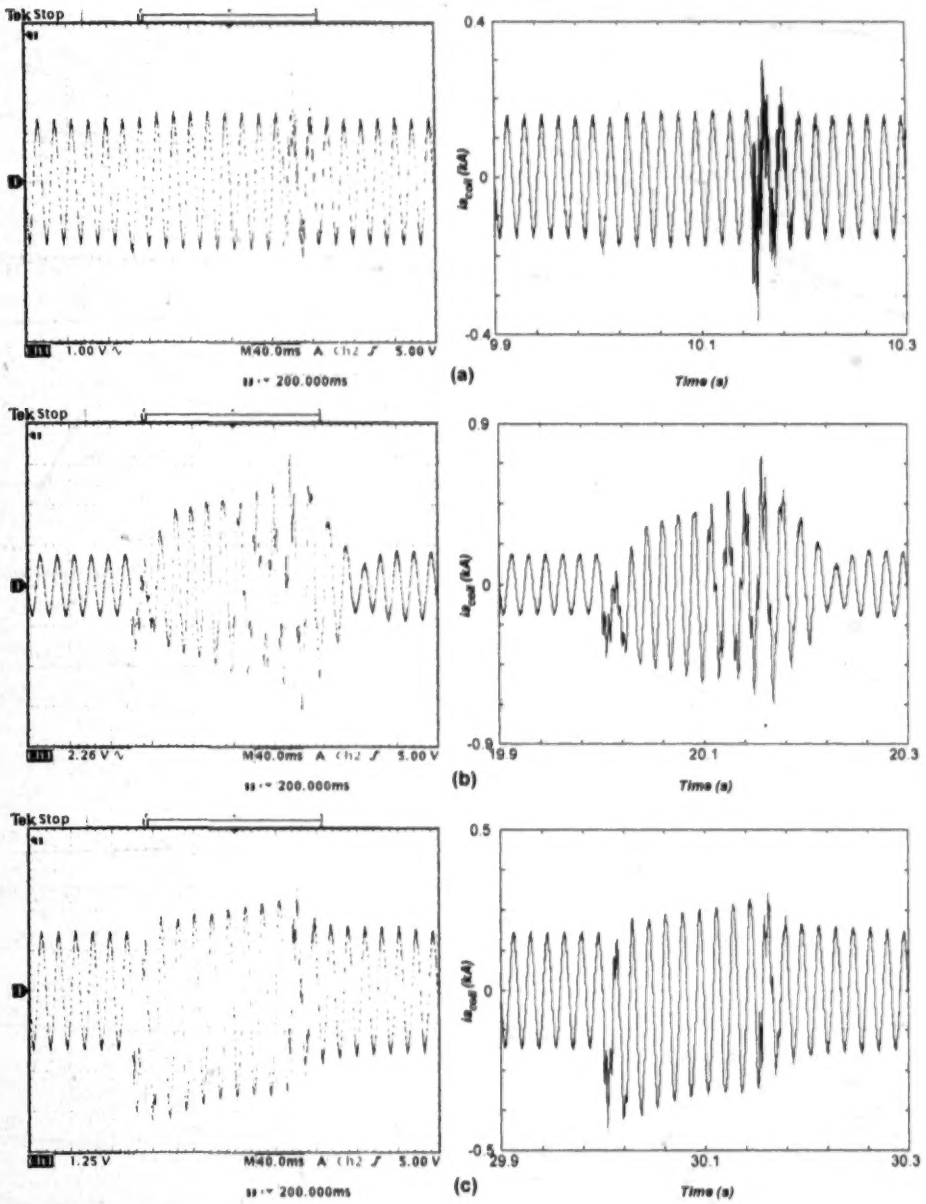

Figure 5.25: Comparisons of the oscilloscope traced RT simulation results (left) with the corresponding off-line results generated using SIMULINK® (right): phase-*a* voltage at the collector bus during (a) single-phase-to-ground fault; (b)three-phase-to-ground fault; (c) two-phase-to-ground fault

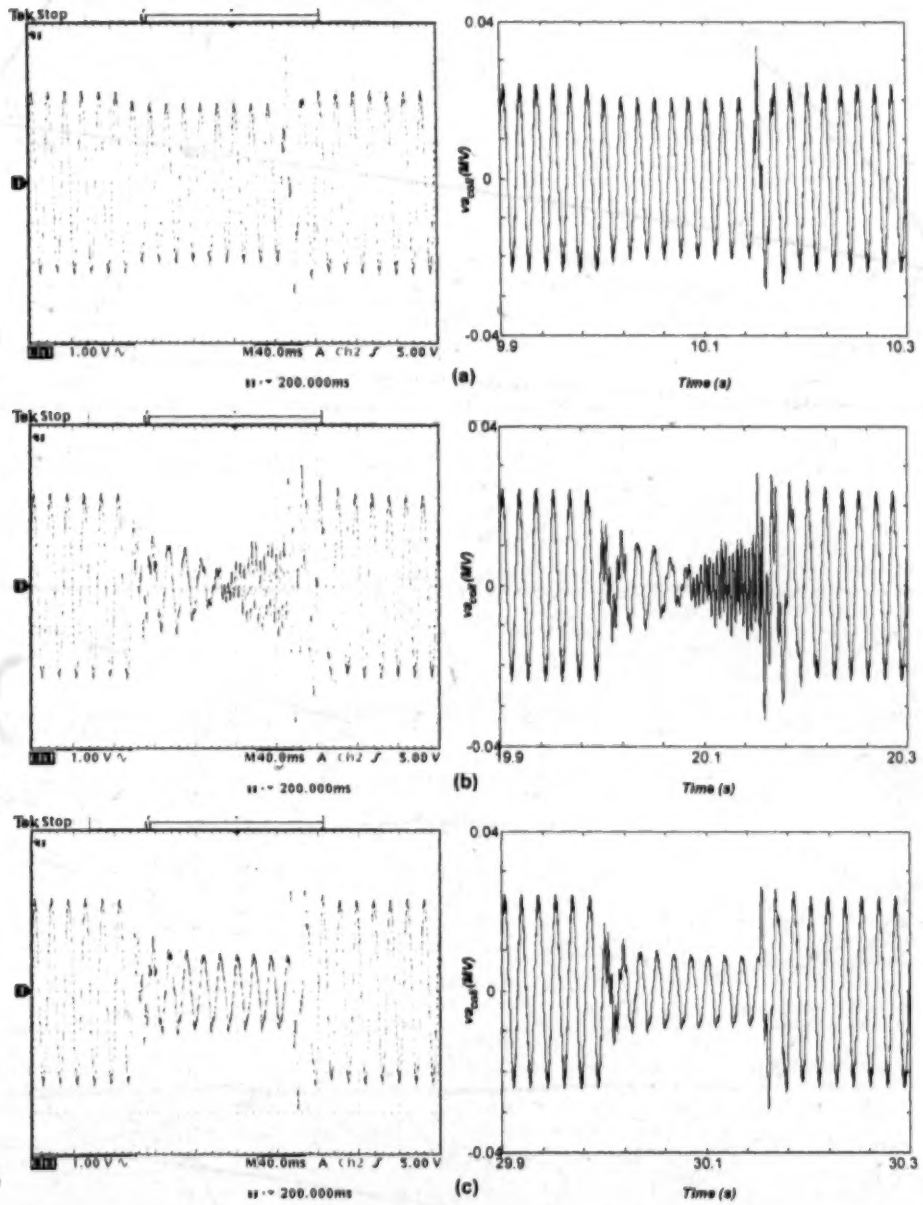

Figure 5.26: Comparisons of the oscilloscope traced RT simulation results (left) with the corresponding off-line results generated using SIMULINK® (right): phase-*a* current at the collector bus during (a) single-phase-to-ground fault; (b)three-phase-to-ground fault; (c) two-phase-to-ground fault

Table 5.2: Performance log for the RT simulation of the detail wind farm model

Time Distribution	Master (μs)	Slave1 (μs)	Slave2 (μs)	Slave3 (μs)
Computation Time	16.327	42.420	42.758	42.300
Idle Time	-2.887	0.035	0.033	0.038
Data Acquisition	1.442	1.420	1.337	1.352
Status Update	0.515	0.370	0.363	0.375
Target Request Time	0.075	0.075	0.073	0.075
Host Request Time	0.042	0.040	0.040	0.037
Synchronization	0.042	0.043	0.035	0.039
Signal To Master	–	6.338	6.432	6.178
Signal From Master	–	1.992	2.117	1.975
Signal To Slave1	6.338	–	–	–
Signal From Slave1	14.768	–	–	–
Signal To Slave2	6.265	–	–	–
Signal From Slave2	0.075	–	–	–
Signal To Slave3	6.415	–	–	–
Signal From Slave3	0.040	–	–	–
Others	0.933	0.545	0.472	0.909
Total Step-Size	53.278	53.278	53.278	53.278

Because the simulator needed more time to finish the necessary computation and communication, the time-step was automatically expanded. It was obvious that the communication overhead was the main cause of the overruns. As the intensive computation has already pushed the *nodes* executing the slave subsystems close to the time limit, not enough margin has left to handle the communications. Although the situation can be resolved by simply enlarging the time-step, versatile solutions are needed to satisfy the more demanding studies.

5.5 Wind Farm Aggregation

To reduce the amount of time and computational resources needed for the studies of wind farm, the most straightforward solution is to develop an aggregated model that is capable of representing the collective behavior of multiple or all the WTGSs. Different levels of aggregation can be achieved through attuned utilizations of the data regarding the physical attributions and electrical properties of the wind

farm. In this section, three levels of aggregation are presented to demonstrate the solutions for some of the potential obstacles.

5.5.1 Level One Aggregation

According to the wind farm layout and wind direction given in Fig. 5.19, strong correlation between the vertically aligned WTGSs allowed division of the wind farm into four regions, as shown in Fig. 5.27. To represent the collective generation capacity within each region, an equivalently rated WTGS model can be used. For example, the replacement WTGS model of Region 1 had the rating of $5.01MVA = 3 \times 1.67MVA$.

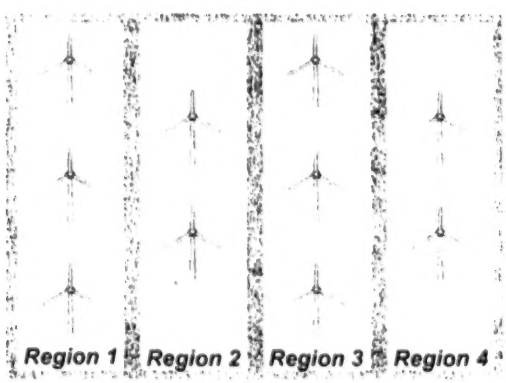

Figure 5.27: Division of the wind farm for Level One aggregation

The higher rating WTGSs were derived directly from the existing model with the nominal rating of $1.67MVA$. Since the WRIM in the existing WTGS model was specified with per-unit parameters, its output capacity can be proportionally increased by changing the base power. There was no need to change any other parameters because the replacement model must inherit the mechanical properties and the controller characteristics. The four aggregated models were directly connected to the four sub-collector buses shown in Fig. 5.18. Since the wind speed signals shown in Fig. 5.20 has already accounted for the sparsity of the wind farm, they were directly applied to the four aggregation models. Due to the rating

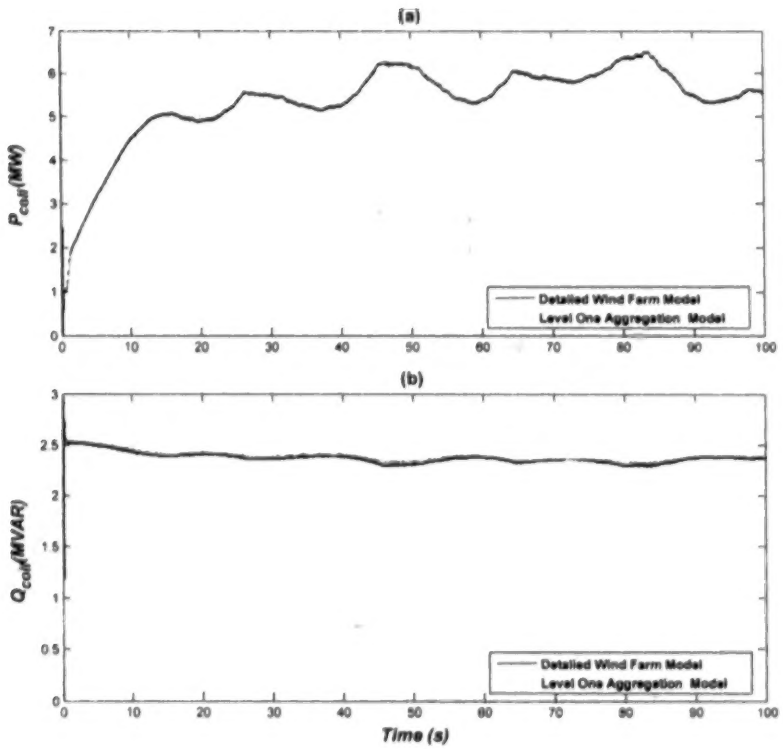

Figure 5.28: Comparisons of the variable wind speed responses generated by the detailed and Level One Aggregation model: (a) generated active power measured at collector bus; (b) generated reactive power measured at collector bus

differences, the wind speed signals shown in Fig. 5.20 (a) and (c) were applied to the aggregated WTGSs representing Region 1 and 3, respectively; the aggregated model with double the nominal capacity representing Region 2 and 4 were fed with the wind speed signals shown in Fig. 5.20 (b) and (d), respectively.

By grouping and replacing the WTGSs experiencing similar wind variations with an equivalent model, the average off-line simulation time was halved to $5542.0s$. In Fig. 5.28, comparisons of the simulation results accredited the aggregation technique. At the collector bus, the variable wind speed responses generated by the aggregation model were very close to those produced using the detailed wind farm model. Using (5.1) and (5.2), the maximum discrepancies

found in between the collector bus active and reactive waveforms were 0.92% and 3.70%, respectively.

$$\varepsilon_P = \frac{max(P_{detail} - P_{agg})}{P_{detail}} \tag{5.1}$$

$$\varepsilon_Q = \frac{max(Q_{detail} - Q_{agg})}{Q_{detail}} \tag{5.2}$$

where P_{detail} and Q_{detail} were defined as the collector bus active and reactive power generated using the detailed wind farm model, and P_{agg} and Q_{agg} were representing the collector bus active and reactive power generated using the aggregated model.

The electrical connections at the sub-collector buses may be the main contributor to the discrepancies. Since the loadings on the cables behind the sub-collector buses were altered, the cumulative behavior at the collector bus would be changed. Under the magnified views given in Fig. 5.29-5.32, the deviations becomes more obvious. For the single-line-to-ground and two-phase-to-ground faults, Fig. 5.29 (a) and (c), the aggregated wind farm model tend to under estimate the oscillations in P_{coll} and Q_{coll}. Minor dc-offsets were also observed. By referring to Fig. 5.30 and 5.32, the discrepancies were better depicted as the mismatching high frequency voltage and current components. In the enlarged views, the waveforms generated by the aggregated model could only outline those generated by the detailed wind farm model; higher frequency jitters were not closely matched.

When comparing the results for three-phase fault, Fig. 5.29 (b), it was found that the magnitudes of the post-fault power spikes were slightly exaggerated. This exaggeration was caused by the apparent mismatches in the post-fault voltage and current waveforms, Fig. 5.31. Although the pattern and timing of the responses were still considered accurate enough for electromagnetic transient analysis, the misrepresented waveforms during the fault were undesirable. Since the third harmonic was filtered by the star-delta connection of the transformer, the forth harmonic became the most prominent component in the voltage waveform, Fig. 5.31 (a). However, the aggregated model was not able to precisely match the amplitude and phase of this dominating harmonic component.

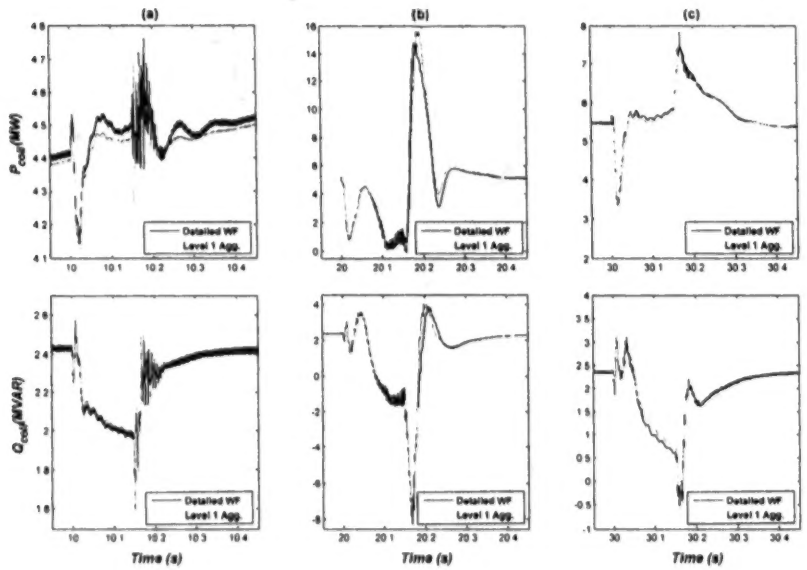

Figure 5.29: Comparisons of the fault responses generated by the detailed and Level One Aggregation model: (a) response to single-line-to-ground fault; (b) response to three-phase fault; (c) response to two-line-to-ground fault

5.5.2 Level Two Aggregation

For further aggregation, the wind farm was divided into two parts from the middle. This setup required two equivalent WTGS models with five times the nominal generation capacity. In order to preserve the physical attributes of the wind farm, the wind speed signals were finely adjusted.

For the first equivalent model representing WTGS 1-5, the wind speed pattern was constructed from the waveforms shown in Fig. 5.20 (a) and (b). Since three of the five WTGSs should experience the wind pattern shown in Fig. 5.20 (a), and the remaining two should experience what was depicted in Fig. 5.20 (b), the magnitudes of the gust and ramp were scaled accordingly. As shown in Fig. 5.33 (a), the average wind speed was still maintained at $11.3m/s$. For the second aggregated model, the re-scaled composite wind speed signal shown in Fig. 5.23 (b) was applied.

Since the entire wind farm was represented by only two equivalent WTGSs, the

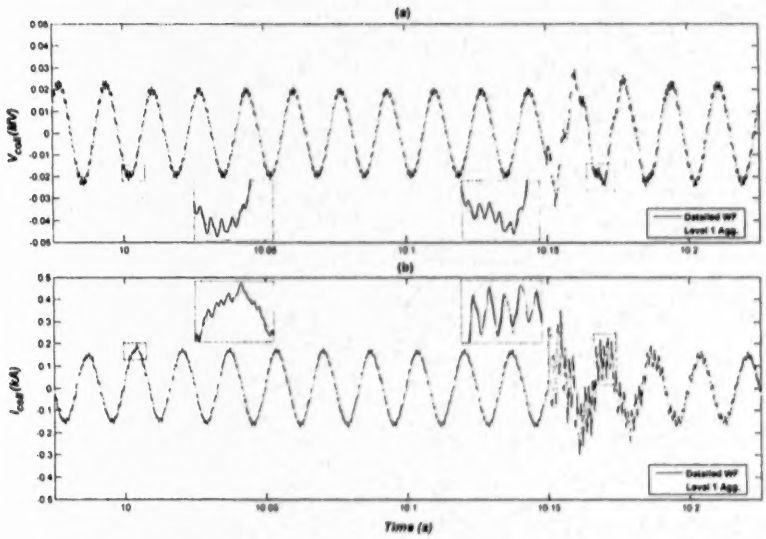

Figure 5.30: Comparisons of the collector bus: phase-*a* (a) voltage; and (b) current, during single-line-to-ground fault generated by the detailed and Level One Aggregation model

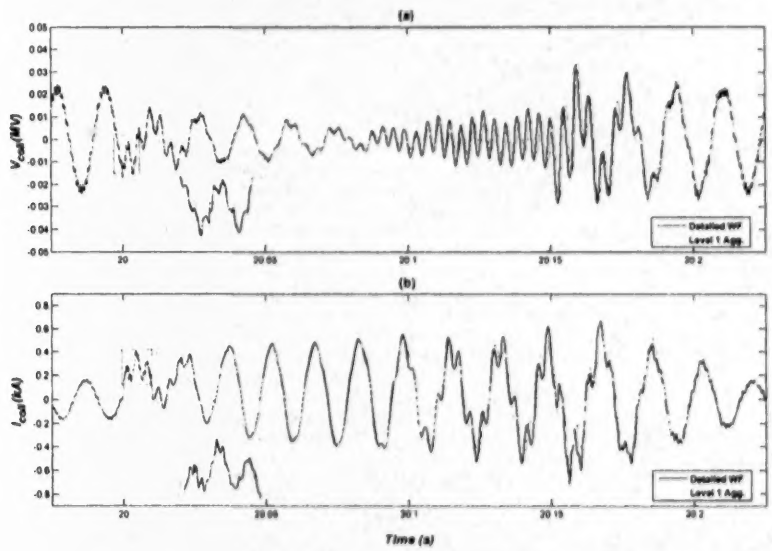

Figure 5.31: Comparisons of the collector bus: phase-*a* (a) voltage; and (b) current, during three-phase fault generated by the detailed and Level One Aggregation model

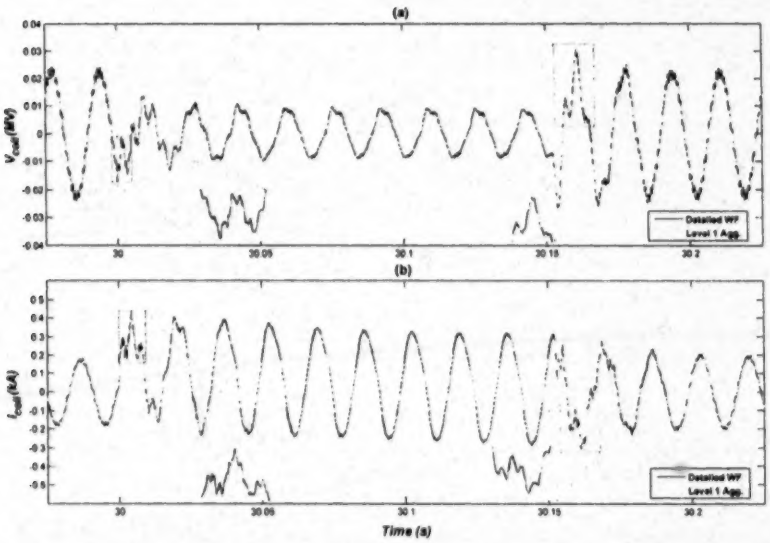

Figure 5.32: Comparisons of the collector bus: (a) phase-*a* voltage; and (b) current, during two-line-to-ground fault generated by the detailed and Level One Aggregation model

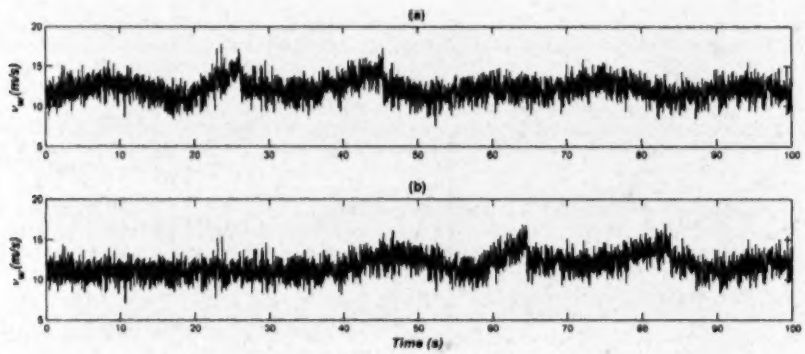

Figure 5.33: Variable wind speed signals for the Level Two aggregation model

electrical connections at the sub-collector buses were adjusted correspondingly. Two cables were put in parallel to conserve their combined effects on power transmission.

As more details were eliminated from the wind farm model, it was expected to produce a degradation in simulation accuracy for the exchange of higher

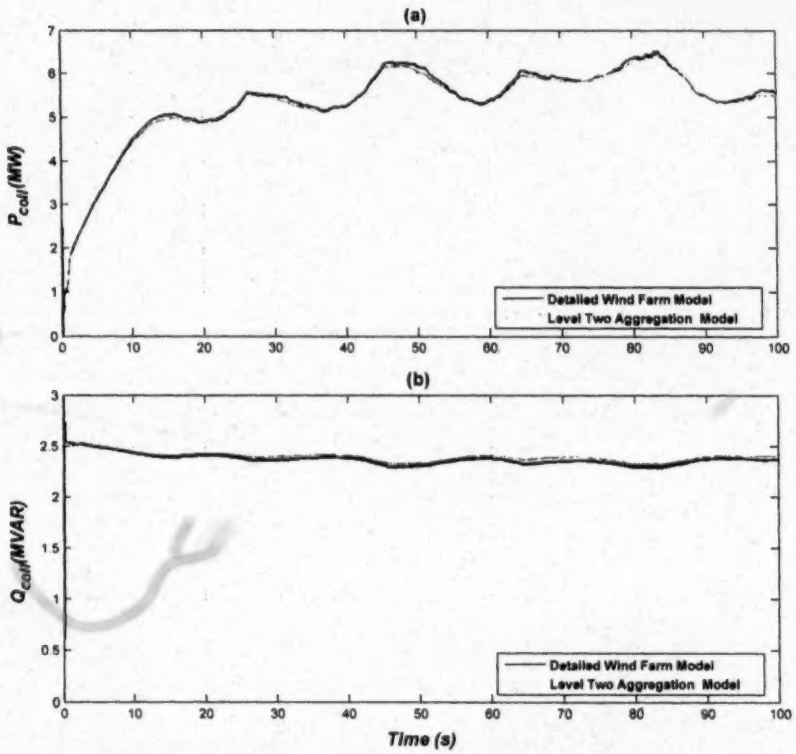

Figure 5.34: Comparisons of the variable wind speed responses generated by the detailed and Level Two Aggregation model: (a) generated active power measured at collector bus; (b) generated reactive power measured at collector bus

efficiency. In Fig. 5.34 and 5.35, comparisons of the simulation results showed larger discrepancies. The maximum deviations were increased to $\varepsilon_P = 2.42\%$ and $\varepsilon_Q = 6.04\%$. Although the wave shapes for the fault responses were still very close to those produced by the detailed wind farm model, the exaggerated power spikes along with the enlarged dc-offsets may lead to unnecessary concerns regarding fault immunity of the wind farm.

In Fig. 5.36-5.38, the fault voltage and current waveform comparisons showed further disagreements for the high frequency components. For the three-phase fault voltage waveform (Fig. 5.37 (a)), the amplitude differences and phase delay of the forth harmonic component became more obvious.

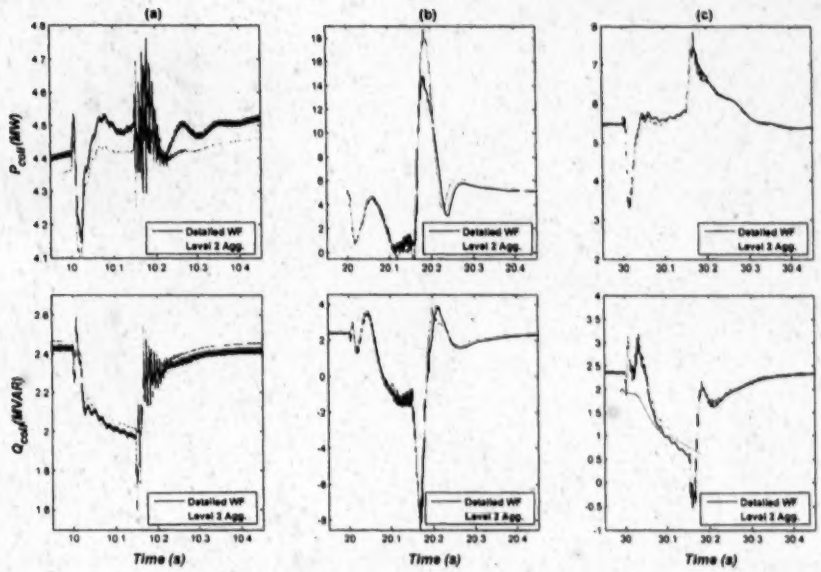

Figure 5.35: Comparisons of the fault responses generated by the detailed and Level Two Aggregation model: (a) response to single-line-to-ground fault; (b) response to three-phase fault; (c) response to two-line-to-ground fault

5.5.3 Level Three Aggregation

To achieve the highest level of aggregation, all ten WTGSs were collectively represented with an equivalent model having ten times the nominal capacity. For this highly compact wind farm model, the re-scaled wind pattern, Fig. 5.39, was synthesized from the four wind speed signals shown in Fig. 5.20. All the sub-collector buses were merged into one, and the cables connecting to the collector bus were combined in parallel. After a series of combinations, the wind farm was simplified to a grid-connected WTGS.

In Fig. 5.40 and 5.41, the simulation result comparisons showed higher discrepancies. Maximum errors calculated for the waveforms shown in Fig. 5.40 have further increased ε_P and ε_Q to 8.07% and 8.15%, respectively. In the fault responses comparisons (Fig. 5.41-5.44) the exaggeration in three-phase fault responses become more severe. For the other two fault responses, deviations from the referencing simulation results became more obvious.

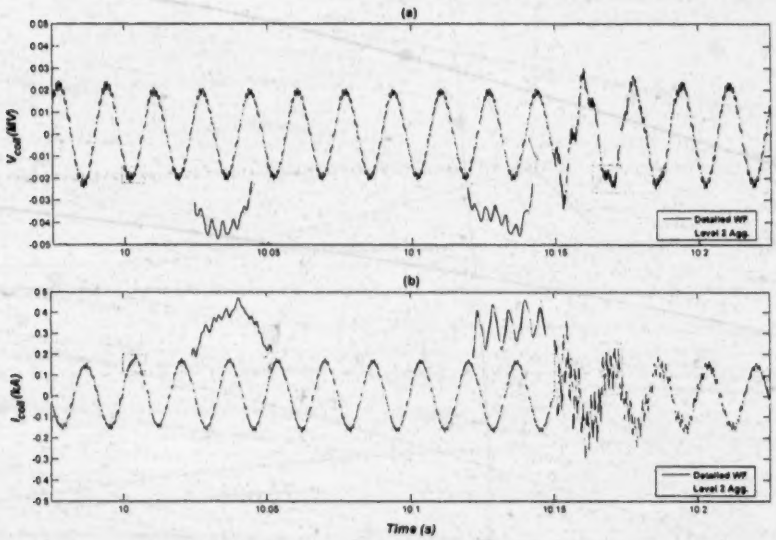

Figure 5.36: Comparisons of the collector bus: phase-*a* (a) voltage; and (b) current, during single-line-to-ground fault generated by the detailed and Level Two Aggregation model

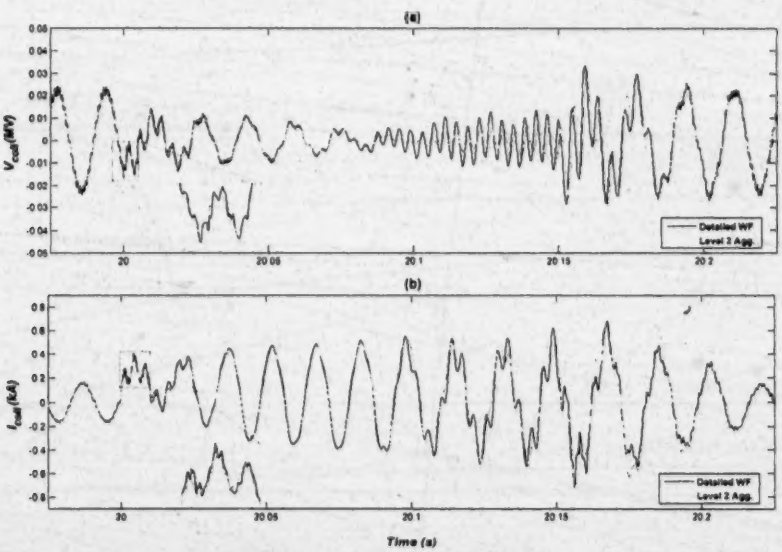

Figure 5.37: Comparisons of the collector bus: phase-*a* (a) voltage; and (b) current, during three-phase fault generated by the detailed and Level Two Aggregation model

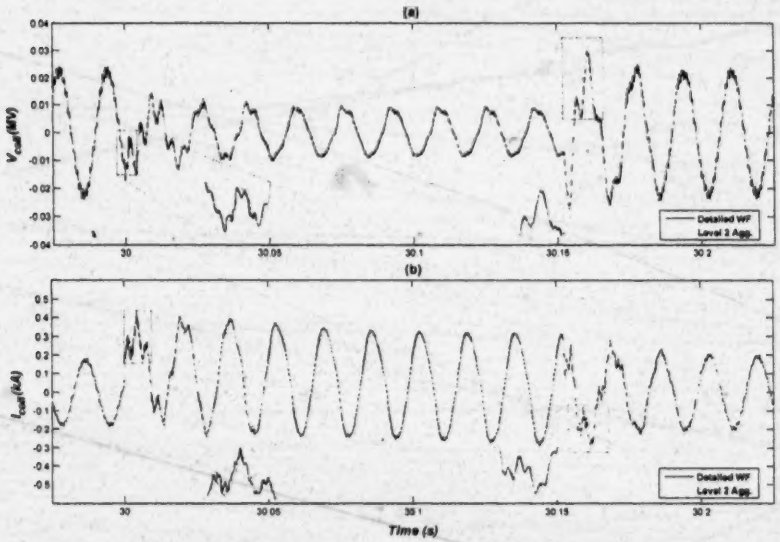

Figure 5.38: Comparisons of the collector bus: phase-*a* (a) voltage; and (b) current, during two-line-to-ground fault generated by the detailed and Level Two Aggregation model

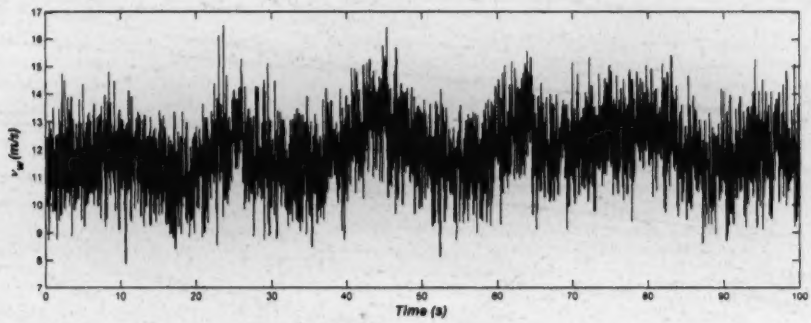

Figure 5.39: Variable wind speed signal for the Level Three aggregation model

5.5.4 Aggregation Summary

This studies conducted in the previous sections demonstrated how to effectively incorporated the physical and electrical prosperities of a wind farm for aggregation purposes. In general, it was concluded that the macro behavior of the wind farm is determined by the wind speed and the geographical properties. When it comes to matching the fast transients, such as faults responses, the aggregations of the

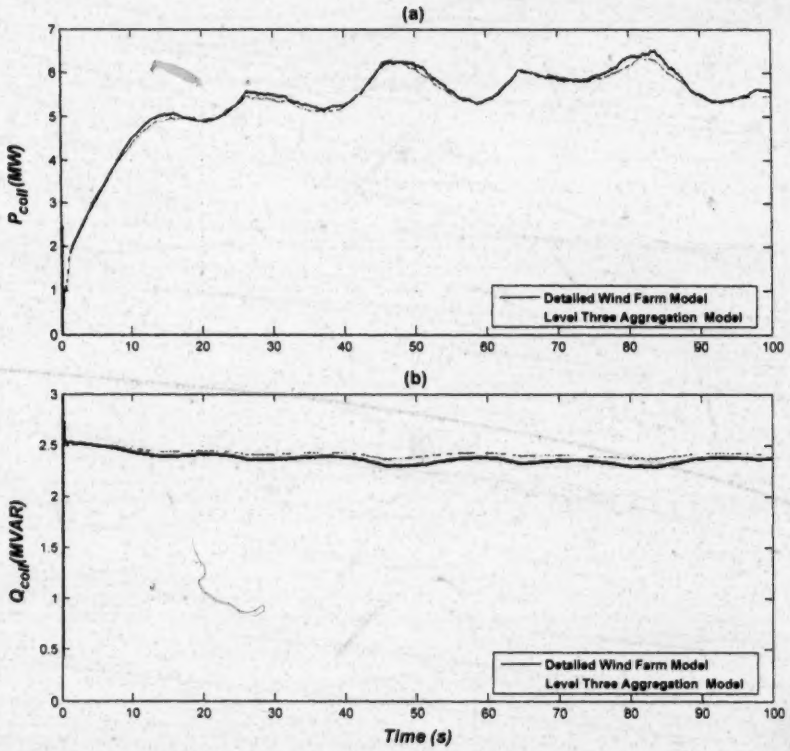

Figure 5.40: Comparisons of the variable wind speed responses generated by the detailed and Level Three Aggregation model: (a) generated active power measured at collector bus; (b) generated reactive power measured at collector bus

electrical network would have more substantial influence.

When the model becomes simpler, the simulation speed and the accuracy of the simulation results were correspondingly reduced, as summarized in Table. 5.4. Applications of these aggregated models should depend on the type of studies performed. All three models are considered sufficiently accurate for variable wind speed analysis. When it comes to analyzing the electromagnetic transient response of a wind farm, the Level One Aggregation model is generally recommended. The intermediate Level Two Aggregation model can be used to achieve the balance between simulation speed and accuracy.

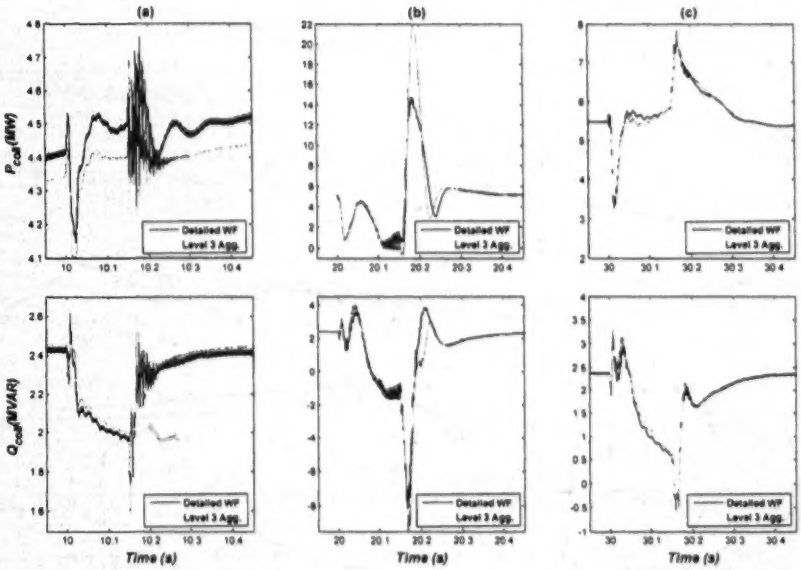

Figure 5.41: Comparisons of the fault responses generated by the detailed and Level Three Aggregation model: (a) response to single-line-to-ground fault; (b) response to three-phase fault; (c) response to two-line-to-ground fault

5.5.5 Real-Time Performance of the Aggregated Models

To investigate the benefit of adopting the aggregated models for real-time simulations, the off-line models were separated into subsystems. As shown in Table. 5.4, the Level One Aggregation model required total of three *nodes* to ensure that the simulation time-step (T_s) was kept below the $50/mus$ limit. However, the maximum computation (T_{RT}) and communication (T_{com}) times were substantially reduced when compared with those recorded for the detail wind farm model.

The real-time performance shown in the third row has highlighted the benefits of the Level Two Aggregation model. First of all, the number of *nodes* required for running the model in real-time was drastically reduced to one. This improvement not only reduced the demand on the computational hardware, but also improved the simulation performance. Since no inter-*node* communication was required, the $30.853\mu s$ computation time alone was easily fitted into the $50\mu s$ bracket. When the accuracy was also put into account, Level Two Aggregation model became the

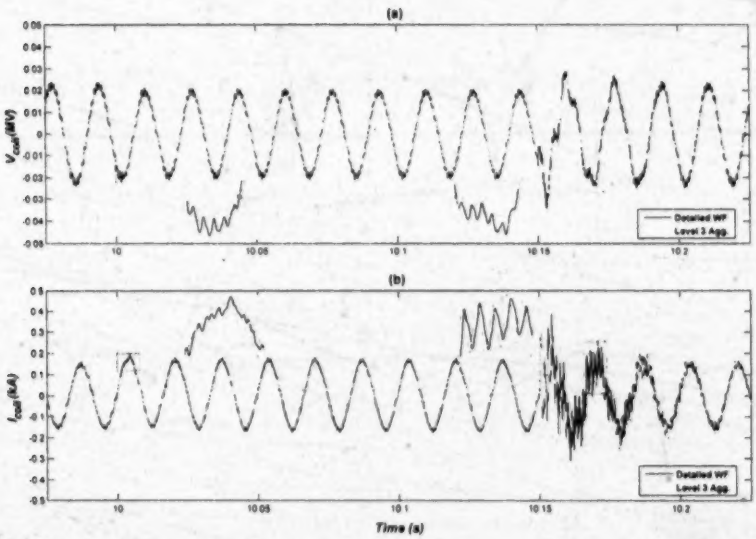

Figure 5.42: Comparisons of the collector bus: phase-*a* (a) voltage; and (b) current, during single-line-to-ground fault generated by the detailed and Level Three Aggregation model

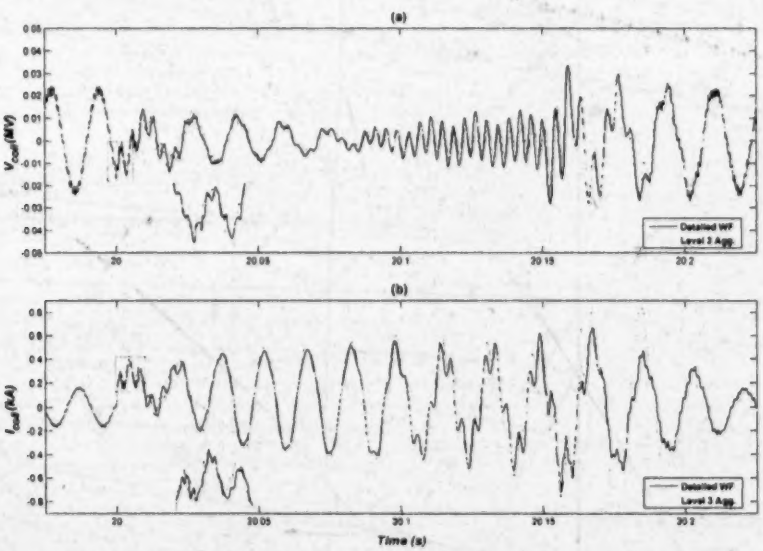

Figure 5.43: Comparisons of the collector bus: phase-*a* (a) voltage; and (b) current, during three-phase fault generated by the detailed and Level Three Aggregation model

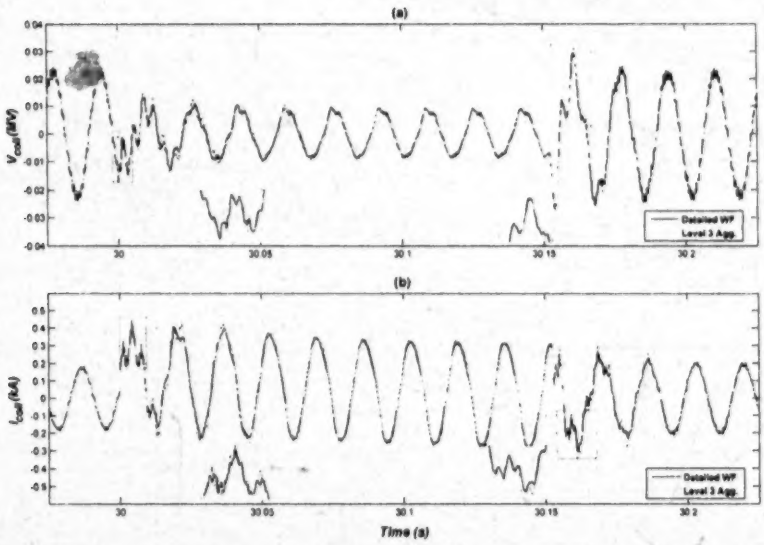

Figure 5.44: Comparisons of the collector bus: phase-*a* (a) voltage; and (b) current, during two-line-to-ground fault generated by the detailed and Level Three Aggregation model

Table 5.3: Off-line execution times and errors associated with different levels of aggregation

Model	No. of WTGSs	Rating(s) (MVA)	T_{avg} (s)	ε_P (%)	ε_Q (%)
Detailed	10	1.67	10022.0	–	–
Level One	4	3.34 & 5.01	5542.0	0.92	3.70
Level Two	2	8.35	3330.7	2.42	6.04
Level Three	1	16.70	1942.1	8.07	8.15

most suitable candidate for real-time studies of the wind farm interacting with variable wind speed, and single-line-to-ground and two-line-to-ground faults.

Because the Level Three Aggregation model resembled a single grid-connected WTGS, the amount of resources required for real-time simulation was the lowest among the three aggregation models. Considering the amount of time needed to develop, compile, and finally run the simulation in real-time, the Level Three Aggregation model is highly recommended for timely variable wind speed studies.

Table 5.4: RT execution times for individual tasks within one time-step

Model	No. of *node*(s)	T_s (μs)	T_{RT} (μs)	T_{com} (μs)
Detailed	4	53.278	42.758	33.901
Level One	3	50.000	28.822	15.477
Level Two	1	50.000	30.853	–
Level Three	1	50.000	17.953	–

5.6 Summary

First, a single WTGS and transmission system model was setup to verify the performance of the complete DFIG-based WTGS model developed through the previous chapters. From the case studies, the complete WTGS model has demonstrated its capability to generate under varying wind conditions while riding through different kinds of grid faults. Then, the complete WTGS was used to construct a grid-connected wind farm for the study of aggregation. Three different levels of aggregation models were developed to increase the efficiency of wind farm studies in off-line and real-time simulations.

6

Conclusions and Future Work

The wind farm aggregation techniques developed in this thesis were the product of different levels of wind energy system studies. First, the fundamental theories and designs of a DFIG-based WTGS were explored. After applying the properly designed control systems, the complete WTGS model underwent a series of off-line and real-time verifications as well as various interactive studies. Then, the validated WTGS model was employed for the construction of a wind farm, which formed the reference for the final aggregation study. The milestones and inspirations for future studies stemmed from this research are collectively presented in the following sections.

6.1 Contributions

Contributions from the thesis can be separated into two main sections concerning:

1. Development of a generalized DFIG-based WTGS model; and

2. Application of the verified WTGS model for RT wind farm studies.

Since the WTGS is consisted of many complex mechanical and electrical components, the model development and verifications were systematically divided into three stages. In stage one:

- the complex DFIG-based WTGS was logically divided into three sub-models: aerodynamic, mechanical, and electrical. Interactions between and functionalities within the sub-models were clearly defined.
- the highly efficient mathematical formulation describing the energy exchange across the wind turbine was verified.
- an alternative curve-fitting technique were presented for extrapolating the wind turbine power coefficient curves.
- detailed mathematical equations and their implementations for the multi-mass mechanical model were presented.
- in-depth analysis of the WRIM model were included to aid the discussions on the model reductions and parameter determinations.
- custom power electronic switch models were proposed for solving the technical problems associated with certain EMTP-type software packages.

In the second stage:

- mechanical and electrical control principles and the collaborations between the two controllers were clarified. The measurements required and the commands discharged from each controller were specifically identified.
- the commanding role of the mechanical controller was ascertained to rectify the confusions regarding the controller hierarchy.
- the entire electrical controller was designed and modeled from the ground up. To endorse better understanding of the design, the vector control theory, PI controller operation, and PWM generation were briefly discussed. Explicit demonstrations were given on how to employ the conventional root-locus method for fine-tuning the critical electrical responses.

In the final stage:

- the models and controller developed in the previous stages were methodically validated using three commercial software simulation packages: PSCAD™/EMTDC™, MATLAB®/SIMULINK®, and EMTP-RV.
- step-by-step construction of the complete DFIG model was demonstrated. By going through various software testings, the configuration was finalized as the reference model.
- the techniques for the model complexity measurements were explored under MATLAB®/SIMULINK®. By applying the given techniques, merits of the DFIG model optimization, reduction, and aggregation were better perceived.
- a modified Trapezoidal integration method was developed to resolve the algebraic-loop that hampered the performance of MATLAB®/SIMULINK®. This solution was essentially based on the conventional pole-zero compensation in discrete-time domain.
- the credibility of a switching function model, TSB, was confirmed, and the model was used to replace the SPS power electronic converter model resulting in substantial gains in simulation performance. This was the monumental step that led to the realization of simulating the WTGS in real-time.
- exhaustive analysis was performed to define the optimal techniques for improving the off-line and real-time simulation performances of the DFIG model.

After identifying the fundamental theories and verifying different techniques for the DFIG-based WTGS model development, spectrum of the research was expanded to applying the developed model in wind energy integration studies:

- a grid-connected single WTGS schematic was setup for studying the responses with variable wind speed and grid faults. By complying the

studies with the emerging operation standards, valuable insights was provided for actual controller development and coordinations.

- comprehensive demonstrations of off-line and real-time wind farm modeling and simulation were given. The main focus was on how to preserve the dynamic characteristics of the wind farm by effectively utilizing the physical and electrical properties.

- a model separation technique based the discrete Bergeron transmission line model was examined for the real-time simulation of large power systems.

- finally, three aggregation models were proposed for lightening the computational burden and achieving higher scalability on wind farm simulation studies.

6.2 Suggestions for Future Research

From this thesis, a solid foundation was established for the future research studies in the wind energy sector. Prospective research opportunities discovered during the study were identified below:

- a more well rounded converter bridge model replacement is needed. Although the switching function model was efficient, its limitations prevented the proper modeling of the hardware protective device for the BBC.

- bench mark models for the DFIG-based WTGSs should be developed. This could be a difficult task since there are many different manufacturers producing variable-speed WTGS using various proprietary technologies. However, common performance guideline should be reached to authenticate the simulation studies.

- applications of the modern control theories should be explored. Adaptive or self-adjusting control would be especially beneficial for the development of

centralized wind farm controller, which adjust the generation depending on the grid conditions.

- further studies on the fault ride-through control should be conducted. To comply with the emerging regulations protecting the interest of general public, the wind facilities must be properly controlled during and after the common transmission faults.

- with the existing wind farm model, centralized control algorithms can be developed. Controllers local to the individual WTGSs should be supervised by this centralized control to meet different operation requirements imposed for the entire wind farm.

- more systematic procedure for wind farm aggregation is essential for practical application of the techniques. Eventually, the procedures would be implemented in computer aided systems for automatic aggregation of a huge wind farm in real-time.

Bibliography

[1] M. Ahlstrom, L. Jones, R. Zavadil, and W. Grant, "The Future of Wind Forecasting and Utility Operations", *IEEE Power&Energy Magazine,* Vol. 3, No. 6 Nov./Dec. 2005, pp. 57-64.

[2] R. Zavadil, N. Miller, A. Ellis, and E. Muljadi, "Making Connections", *IEEE Power&Energy Magazine,* Vol. 3, No. 6 Nov./Dec. 2005, pp. 26-37.

[3] P. B. Eriksen, T. Ackermann, H. Abildgaard, P. Smith, W. Winter, and J. R. Garcáa, "System Operation with High Wind Penetration", *IEEE Power&Energy Magazine,* Vol. 3, No. 6 Nov./Dec. 2005, pp. 65-75.

[4] R. Piwko, D. Osborn, R. Gramlich, G. Jordan, D. Hawkins, and K. Porter, "Wind Energy Delivery Issues", *IEEE Power&Energy Magazine,* Vol. 3, No. 6 Nov./Dec. 2005, pp. 47-56.

[5] J. C. Smith, "Wind of Change: Issues in Utility Wind Integration", *IEEE Power&Energy Magazine,* Vol. 3, No. 6 Nov./Dec. 2005, pp. 20-25.

[6] J. Ekanauake, L. Holdsworth, and N. Jenkins "Control of DFIG Wind Turbines", *IEEE Power Engineer,* Vol. 17, Feb. 2003, pp. 28-32.

[7] D. A. Bechrakis and P. D. Sparis "Correlation of Wind Speed Between Neighboring Measureing Stations", *IEEE Transactions on Energy Conversion,* Vol. 19, No. 2, June 2004, pp. 400-406.

[8] Å. Larsson, "Flicker Emission of Wind Turbines Caused by Switching Operations", *IEEE Transactions on Energy Conversion*, Vol. 17, No. 1, Mar. 2002, pp. 119-123.

[9] Å. Larsson, "Flicker Emission of Wind Turbines During Continuous Operations", *IEEE Transactions on Energy Conversion*, Vol. 17, No. 1, Mar. 2002, pp. 114-118.

[10] C. Carrillo, A. E. Feijóo, J. Cidrás, and J. González, "Power Fluctuations in an Isolated Wind Plant", *IEEE Transactions on Energy Conversion*, Vol. 19, No. 1, Mar. 2004, pp. 217-221.

[11] D. S. Zinger, E. Muljadi, "Annualized Wind Energy Improvement Using Variable Speeds", *IEEE Transactions on Industry Applications*, Vol. 33, No. 6, pp. 1444-1447, Nove.-Dec. 1997.

[12] R. Datta, and V. T. Ranganathan, "Varialbe-Speed Wind Power Generation Using Doubly Fed Wound Rotor Induction Machine-A Comparison With Alternative Schemes", *IEEE Transactions on Energy Conversion*, Vol. 17, No. 3, Sept. 2002, pp. 414-420.

[13] S. Heier, *Grid Intergration of Wind Energy Coversion Systems*, Chincester, UK: John Wiley & Sons Ltd., 1998

[14] J. M. Rodríguez, J. L Fernández, D. Beato, R. Iturbe, J. Usaola, P. Ledesma, and J. R. Wilhelmi, "Incidence on Power System Dynamics of High Penetration of Fixed Speed and Doubly Fed Wind Energy Systems: Study of the Spanish Case", *IEEE Transactions on Power Systems*, Vol. 17, No. 4, Nov. 2002, pp. 1089-1095.

[15] P. Pourbeik, *Integration of Wind Energy into the Alberta Electric System Stages 2 & 3: Planning and Interconnection Criteria* Electric Systems Consulting ABB Inc., Report Number: 2004-10803-2.R01.4, Dec. 2003

[16] G. S. Stavrakis, and G. N. Kariniotakis, "General Simulation Algorithm for the Accurate Assessment of Isolated Diesel - Wind Turbines System Interaction.

Part I: A General Multimachine Power System Model", *IEEE Transactions on Energy Conversion*, Vol. 10, No. 3, Spet. 1995, pp. 577-583.

[17] R. Chedid, N. LaWhite, and M. Llic, "Simulating Dynamic Interactions of Grid-Linked Wind Turbines", *IEEE Computer Applications in Power* Vol. 7, Issue: 4, 1994, pp. 46-49

[18] R. Chedid, F. Mrad, and M. Basma, "Intelligent Control of a Class of Wind Energy Conversion System", *IEEE Transactions on Energy Conversion*, Vol. 14, No. 4, Dec. 1999, pp. 1597-1604.

[19] A. D. Hansen, P. Sorensen, L. Janosi, and J. Bech, "Wind Farm Modelling for Power Quality", *IEEE The 27th Annual Conference of the Industrial Electronics Society, 2001. IECON '01.* Vol. 3, 29 Nov.-2 Dec. 2001, pp. 1959 - 1964

[20] J. L. R. Amenedo, S. Arnalte, and J. C. Burgos, "Automatic Generation Control of a Wind Farm With Variable Speed Wind Turbines", *IEEE Transactions on Energy Conversion*, Vol. 17, No. 2, June 2002, pp. 279-284.

[21] J. G. Slootweg and W. L. Kling, "Modeling of Large Wind Farms in Power System Simulations", *IEEE Power Engineering Society Summer Meeting*, Vol. 1, 21-25 July 2002, pp. 503-508.

[22] R. J. Koessler, S. Pillutla, L. H. Trinh, and D. L. Dickmander, "Integration of Large Wind Farms into Utility Grids (Part 1 - Modeling of DFIG)", *Power Engineering Society General Meeting, 2003, IEEE* Vol. 3, 13-17 July 2003

[23] P. Pourbeik, R. J. Koessler, D. L. Dickmander, and W. Wong, "Integration of Large Wind Farms into Utility Grids (Part 2 - Performance Issues)", *Power Engineering Society General Meeting, 2003, IEEE* Vol. 3, 13-17 July 2003

[24] D. J. Trudnowski, A. Gentile, J. M Khan, E. M. Petritz, "Fixed-Speed Wind-Generator and Wind-Park Modeling for Transient Stability Studies", *IEEE Transactions on Power System*, Vol. 19, No. 4, Nov. 2004, pp. 1911-1917.

[25] S. K. Salman, A. L. J. Teo, "Windmill Modeling Consideration and Factors Influencing the Stability of a Grid-Connected Wind Power-Based Embedded Generator", *IEEE Transactions on Power System*, Vol. 18, No. 2, May 2003, pp. 793-802.

[26] J. G. Slootweg, S. W. H. de Haan, H. Polinder, W. L. Kling "Aggregated Modelling of Wind Parks With Variable Speed Wind Turbines in Power System Dynamics Simulations", *14th Power Systems Computation Conference, Sevilla, Spain*, 24-28, June 2002.

[27] W. Lu, B. T. Ooi, "Optimal Acquisition and Aggregation of Offshore Wind Power by Multiterminal Voltage-Source HVDC", *IEEE Transactions on Power Delivery*, Vol. 18, No. 1, Jan. 2003, pp. 201-206.

[28] S. J. Haslam, P. A. Crossley, and N. Jenkins, "Design and Field Testing of a Source Based Protection Relay for Wind Farms", *IEEE Transactions on Power Delivery*, Vol. 14, No. 3, July 1999, pp. 818-823.

[29] C. Nichita, D. Luca, B. Dakyo, E. Ceanga, "Large Band Simulation of the Wind Speed for Real Time Wind Turbine Simulators", *IEEE Transactions on Energy Conversion*, Vol. 17, No. 4, Dec. 2002, pp. 523-529.

[30] M. G. Jovanović, R. E. Betz, J. Yu, "The Use of Doubly Fed Reluctance Machines for Large Pumps and Wind Turbines", *IEEE Transactions on Industry Applications*, Vol. 38, No. 6, Nov.-Dec. 2002, pp. 1508-1516.

[31] T. F. Chan, K. A. Nigim, L. L. Lai, "Voltage and Frequency Control of Self-Excited Slip-Ring Induction Generators", *IEEE Transactions on Energy Conversion*, Vol. 19, No. 1, Mar. 2004, pp. 81-86.

[32] H. M. Kojabadi, L. Chang, T. Boutot, "Development of a Novel Wind Turbine Simulator for Wind Energy Conversion Systems Using an Inverter-Controlled Induction Motor", *IEEE Transactions on Energy Conversion*, Vol. 19, No. 3, Sept. 2004, pp. 547-552.

[33] D. S. L. Dolan and P. W. Lehn, "Real-Time Wind Turbine Emulator Suitable for Powr Quality and Dynamic Contrl Studies", *IPST05International Conference on Power Systems Transients, Montreal, Canada* June 2005, pp. 2328.

[34] N. W. Miller, W. W. Price, J. J. Sanchez-Gasca, "Dynamic Modeling of GE 1.5 and 3.6 Wind Turbine-Generators", *GE-Power Systems Energy Consulting,* Version 3.0, Oct. 27th, 2003.

[35] P. Vas, *Vector Control of AC Machines,* New York: Oxfor Univ. Press, 1990

[36] O. Wasynczuk, D. T. Man, J. P. Sullivan, "Dynamic Behavior of a Class of Wind Turbine Generators During Random Wind Fluctuations", *IEEE Transactions on Power Apparatus and Systems,* Vol. 100, No. 6, Jun. 1981, pp. 2837-2845.

[37] P. M. Anderson, A. Bose, "Stability Simulation of Wind Turbine Systems", *IEEE Transactions on Power Apparatus and Systems,* Vol. 102, No. 12, Dec. 1983, pp. 3791-3794.

[38] R. Pena, J. C. Clare, G. M. Asher, "Doubly fed induction generator using back-to-back PWM converters and its application to variable-speed wind-energy generation", *IEE Proc.-Electr. Power Appl.*, Vol. 143, No. 3, May 1996, pp. 231-241.

[39] R. Pena, J. C. Clare, G.M. Asher, "A doubly fed induction generator using back-to-back PWM converters supplying an isolated load from a variable speed wind turbine", *IEE Proc.-Electr. Power Appl.,* Vol. 143, No. 5, Sept. 1996, pp. 380-387.

[40] S. A. Papathanassiou, M. P. Papadopoulos, "Dynamic Behavior of Variable Speed Wind Turbines under Stochastic Wind", *IEEE Transactions on Energy Conversion,* Vol. 14, No. 4, Dec. 1999, pp. 1617-1623.

[41] T. Petru, T. Thiringer, "Modeling of Wind Turbines for Power System Studies", *IEEE Transactions on Power Systems,* Vol. 17, No. 4, Nov. 2002, pp. 1132-1139.

[42] J. G. Slootweg, H. Polinder, W. L. Kling, "Representing Wind Turbine Electrical Generating Systems in Fundamental Frequency Simulations", *IEEE Transactions on Energy Conversion*, Vol. 18, No. 4, Nov. 2003, pp. 516-524.

[43] J. G. Slootweg, S. W. H. de Haan, H. Polinder, W. L. Kling, "General Model for Representing Variable Speed Wind Turbines in Power System Dynamics Simulations", *IEEE Transactions on Power Systems*, Vol. 18, No. 1, Feb. 2003, pp. 144-151.

[44] A. Tapia, G. Tapia, J. X. Ostolaza, J. R. Sáenz, "Modeling and Control of a Wind Turbine Driven Doubly Fed Induction Generator", *IEEE Transactions on Energy Conversion*, Vol. 18, No. 2, June 2003, pp. 194-204.

[45] D. Seyoum, C. Grantham, M. F. Rahman, "The Dynamic Characteristics of an Isolated Self-Excited Induction Generator Driven by a Wind Turbine", *IEEE Transactions on Industry Applications*, Vol. 39, No. 4, July-Aug. 2003, pp. 936-944.

[46] L. Mihet-Popa, F. Blaabjerg, I. Boldea, "Wind Turbine Generator Modeling and Simulation Where Rotational Speed is the Controlled Variable", *IEEE Transactions on Industry Applications*, Vol. 40, No. 1, Jan.-Feb. 2004, pp. 3-10.

[47] M. V. A. Nunes, J. A. P. Lopes, H. H. Zürn, U. H. Bezerra, R. G. Almeida, "Influence of the Variable-Speed Wind Generators in Transient Stability Margin of the Conventional Generators Integrated in Electrical Grids", *IEEE Transactions on Energy Conversion*, Vol. 19, No. 4, Dec. 2004, pp. 692-701.

[48] C. M. Ong, *Dynamic Simulation of Electric Machinery: Using Matlab/Simulink*, Prentice Hall, 1997

[49] B. K. Bose , *Modern Power Electronics and AC Drives*, Prentice Hall, 2001)

[50] G. J. Rogers, D. Shirmohammadi, "Induction Machine Modeling for Electromagnetic Transient Program", *IEEE Transactions on Energy Conversion*, Vol. 2, No. 4, Dec. 1987, pp. 1156-1165.

[51] S. R. Sanders, J. Mark Noworolski, Xiaojun Z. Liu, George C . Verghese, "Generalized Averaging Method for Power Conversion Circuits", *IEEE Transactions on Power Electronics*, Vol. 6, No. 2, Apr. 1991, pp. 251-259.

[52] H. S. Chikwanda, H. R. Bolton, "Analysis of the naturally commutated, convertor-fed induction motor drive system using a flux vector method", *IEE PROCEEDINGS-B*, Vol. 140, No. 6, Nov. 1993, pp. 401-415.

[53] L. Salazar, G. Joós, "PSPICE Simulation of Three-phase Inverters by Means of Switching Functions", *IEEE Transactions on Power Electronics*, Vol. 9, No. 1, Jan. 1994, pp. 35-42.

[54] K. S. Tam, L. Yang, "Functional Models for Space Power Electronic Circuits", *IEEE Transactions on Aerospace and Electronic Systems*, Vol. 31, No. 1, Jan. 1995, pp. 288-296.

[55] J. Sun, H. Grotstollen, "Symbolic Analysis Methods for Averaged Modeling of Switching Power Converters", *IEEE Transactions on Power Electronics*, Vol. 48, No. 2, Jan.-Feb. 1997, pp. 537-546.

[56] B. K. Lee, M. Ehsani, "A Simplified Functional Simulation Model for Three-Phase Voltage-Source Inverter Using Switching Function Concept", *IEEE Transactions on Industrial Electronics*, Vol. 48, No. 2, Jan.-Feb. 2001, pp. 309-321.

[57] A. Emadi, "Modeling of Power Electronic Loads in AC Distribution Systems Using the Generalized State-Space Averaging Method", *IEEE Transactions on Industrial Electronics*, Vol. 51, No. 5, Jan.-Feb. 2004, pp. 992-1000.

[58] G. R. Slemon, "Modelling of Induction Machines for Electric Drives", *IEEE Transactions on Industry Application*, Vol. 25, No. 6, Nov.-Dec. 1989, pp. 1126-1131.

[59] T. Thiringer, J. Luomi, "Comparison of Reduced-Order Dynamic Models of Induction Machines", *IEEE Transactions on Power Systems*, Vol. 16, No. 1, Feb. 2001, pp. 119-126.

[60] A. Miller, E. Muljadi, D. S. Zinger "A Variable Speed Wind Turbine Power Control", *IEEE Transactions on Energy Conversion*, Vol. 12, No. 2, June 1997, pp. 181-186.

[61] A. D. Hansen, F. Iov, P. S.ørensen, F. Blaabjerg "Overall control strategy of variable speed doubly-fed induction generator wind turbine", *Nordic Wind Power Conference, Chalmers University of Technology*, 1-2 March, 2004

[62] S. J. Chapman, *Electric Machinery Fundamentals*, McGraw-Hill, 1990

[63] C. Schauder, H. Mehta, "Vector analysis and control of advanced static VAR compensators", *IEE Proc.- C Generation, Transmission and Distribution*, Vol. 140, No. 4, Jul. 1993, pp. 299-306.

[64] R. C. Dorf, R. H. Bishop, *Modern Control Systems*, Prentice Hall, 2001

[65] J. Holtz, "Pulsewidth Modulation - A Survey", *IEEE Transactions on Industrial Electronics*, Vol. 39, No. 5, Oct. 1992, pp. 410-420.

[66] K. Zhou, D. Wang, "Relationship Between Space-Vector Modulation and Three-Phase Carrier-Based PWM: A Comprehensive Analysis", *IEEE Transactions on Industrial Electronics*, Vol. 49, No. 1, Feb. 2002, pp. 186-195.

[67] V. R. Dinavahi, M. Reza Iravani, R. Bonert, "Real-time digital simulation of power electronic apparatus interfaced with digital controllers", *IEEE Transactions on Power Delivery*, Vol. 16, No. 4, June 2001, pp. 775-781.

[68] V. Blasko, V. Kaura, "A New Mathematical Model and Control of a Three-Phase AC-DC Voltage Source Converter", *IEEE Transactions on Power Electronics*, Vol. 12, No. 1, Jan. 1997, pp. 116-123.

[69] J. A. Hollman, J. R. Marti, "Real time network simulation with PC-cluster", *IEEE Transactions on Power Systems*, Vol. 18, No. 2, May 2003, pp. 563-569.

[70] R. Champagne, L .A. Dessaint, H. Fortin-Blanchette, G. Sybille, "Analysis and Validation of a Real-Time AC Drive Simulator", *IEEE Transactions on Power Electronics*, Vol. 19, No. 2, Mar. 2004, pp. 336-345.

[71] L. Pak, M. O. Faruque, X. Nie, V. Dinavahi, "A Versatile Cluster-Based Real-Time Digital Simulator for Power Engineering Research", *submitted to IEEE Transactions on Power Systems*,

[72] O. Anaya-Lara and E. Acha, "Modeling and Analysis of Custom Power Systems by PSCAD/EMTDC", *IEEE Transactions on Power Delivery*, Vol. 17, No. 1, Jan. 2002, pp. 266-270.

[73] C. K. Sao, P. W. Lehn, M. R. Iravani, and J. A. Martinez, "A Benchmark System for Digital Time-Domain Simulation of a Pulse-Width-Modulated D-STATCOM", *IEEE Transactions on Power Delivery*, Vol. 17, No. 4, Oct. 2002, pp. 1113-1120.

[74] M. O. Faruque, V. Dinavahi, Wilsun Xu, "Algorithms for the accounting of multiple switching events in digital simulation of power-electronic systems", *IEEE Transactions on Power Delivery*, Vol. 20, No. 2, Jan. 2005, pp. 1157-1167.

[75] A. M. Gole, I. T. Fernando, G. D. Irwin, O. B. Nayak, "Modeling of power electronic apparatus: Additional interpolation issues", *IPST97International Conference on Power Systems Transients, Seattle*, June 1997, pp. 2328.

[76] J. R. Marti, S. Acevedo, L. R. Linares, H. W. Dommel, "Accurate solution of HVDC converters in real-time transients simulation", *IPST97International Conference on Power Systems Transients, Seattle*, June 1997, pp. 455459.

[77] E. A. DeMeo, W. Grant, M. R. Milligan, and M. J. Schuerger, "Wind Plant Integration: Costs, Status, and Issues", *IEEE Power&Energy Magazine*, Vol. 3, No. 6 Nov./Dec. 2005, pp. 38-46.

[78] N. Mohan, T. M. Undeland, and W. P. Robbins, *Power Electronics: Converters, Applications, and Design*, Canada: John Wiley & Sons, Inc., 1995

[79] G. Saccomando, J. Svensson, A. Sannino, "Improving Voltage Disturbance Rejection for Variable-Speed Wind Trubine", *IEEE Transactions on Energy Conversion*, Vol. 17, No. 3, Sept. 2002, pp. 422-428.

[80] J. D. Glover and M. S. Sarma, *Power System Analysis and Design*, California: Wadsworth Group, 2002

A

Coefficients for $C_p(\theta, \lambda)$ Curve Fitting

Table A.1: Coefficients for $C_p(\theta, \lambda)$ Curve Fitting

i	j	a_{ij}
4	4	4.9686e-010
4	3	-7.1535e-008
4	2	1.6167e-006
4	1	-9.4839e-006
4	0	1.4787e-005
3	4	-8.919e-008
3	3	5.9924e-006
3	2	-1.0479e-004
3	1	5.7051e-040
3	0	-8.6018e-004
2	4	2.7937e-006
2	3	-1.4855e-004
2	2	2.1495e-003
2	1	-1.0996e-002
2	0	1.5727e-002
1	4	-2.3895e-005
1	3	1.0683e-003
1	2	-1.3934e-002
1	1	6.0405e-002
1	0	-6.7606e-002
0	4	1.1524e-005
0	3	-1.3365e-004
0	2	-1.2406e-002
0	1	2.1808e-001
0	0	-4.1909e-001

B

MATLAB-code for $C_p(\theta, \lambda)$ Curve Fitting

B.1 Cp.m

```
%By:   Pak, Lok-Fu
%Date: Sept. 17, 05
%-------------------------------------------------------------------------
% This MATLAB program generates the Cp(theta, lamda) curves

clear;

load Cp_al.txt;
al = Cp_al;      % load given alpha coefficient from Cp_al.txt file

theta_cp = [0 1 3 5 7 9 11 13 15 17 19]; % pitch angel of the turbine blade
lambda_cp = (0:1:20);                    % tip speed ratio

% intialize power coefficient
C_p = zeros(length(theta_cp), length(lambda_cp));

temp = 0;
temp2= 0;
temp3= 0;

for count = 1:length(theta_cp)
    for count2 = 1:length(lambda_cp)
        for i = 1:5
            for j = 1:5
            temp=al(i,j)*(theta_cp(count)^(i-1))*(lambda_cp(count2)^(j-1));
            temp2= temp2 + temp;

            temp = 0;
            end;
            temp3 = temp3 + temp2;
            temp2 = 0;
        end;
        C_p(count,count2) = temp3;
        temp3 = 0;
    end;
end;

subplot(2,2,1)
plot(lambda_cp, C_p)
title('\itCp\rm(\theta, \lambda) vs. \lambda curves')
xlabel('\lambda')
ylabel('\itCp\rm(\theta, \lambda)')
axis([0 20 0 0.6])

subplot(2,2,2)
plot(lambda_cp, C_p(1,:))
title('\itCp\rm(\theta, \lambda) vs. \lambda curve (with \theta = 0\circ)')
xlabel('\lambda')
ylabel('\itCp\rm(\theta, \lambda)')
axis([0 20 0 0.6])

%-------------------------------------------------------------------------
% The power vs. turbine rational speed curves
% ---constants---
xresol = 0.1;
w_range= 3.5;

%----------------

con = 0.00159;  % p/2*Ar
K_b = 35.25;    % turbine blade radius

v_w = [4.82:0.5:12];      % wind speed
w_g = [0:xresol:w_range]; % generator rotational speed

P = zeros(length(v_w), length(w_g));

for count3 = 1:length(v_w)

    for count4 = 1:length(w_g)

        lam = K_b * w_g(count4) / v_w(count3);

        % Forth order approximation
        Ccp=1.2e-5*(lam^4)-0.00013*(lam^3)-0.012*(lam^2)+0.22*lam-0.42;

        % Third order approximation
        % Ccp = 0.00033 * lam^3 - 0.018 * lam^2 + 0.24 * lam -0.44;

        P(count3, count4) = con * (v_w(count3)^3) * Ccp;
    end;
end;

% finding the max point curve
[control,index] = max(P');
c_curve = zeros(1,length(index));

for count5 = 1:length(index)
    c_curve(count5) = w_g(index(count5));
end;

subplot(2,2,3)
plot(w_g*30/pi, P, 'b')
title('Power vs. Turbine Rational Speed curves')
xlabel('\warpi_{\itturbine} (rpm)')
ylabel('\itPower \rm(p.u.)')
hold on;
plot(c_curve * 30 /pi, control, '-.r')
axis([0 max(w_g)*30/pi 0 1.5])
hold off;

% The control curve (P(p.u.) vs. w_turbine(rpm) )
x = [0:0.01:max(w_g)*30/pi];
y = 6e-5 * (x.^3) - 2.6e-5 * (x.^2) - 0.0023 *x + 0.021;

for count6 = 1:length(y)
    if y(count6) < 0.1
        y(count6) = 0;
    elseif y(count6) > 1
        y(count6) = 1;
    end;
end;

subplot(2,2,4)
plot(x, y)
title('Power vs. Turbine Rational Speed control curve')
xlabel('\warpi_{\itturbine} (rpm)')
ylabel('\itPower \rm(p.u.)')
hold on;

% setting the power limitations
lim     = zeros(3,length(x));
lim(1,:) = 1;
lim(2,:) = 0.1;
lim(3,:) = 0.55;
plot(x, lim,':r')
axis([0 max(w_g)*30/pi 0 1.5])
hold off;

% The control curve (P(p.u.) vs. v_w(m/s) )
xv = [0:0.01:25];
yv = (xv.^3) * 0.00091 + 0.00013 * (xv.^2) - 0.001 * xv + 0.0025;

for count6 = 1:length(yv)
    if yv(count6) < 0.1
        yv(count6) = 0;
    elseif yv(count6) > 1
        yv(count6) = 1;
    end;
end;
```

C

Variables for Mechanical Control

Table C.1: Wind Power Coefficients

Parameter Name	Recommended Value
K_{pp}	150.00
K_{ip}	25.00
T_p (second)	0.01
θ_{max} (degree)	27.00
θ_{min} (degree)	0.00
$d\theta/dt_{max}$ (degrees/second)	10.00
$d\theta/dt_{min}$ (degrees/second)	-10.00
P_{max} (pu)	1.00
P_{min} (pu)	0.10
dP/dt_{max} (pu/second)	0.45
dP/dt_{min} (pu/second)	-0.45
K_{pc}	3.00
K_{ic}	30.00
K_{ptrq}	3.00
K_{itrq}	0.60
T_{pc}	0.05

D

MATLAB-code for Rotor-side Converter Controller Design

D.1 PI_inner_con1.m

```
%By:   Pak, Lok-Fu
%Date: Sept. 17, 05
%-------------------------------------------------------------------
%This MATLAB program is used for rotor-side converter controller design.
%The target is the inner-loop current controlling PI controller.

clear;

Ts = 50e-6; %The sample time for s- to z-domain transformation

Zb = 575^2/1.67e6; %Base impedance
Lb = Zb/(60*2*pi); %Base inductance

Rr = 0.0100649 * Zb; %Rotor resistance in SI unit
Lm = 3.47857 * Lb;   %Mutual inductance in SI
Ls = 0.0998644 * Lb + Lm;
Lr = 0.0998644 * Lb + Lm; %Rotor inductance in SI

%The 0.005 indicate the extra filtering inductance L_{fr}
Lrp = Lr - (Lm^2/Ls) + 0.005;

%Machine rotor model parameters
A = exp(-Rr/Lrp*Ts);
kp = (1 - A)/Rr;

%inner-loop PI controller parameters
kc = 0.8799;
ac =0.996591;

%System transfer function
Gpi = tf([1 -ac], [1 -1], Ts);
Ginver = tf(1, [1 0 0], Ts);
Gplant = tf( kp, [1 -A], Ts);
sys = Gpi * Ginver * Gplant;

%Root-locus
axis square;
rlocus(sys);
figure;
axis square;
rlocus(sys);
axis([0.992 1.001 -4e-3 4e-3])
%rlocfind(sys);

%PI controller tf in s-domain
Gc = d2c(kc*Gpi,'tustin')

%Step response
figure;
axis square;
step(feedback(Gc,1),1);
axis([0 1 0 1.2])
```

D.2 PI_outter_con1.m

```
%By:   Pak, Lok-Fu
%Date: Sept. 17, 05
%-------------------------------------------------------------------
%This MATLAB program is used for rotor-side converter controller design.
%The target is the outer-loop power controlling PI controller.

clear;

Ts = 50e-6; %The sample time for s- to z-domain transformation

Zb = 575^2/1.67e6;
Lb = Zb/(60*2*pi);

Rr = 0.0100649 * Zb;
Lm = 3.47857 * Lb;
Ls = 0.0998644 * Lb + Lm;
Lr = 0.0998644 * Lb + Lm;

%The 0.005 indicate the extra filtering inductance
Lrp = Lr - (Lm^2/Ls) + 0.005;

%Machine rotor model parameters
A = exp(-Rr/Lrp*Ts);
kp = (1 - A)/Rr;

%inner-loop PI controller parameters
kc = 0.8799;
ac = 0.996591;

%outer-loop PI controller parameters
kc2 = 1.898;
ac2 = 0.997893;

%System transfer function
Gpi2 = tf([1 -ac2], [1 -1], Ts);
Gpi = kc*tf([1 -ac], [1 -1], Ts);
Ginver = tf(1, [1 0 0], Ts);
Gplant = tf( kp, [1 -A], Ts);
sys = Gpi2 * Gpi * Ginver * Gplant;

%Root-locus
axis square
rlocus(sys);
axis([-2 2 -2 2])
figure;
axis square
rlocus(sys);
axis([0.989 1.001 -5e-3 5e-3])
%rlocfind(sys);
figure;

%PI controller tf in s-domain
Gc = d2c(Gpi,'tustin')
Gc2 = d2c(kc2*Gpi2,'tustin')

%Step response
axis square
step(feedback(Gc2,1),1);
axis([0 1 0 1.2])
```

E

MATLAB-code for Grid-side Converter Controller Design

E.1 PI_inner_con2.m

```
%By:   Pak, Lok-Fu
%Date: Sept. 17, 05
%-------------------------------------------------------------------------
%This MATLAB program is used for grid-side converter controller design.
%The target is the inner-loop current controlling PI controller.

clear;

Ts = 50e-6; %The sample time for s- to z-domain transformation

%AC-supply side parameters
R = 0.005;
L = 0.001;

%AC-side model parameters
A = exp(-R/L*Ts);
kp = (1 - A)/R;

%PI controller parameters
kc = 4.171;
ac = 0.994006;

%System tf
Gpi = tf([1 -ac], [1 -1], Ts);
Ginver = tf(1, [1 0 0], Ts);
Gplant = tf( kp, [1 -A], Ts)
sys = Gpi * Ginver * Gplant;

%Root-locus
axis square
rlocus(sys);
figure;
axis square
rlocus(sys);
axis([0.987 1.001 -6e-3 6e-3])
%rlocfind(sys);

figure;

%PI controller tf in s-domain
Gc = d2c(kc*Gpi,'tustin')

%Step Response
axis square
% cL = feedback(kc*sys, 1);
step(feedback(Gc,1),1);
axis([0 1 0 1.2])
```

E.2 PI_outter_con2.m

```
%By:   Pak, Lok-Fu
%Date: Sept. 17, 05
%-------------------------------------------------------------------------
%This MATLAB program is used for grid-side converter controller design.
%The target is the outter-loop current controlling PI controller.

clear;

%Ts = 50e-6;

%system parameters
R = 0.1;
L = 0.001;
C = 25000e-6;

% A = exp(-R/L*Ts);
% kp = (1 - A)/R;

%PI controller gains
kc2 = 1.25;
ac2 = 200;

%system tf
Gpi = tf([1 ac2], [1 0]);
Gain = 3*0.75/(2*sqrt(2));
Gplant = tf( 1, [C 0]);
sys = Gpi * Gain * Gplant;

%Root-locus
rlocus(sys);
axis([-450 100 -300 300])
%rlocfind(sys);
figure;

%Step response
axis square
cL = feedback(kc2*sys, 1);
step(cL,1);

%PI controller tf
Gc = kc2*Gpi
```

F

Induction Machine Starting Schematics

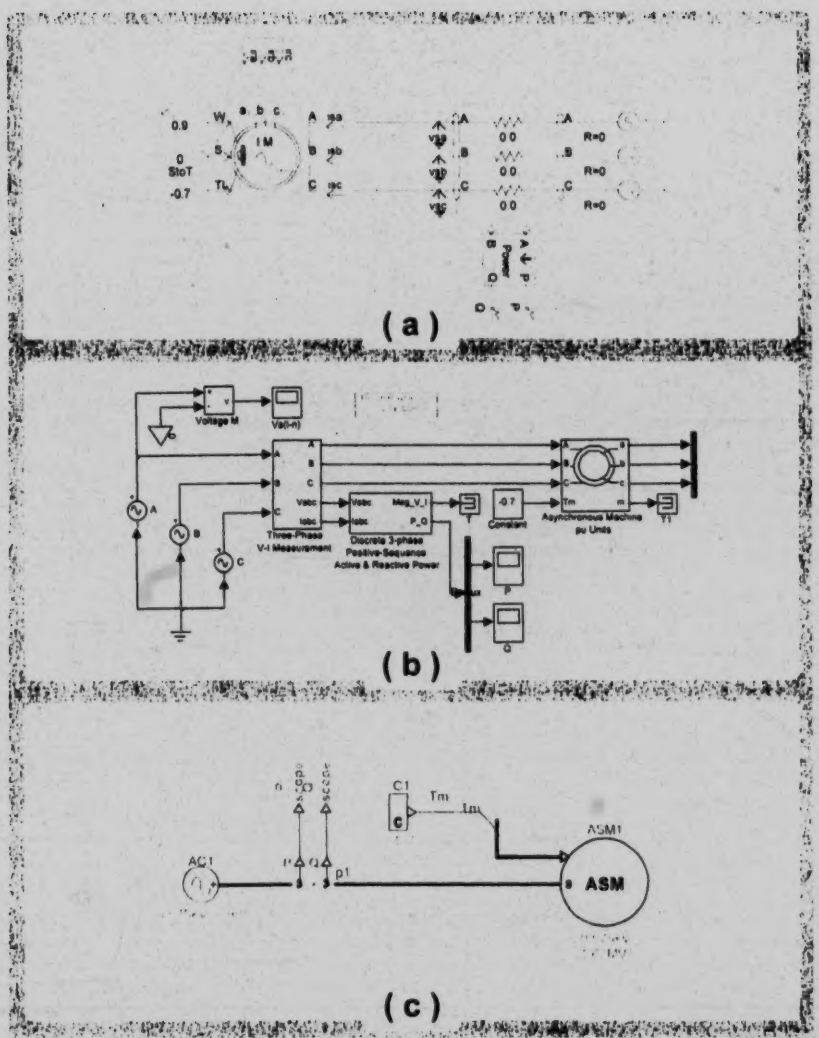

Figure F.1: Induction Machine Starting Schematics Implemented in: (a) PSCAD/EMTDC V.4.0; (b) MATLAB/SIMULINK V.7.0.1; (c) EMTP-RV V1.1

G

DC Capacitor Charging Schematics Implementations

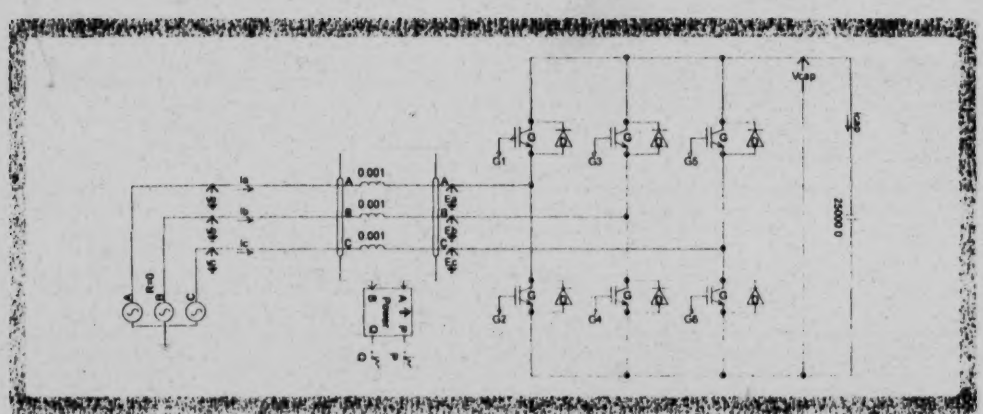

Figure G.1: DC Capacitor Charging Electrical Schematics Implemented in PSCAD/EMTDC V.4.0

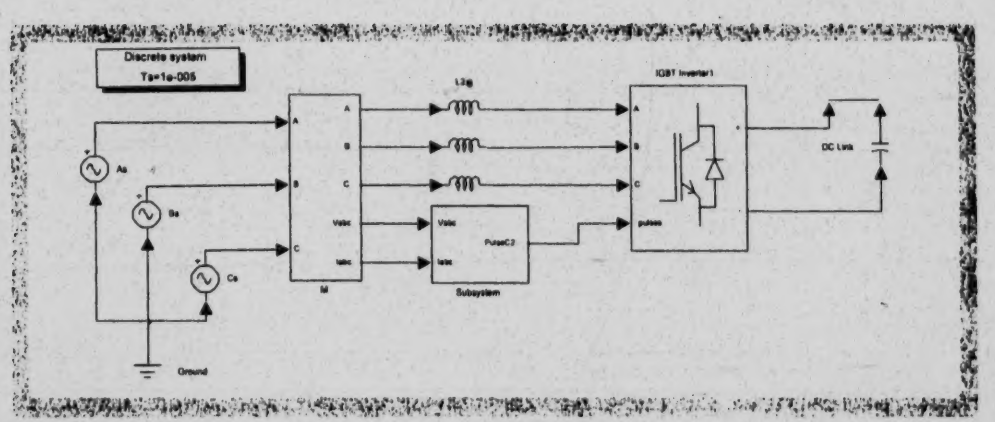

Figure G.2: DC Capacitor Charging Electrical Schematics Implemented in MATLAB/SIMULINK V.7.0.1

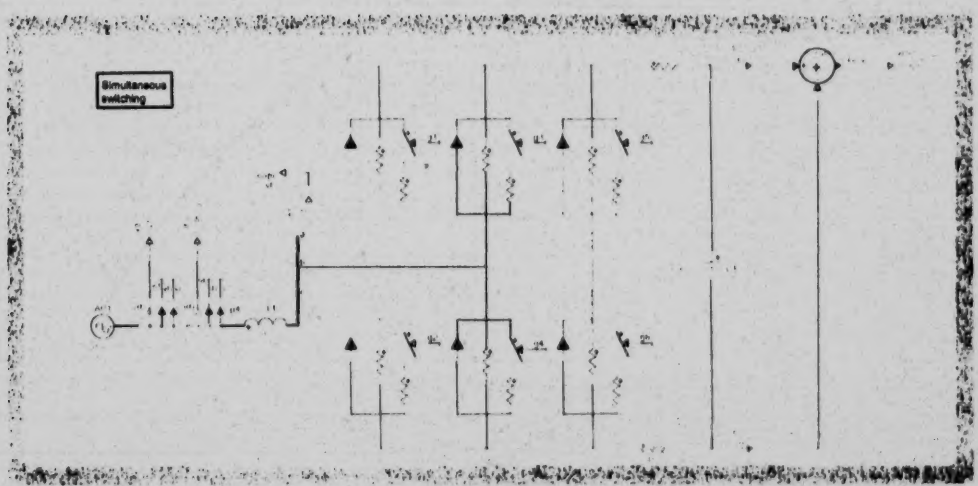

Figure G.3: DC Capacitor Charging Electrical Schematics Implemented in EMTP-RV V1.1

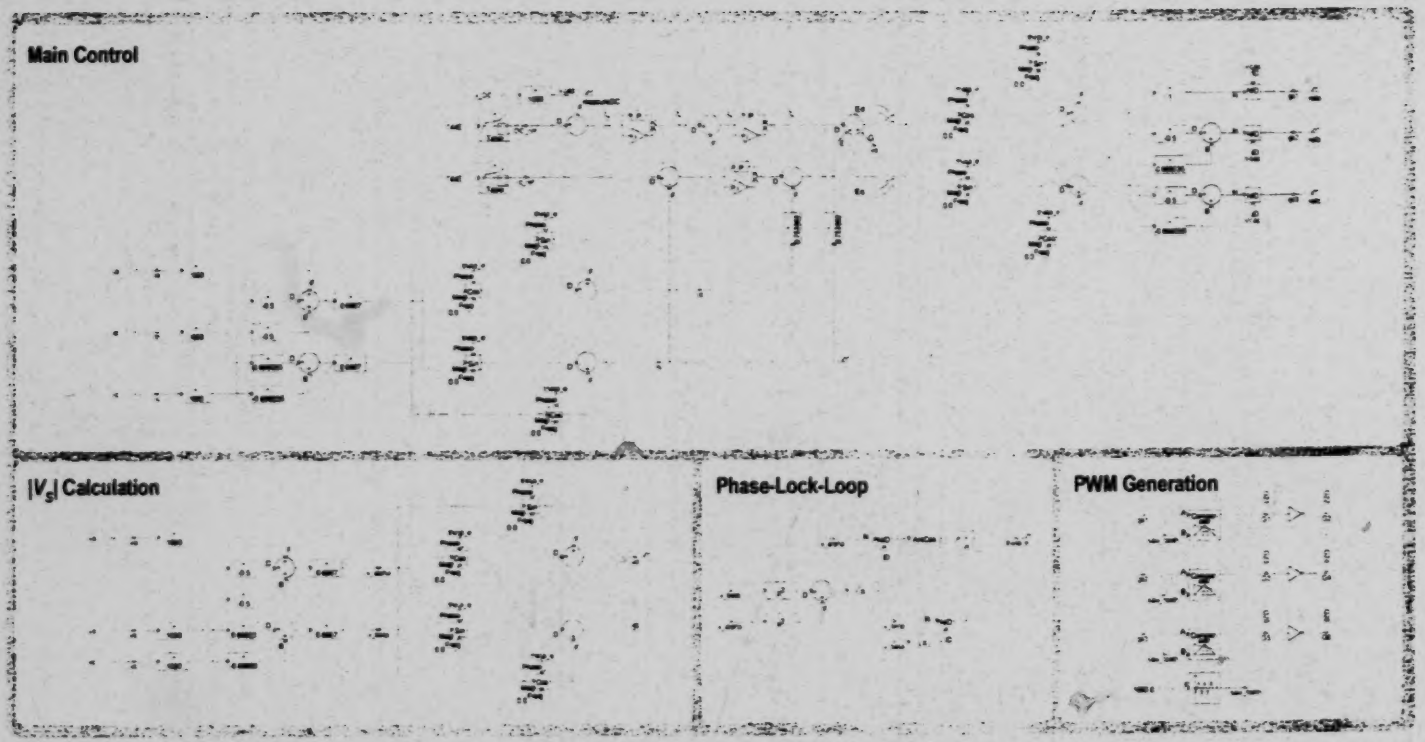

Figure G.4: DC Capacitor Charging Control Schematics Implemented in PSCAD/EMTDC V.4.0

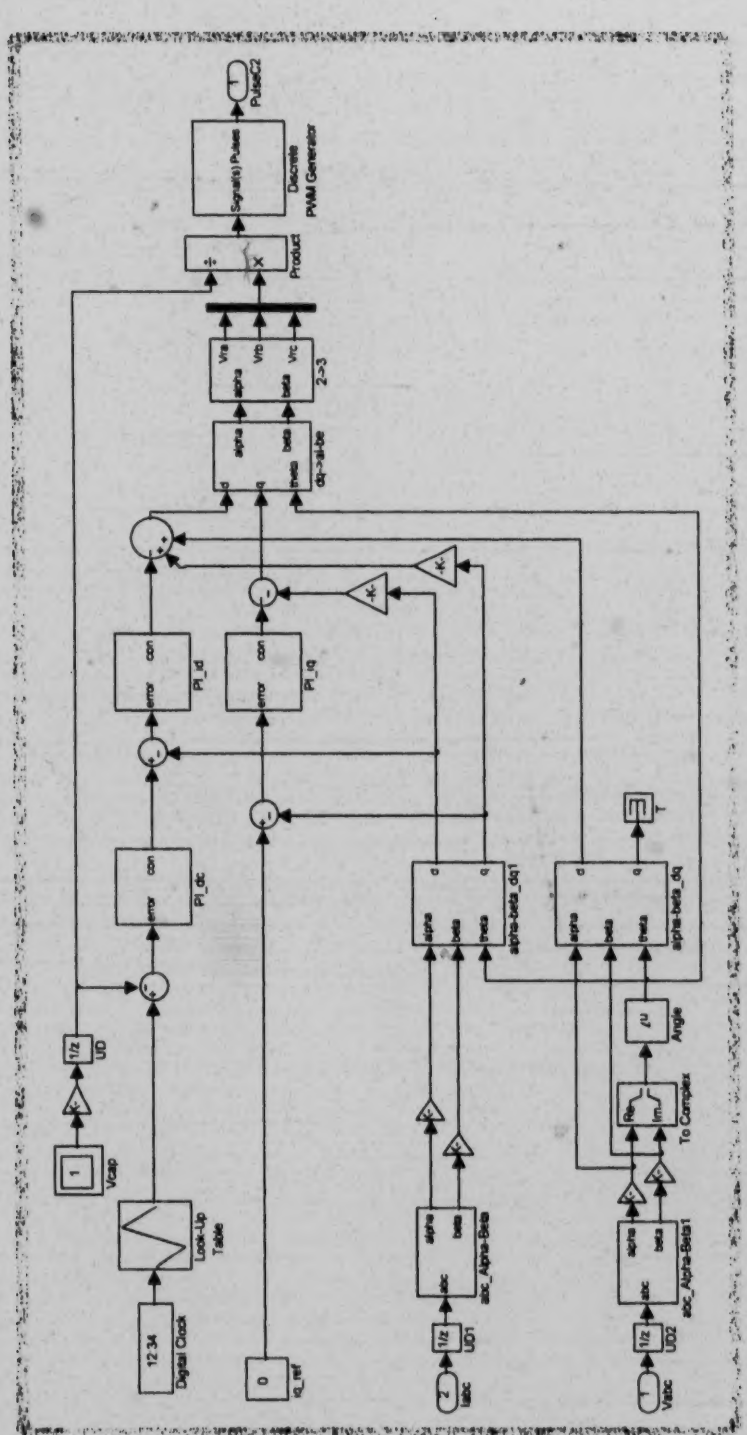

Figure G.5: DC Capacitor Charging Control Schematics Implemented in MATLAB/SIMULINK V.7.0.1

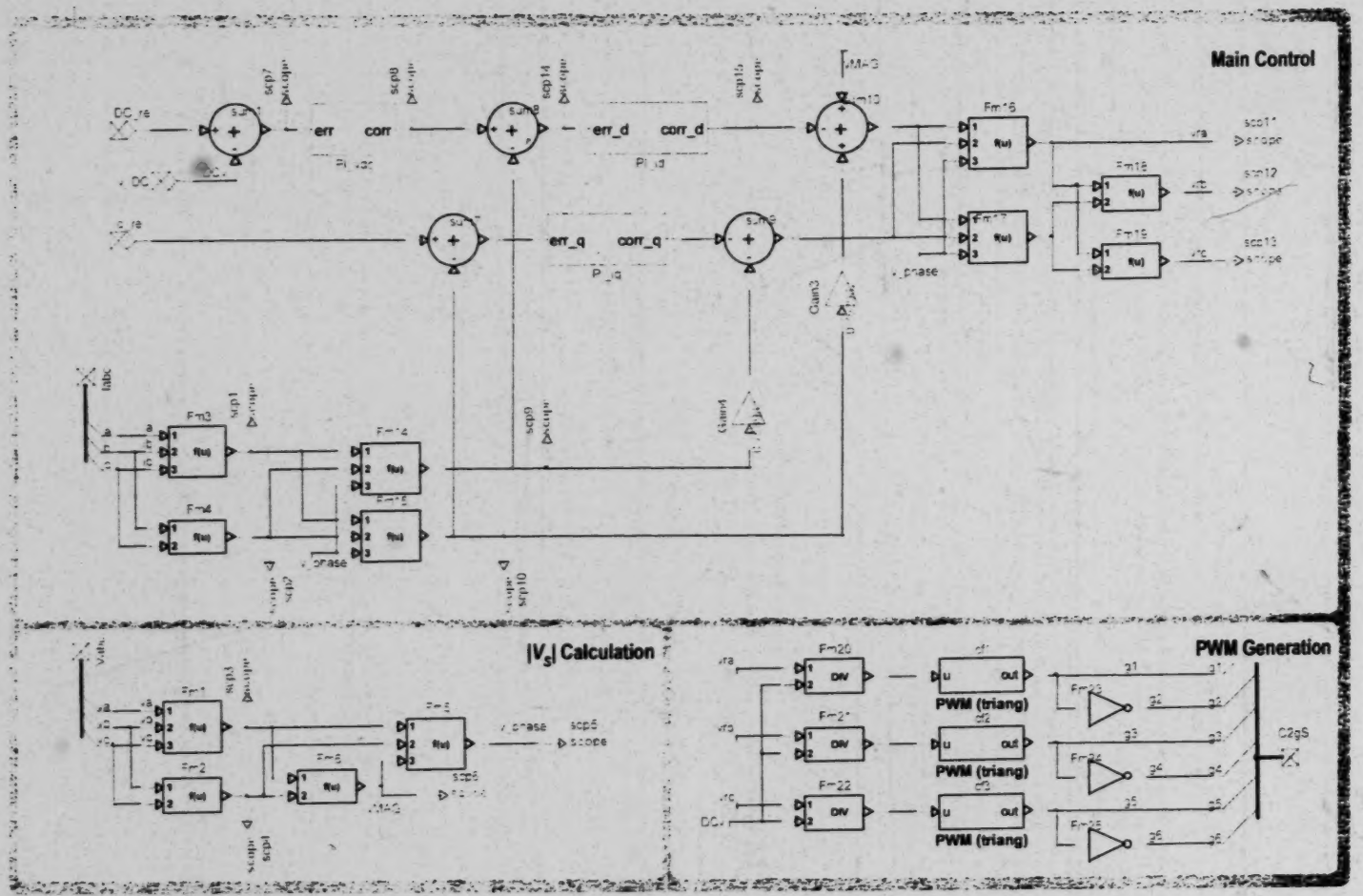

Figure G.6: DC Capacitor Charging Control Schematics Implemented in EMTP-RV V1.1

H

Complete DFIG Implementation

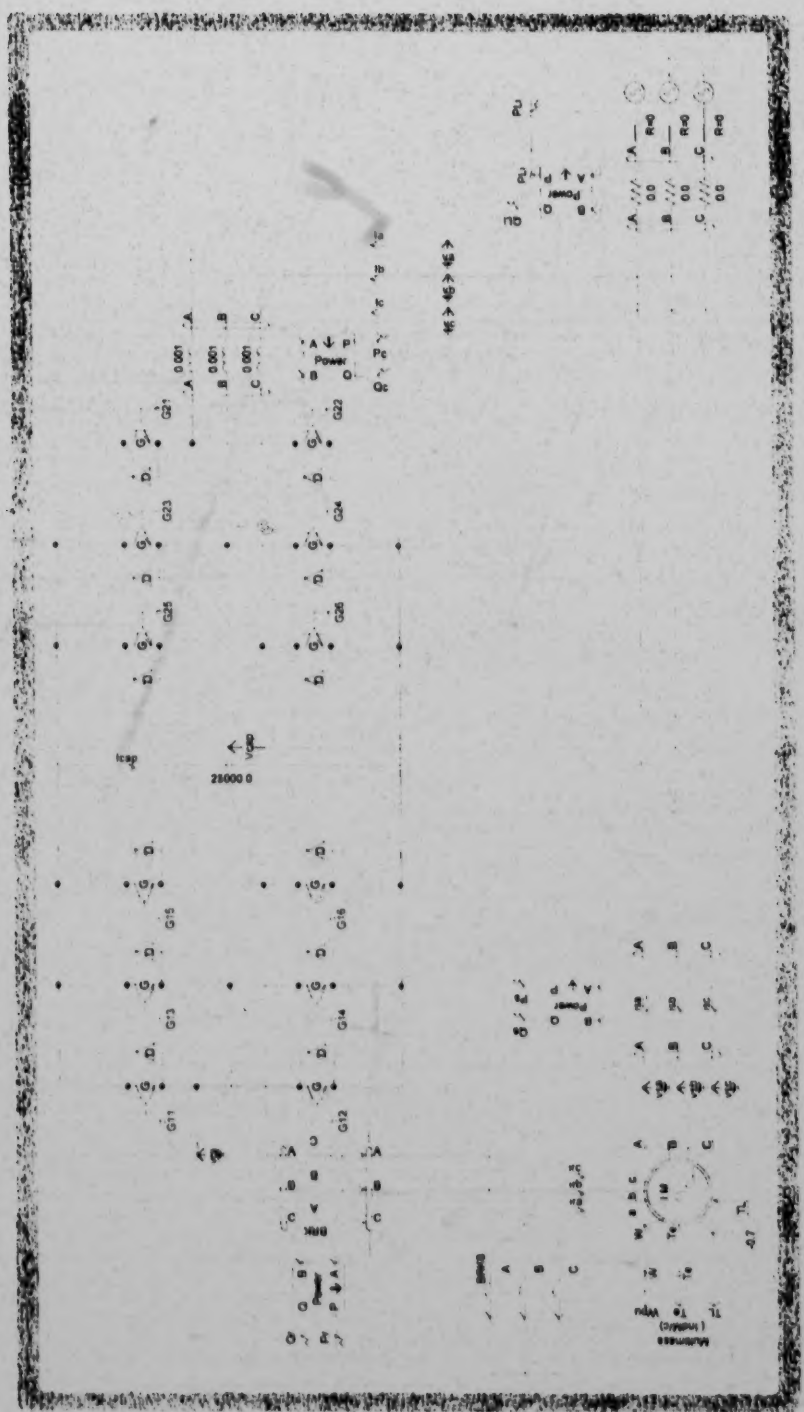

Figure H.1: DFIG Schematics Implemented in PSCAD/EMTDC V4.0

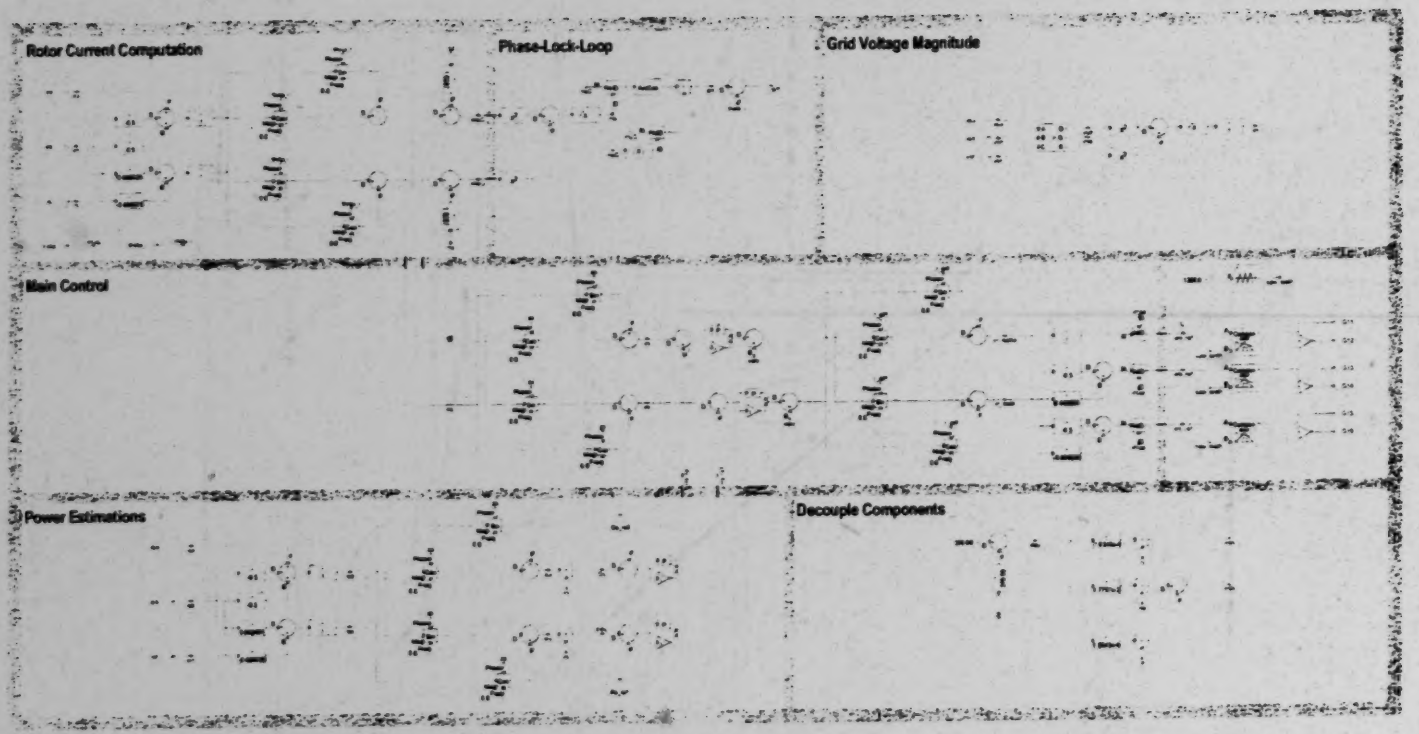

Figure H.2: Rotor-side Converter Controller Schematics Implemented in PSCAD/EMTDC V.4.0

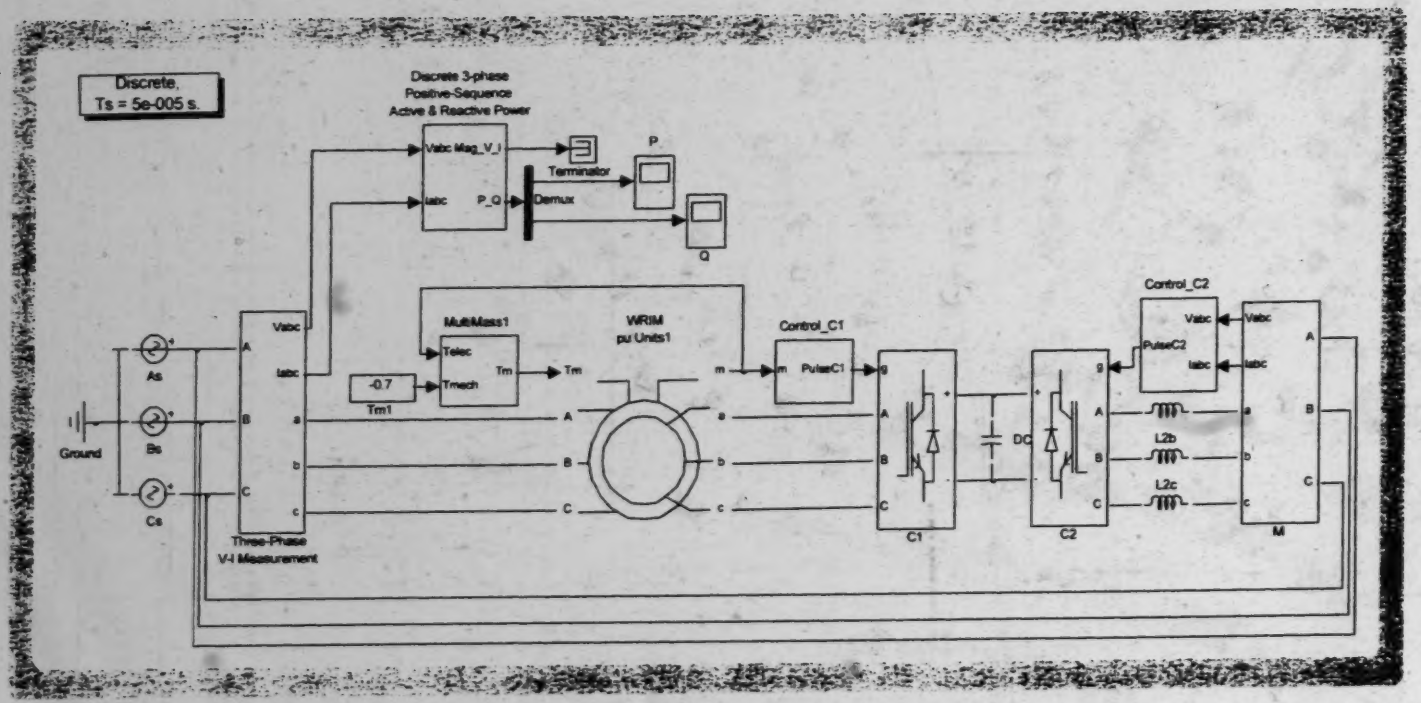

Figure H.3: DFIG Schematics Implemented in MATLAB/SIMULINK V.7.0.1

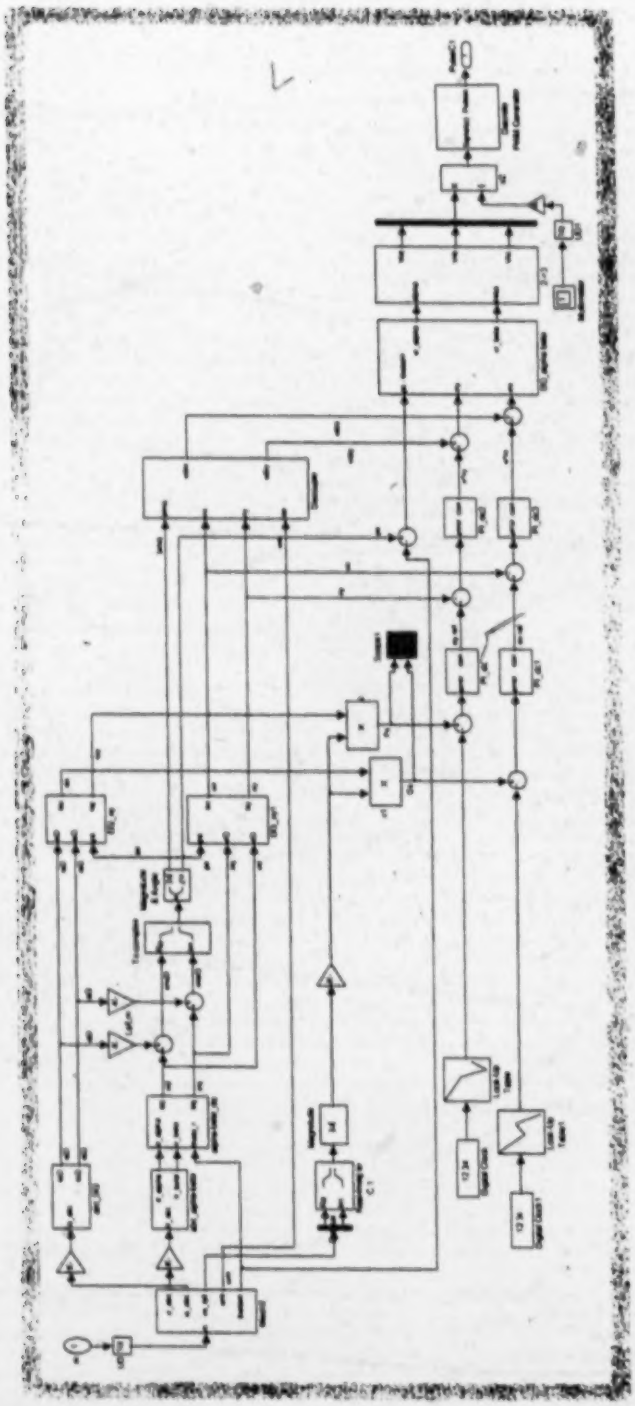

Figure H.4: Rotor-side Converter Controller Schematics Implemented in MATLAB/SIMULINK V.7.0.1

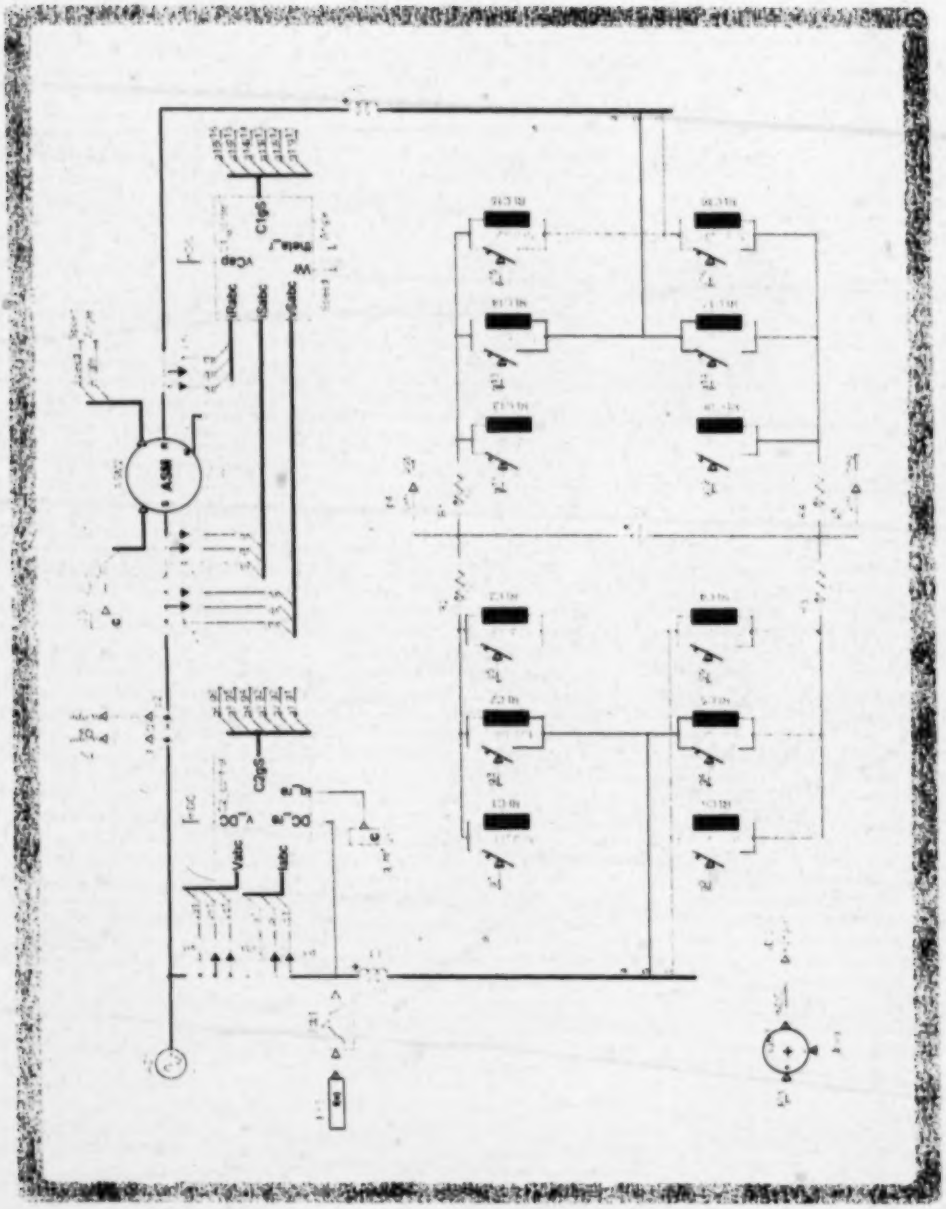

Figure H.5: DFIG Schematics Implemented in EMTP-RV V1.1

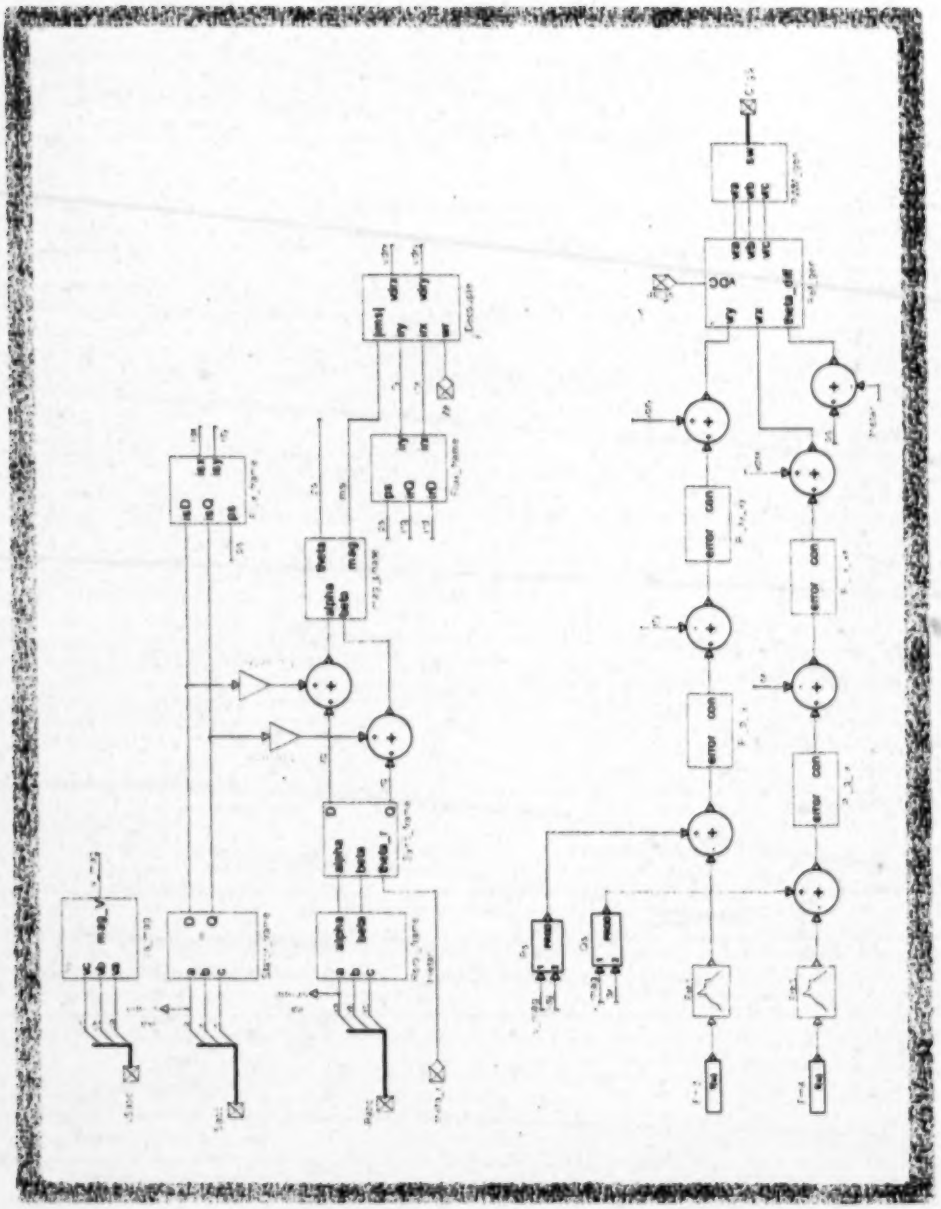

Figure H.6: Rotor-side Converter Controller Schematics Implemented in EMTP-RV V1.1

I

DFIG Implemented with RT-LAB Modules

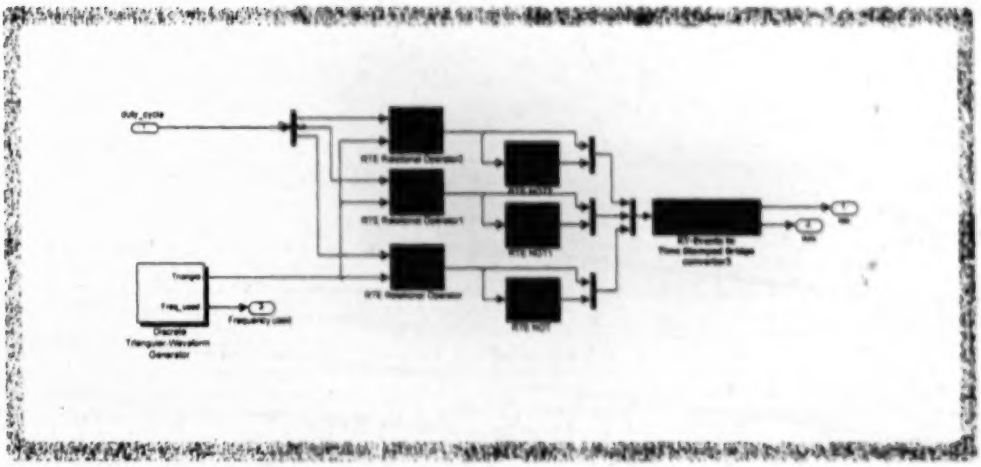

Figure I.1: PWM Pulse Generation with RT-EVENTS V.2.4 Comparison Block

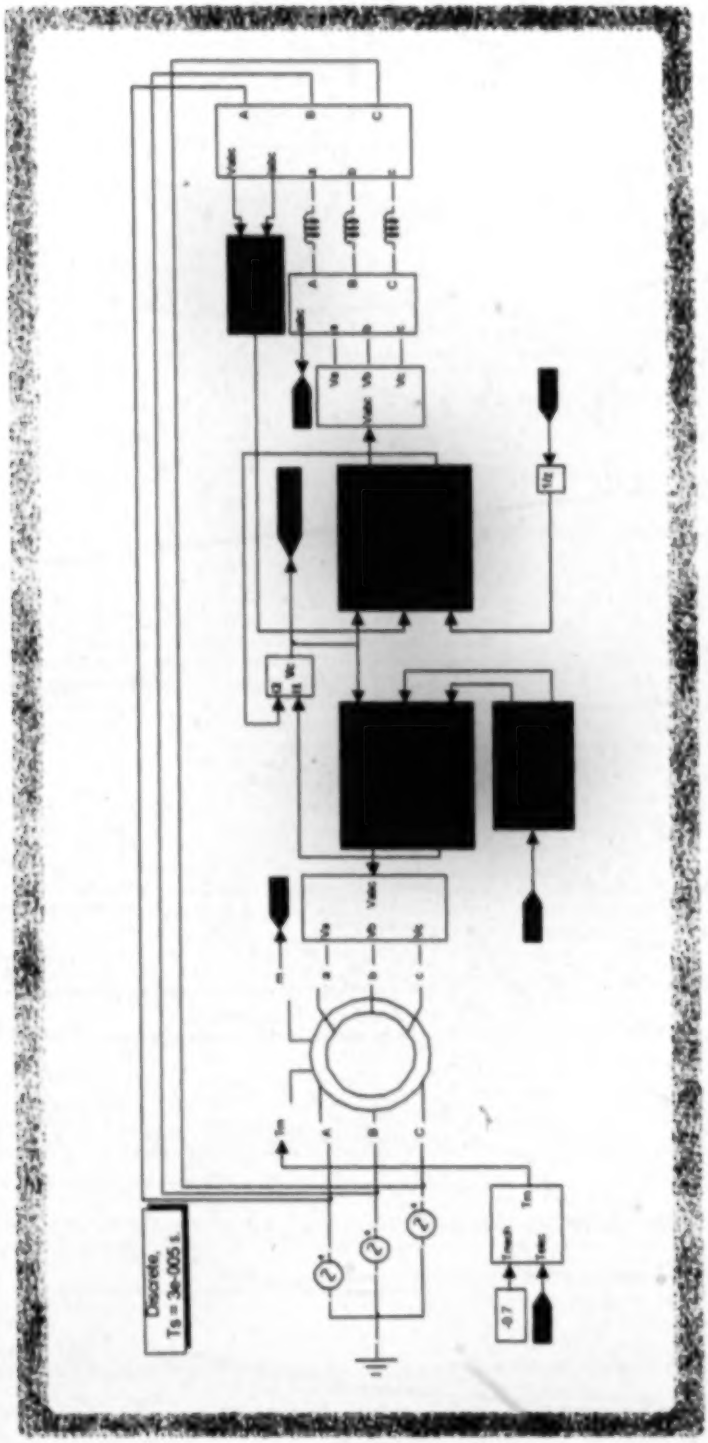

Figure 1.2: DFIG Schematics Implemented with RT-EVENTS V2.4 Time-Stamped Bridge

J

Loop-free Trapezoidal Implementation

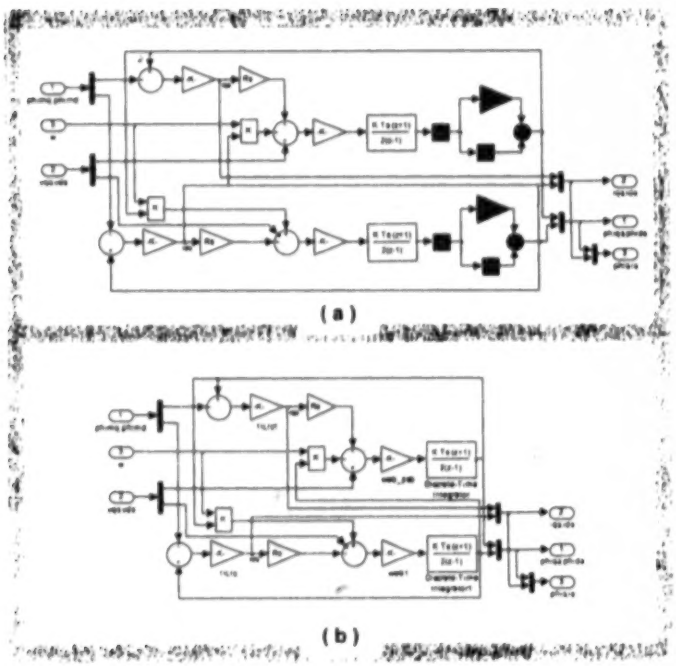

Figure J.1: Loop-free Trapezoidal Implementation for WRIM in MATLAB/SIMULINK V.7.0.1: (a) stator-side algebraic-loop compensated with memory buffer and prediction mechanism; (b) original stator winding model

K

3^{rd} Order WRIM Implementation

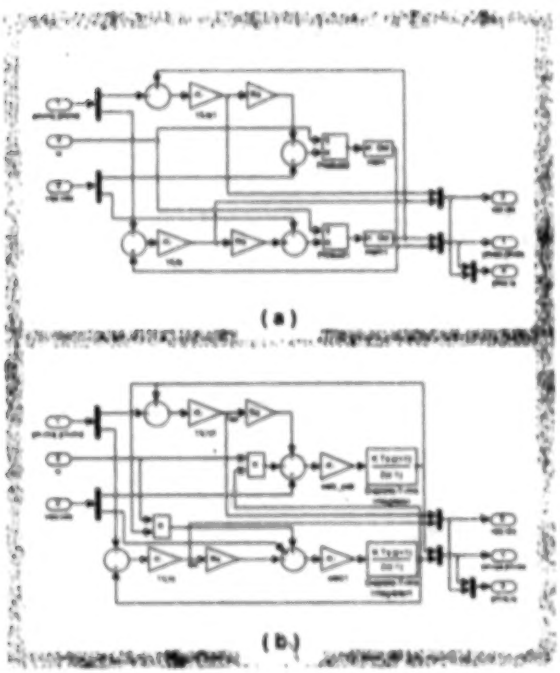

Figure K.1: 3^{rd} Order WRIM Implementation in MATLAB/SIMULINK V.7.0.1: (a) modified stator winding model; (b) original stator winding model